Smart Materials and Devices

Science Exploration

Open Access Review

Morphological control and structural modification of RuO_2-based materials for boosting electrochemical oxygen evolution

Wen-Jing Feng[1,2], Xiu Wang[1,2], Ling-Xian Wang[2,3], Huan Yang[2,3], Cheng-Zong Yuan[2,*], Xiaomeng Zhang[2,3,4,*], Ruixiang Wang[1,*]

[1]Jiangxi Provincial Key Laboratory of Green and Low Carbon Metallurgy for Strategic Nonferrous Metals, Jiangxi University of Science and Technology, Ganzhou 341000, Jiangxi, China.
[2]Ganjiang Innovation Academy, Chinese Academy of Sciences, Ganzhou 341119, Jiangxi, China.
[3]University of Science and Technology of China, Hefei 230026, Anhui, China.
[4]State Key Laboratory of Mesoscience and Engineering, Institute of Process Engineering, Chinese Academy of Sciences, Beijing 100190, China.

***Correspondence to:** Cheng-Zong Yuan, Ganjiang Innovation Academy, Chinese Academy of Sciences, Ganzhou 341119, Jiangxi, China. E-mail: czyuan@mail.ustc.edu.cn
Xiaomeng Zhang, Ganjiang Innovation Academy, Chinese Academy of Sciences, Ganzhou 341119, Jiangxi, China; University of Science and Technology of China, Hefei 230026, Anhui, China; State Key Laboratory of Mesoscience and Engineering, Institute of Process Engineering, Chinese Academy of Sciences, Beijing 100190, China. E-mail: xmzhang@gia.cas.cn
Ruixiang Wang, Jiangxi Provincial Key Laboratory of Green and Low Carbon Metallurgy for Strategic Nonferrous Metals, Jiangxi University of Science and Technology, Ganzhou 341000, Jiangxi, China. E-mail: wrx9022@163.com

Received: July 02, 2026 **Accepted:** September 17, 2026 **Published:** September 20, 2026

Cite this article: Feng WJ, Wang X, Wang LX, Yang H, Yuan CZ, Zhang X, et al. Morphological control and structural modification of RuO_2-based materials for boosting electrochemical oxygen evolution Smart Mater Devices. 2027;3:202633. https://doi.org/10.70401/smd.2026.0049

Abstract

Proton exchange membrane water electrolysis (PEMWE) is regarded as a practical hydrogen production method due to its advantages such as smaller resistance loss, higher current density, and higher hydrogen purity. However, the efficiency of PEMWE technology is severely hindered by the slow kinetics and the high reaction barrier of the oxygen evolution reaction (OER). Therefore, developing cost-effective, efficient, and stable OER electrocatalysts is urgently needed. The RuO_2-based electrocatalysts have been proven to be promising alternatives to Ir-based catalysts due to their excellent electrocatalytic activity and high adaptability in acidic environments. This review comprehensively summarizes and discusses the morphological control strategies, advanced modification strategies, and structural synergy of RuO_2 catalysts. Furthermore, the composition and industrial development status of PEMWE are elaborated, along with the current research progress of RuO_2 as an anode in electrolysis. Finally, relevant suggestions for RuO_2 research and practical applications are presented, the challenges facing practical deployment are analyzed, and future research directions are outlined.

Keywords: RuO_2-based electrocatalyst, structure engineering, modification strategies, oxygen evolution reaction, proton exchange membrane water electrolysis, fundamentals

1. Introduction

The growing global energy crisis stems primarily from rapid fossil fuel depletion and severe environmental degradation caused by greenhouse gas emissions. This crisis has intensified the urgency to develop sustainable energy solutions[1,2]. Hydrogen, known for its high energy density (142 MJ kg^{-1}), carbon-neutral combustion, and compatibility with renewable energy systems, has become a key clean energy carrier to address these challenges[3,4]. Among various hydrogen production methods, electrocatalytic water splitting is a promising and environmentally friendly approach, especially when powered by renewable energy sources like solar or wind (Figure 1a)[5,6]. This method enables scalable production of high-purity hydrogen under ambient conditions, while its efficiency depends critically on developing cost-effective, robust electrocatalysts[7,8]. The oxygen evolution reaction (OER), a key half-reaction in water electrolysis, exhibits inherently slow kinetics owing to its complex four-electron transfer process and the high energy barrier of O-O bond formation[9,10]. In contrast, the hydrogen evolution reaction (HER) proceeds via a simpler two-electron pathway, enabling faster reaction rates and lower overpotentials[11]. The substantial thermodynamic and kinetic barriers of the OER often lead to disproportionately high energy consumption, making it the rate-limiting step in overall water splitting systems[12,13]. To overcome

© The Author(s) 2027. This is an Open Access article licensed under a Creative Commons Attribution 4.0 International License (https://creativecommons.org/licenses/by/4.0/), which permits unrestricted use, sharing, adaptation, distribution and reproduction in any medium or format, for any purpose, even commercially, as long as you give appropriate credit to the original author(s) and the source, provide a link to the Creative Commons license, and indicate if changes were made.

this limitation, developing robust and cost-effective electrocatalysts with optimized electronic and structural properties is crucial. These catalysts should effectively lower activation energies, improve reaction efficiency, and facilitate scalable hydrogen production under industrial conditions[14,15].

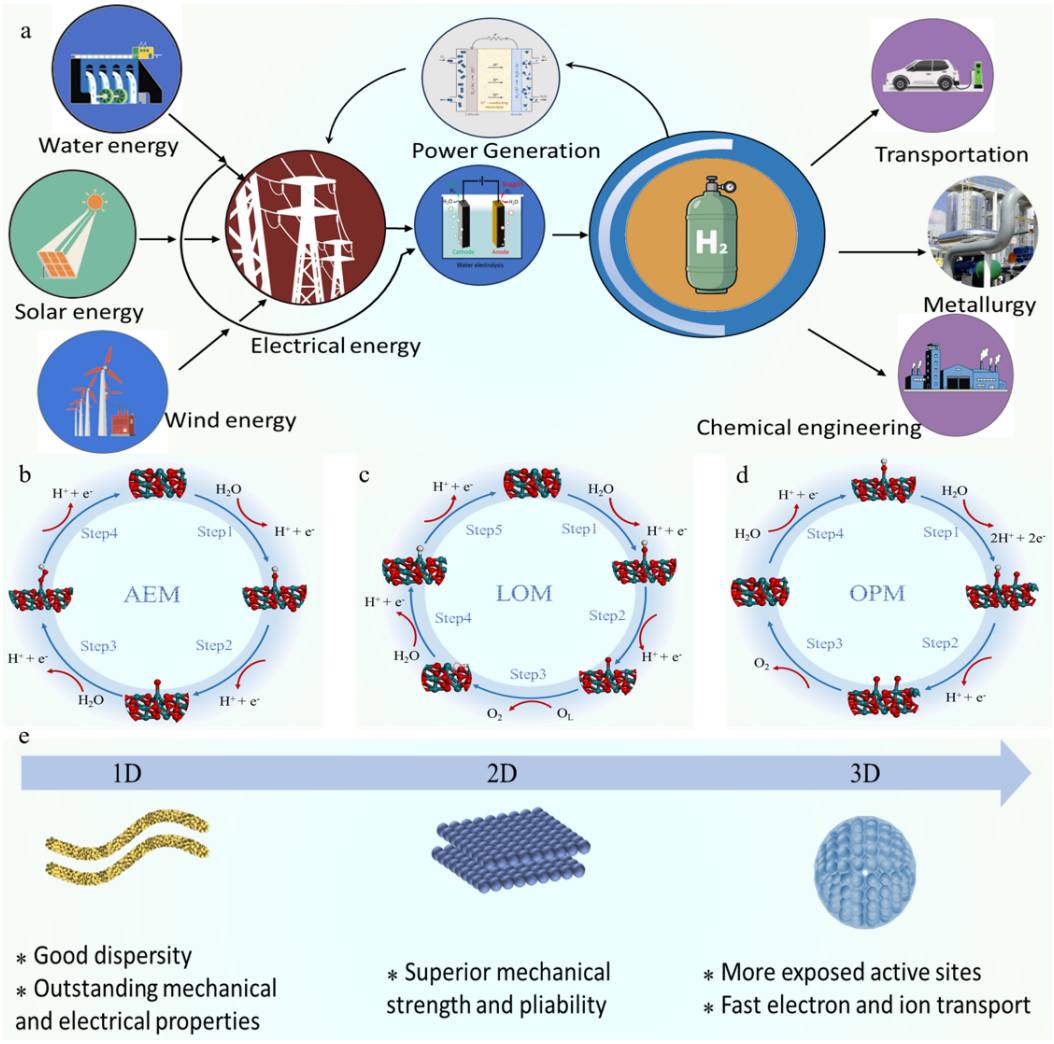


Figure 1. (a) Hydrogen production by water electrolysis and its application; Schematic illustrations of the possible (b) AEM; (c) LOM; (d) OPM pathways; (e) Advantages of one-dimensional nanowires, two-dimensional sheet-like structures, and three-dimensional spherical structures sheets in electrocatalysis. AEM: adsorbate evolution mechanism; LOM: lattice oxygen mechanism; OPM: oxide pathway mechanism; 1D: one-dimensional; 2D: two-dimensional; 3D: three-dimensional.

Alkaline water electrolysis (AWE) and proton exchange membrane water electrolysis (PEMWE) represent the two dominant technologies for hydrogen production, yet their OER mechanisms differ fundamentally[16,17]. In AWE, O_2 and H_2O are generated through hydroxyl group oxidation at the anode, whereas PEMWE relies on direct water oxidation, necessitating the cleavage of strong O-H covalent bonds[18]. At present, although alkaline water electrolysis still dominates, proton-exchange membrane water electrolysis has also achieved significant development momentum[19]. PEMWE offers advantages over alkaline electrolysis, including higher hydrogen purity, greater current density, and superior energy efficiency. In acidic media, the HER proceeds faster with lower resistance losses, and the system operates over a wider temperature range with a more compact footprint[20]. However, breaking the strong oxygen-hydrogen covalent bonds in water molecules requires a significant amount of energy in PEMWE, which makes the OER of PEMWE unfavorable both in terms of kinetics and thermodynamics[15]. Additionally, the acidic environment of PEMWE limits catalyst options, as transition metal-based oxides degrade under such conditions, necessitating costly iridium (Ir) catalysts for stability[21]. At approximately $164 per gram, Ir is prohibitively expensive; moreover, PEMWE deployment alone is projected to consume over 75% of annual Ir production unless usage is reduced[22,23]. Therefore, developing robust oxygen evolution reaction electrocatalysts operable in acidic media remains a critical challenge for advancing PEMWE[14]. Among the limited candidates capable of surviving the harsh acidic and oxidative conditions of OER, RuO_2 and IrO_2 stand as the two benchmark electrocatalysts, both crystallizing in the rutile structure and exhibiting metallic-type conductivity due to the relatively small electronegativity difference between the metal and oxygen[24]. Despite these structural and conductive similarities, RuO_2 and IrO_2 exhibit fundamentally divergent

catalytic behaviors; RuO_2 is significantly more active but far less stable, which originate from deep physicochemical differences rather than mere cost disparities[11,25]. The most fundamental distinction lies in the bonding character of the metal-oxygen bonds. Recent density functional theory (DFT) investigations by Tang *et al.* have revealed that RuO_2 features ionic-dominated Ru-O bonds with delocalized electron distribution, where the electron filling in the Ru-O bond is calculated to be 2.412[26]. In contrast, IrO_2 exhibits covalent-dominated Ir-O bonds with more localized electron density, with a significantly higher electron filling of 2.942 in the Ir-O bond. The divergent bonding and electronic characteristics directly translate into dramatically different oxidation and dissolution behaviors under OER conditions. DFT calculations demonstrate that the dissolution energy change for RuO_2 is -0.306 eV (thermodynamically favorable), whereas for IrO_2 it exceeds 2.9 eV (highly thermodynamically unfavorable)[26]. This means that RuO_2 dissolution is thermodynamically spontaneous under OER conditions, while IrO_2 dissolution requires substantial energy input.

Recently, ruthenium (Ru)-based catalysts have attracted much attention due to their higher OER activity and lower cost compared to Ir-based catalysts[27]. While Ru-based oxides like RuO_2 demonstrate exceptional OER activity surpassing Ir-based counterparts, their susceptibility to dissolution under anodic potentials severely limits practical deployment[12,13]. This degradation arises from the irreversible oxidation of Ru^{4+} to soluble RuO_4 species, particularly in strongly acidic and oxidizing environments, leading to rapid catalyst deactivation and system efficiency loss[4].

The transformation $Ru^{4+} \rightarrow RuO_4$ is not an independent degradation pathway, but rather the result of multiple pathways being coupled together. (1) Cationic Overoxidation: $Ru^{4+} \rightarrow$ Soluble High-Valence Species. Under high anodic potentials, surface Ru^{4+} sites are electrochemically driven into thermodynamically unstable high-valence states ($Ru \geqslant {}^{+5\text{-}6}$), which dissolve as soluble species[28,29]; (2) Anionic Overoxidation: Lattice Oxygen Depletion and Structural Collapse. This degradation mode is intrinsically linked to the lattice oxygen mechanism (LOM) of OER. When lattice oxygen participates in O_2 evolution, it leaves behind oxygen vacancies (V_O) that progressively destabilize the RuO_2 crystal structure[30,31]; (3) Particle Pulverization: Ostwald Ripening, Coalescence, and Agglomeration. Beyond chemical/electrochemical dissolution, RuO_2 nanoparticles undergo physical degradation through several particle-level processes that reduce the electrochemically active surface area (ECSA) and alter the particle size distribution[32]; (4) Ionomer Corrosion and Catalyst-Ionomer Interface Degradation. The Nafion ionomer in the anode catalyst layer serves as the proton conductor and mechanical binder. Its degradation under PEMWE operating conditions has been identified as a critical but often overlooked degradation pathway[33,34]; (5) Interfacial Detachment: Catalyst Layer Delamination. The mechanical integrity of the catalyst layer depends on strong adhesion at multiple interfaces: catalyst-membrane, catalyst-ionomer, catalyst-porous transport layer (PTL), and catalyst-support. Interfacial detachment occurs when these adhesion forces are overcome by mechanical, chemical, or electrochemical stresses[35,36]. These five degradation modes form interconnected feedback loops: LOM generates oxygen vacancies that weaken the catalyst structure, making it more susceptible to bubble-induced detachment; freshly exposed surfaces dissolve rapidly under high-potential acidic conditions; dissolved Ru cations catalyze Fenton reactions that degrade the ionomer, further weakening mechanical binding and enabling more detachment; detached particles undergo Ostwald ripening and coalescence. This self-reinforcing cycle explains the characteristic accelerating degradation observed in RuO_2-based PEMWE anodes, where the voltage degradation rate increases over time rather than remaining constant.

Recent studies have focused on improving stability through novel strategies, including: (1) crystallographic phase engineering, (2) alloying with corrosion-resistant transition metals, and (3) constructing protective heterostructures[37]. For instance, integrating RuO_2 with conductive metal oxides or transition metal substrates has shown promise in suppressing surface overoxidation while maintaining high turnover frequencies[38]. Additionally, atomic-level doping strategies aimed at tuning the Ru-O covalency have emerged to enhance both thermodynamic stability and charge transfer kinetics[39,40]. Despite these advancements, further optimization of the activity-stability trade-off remains necessary to meet the U.S. Department of Energy's lifespan targets for PEMWE. This is particularly critical under industrial operating conditions, where current densities exceed 2 A cm^{-2} and power inputs fluctuate significantly.

Nanostructure engineering has transformed metal oxide catalyst development by enabling precise structural control and surface optimization[41]. As a representative example, RuO_2 demonstrates significantly enhanced catalytic efficiency through dimensional engineering. Low-dimensional RuO_2 structures, including one-dimensional nanowires (1D NWs), two-dimensional nanosheets (2D NSs), and three-dimensional (3D) hierarchical frameworks exhibit superior charge transfer kinetics, increased exposure of coordinatively unsaturated sites, and enhanced mass transport efficiency compared to bulk counterparts[2]. Two-dimensional RuO_2 nanosheets exhibit enhanced electron mobility due to quantum confinement effects, while their atomic thickness provides exceptionally high surface-to-volume ratios that are critical for OER[42]. These nanostructured materials surpass traditional nanoparticles and non-oxide catalysts in both catalytic activity and stability, owing to their anisotropic electronic properties and defect-enriched surfaces[14]. However, synthesizing dimensionally controlled RuO_2 remains challenging as the metastable nanostructures tend to aggregate into thermodynamically favored particles during fabrication[43]. Advanced techniques like template-assisted combustion synthesis and potential-induced nanoclustering have emerged to stabilize these architectures by precisely regulating nucleation/growth dynamics[14,44]. The success of such nanoengineering approaches highlights the critical balance required between achieving desired catalytic geometries and maintaining structural integrity under operational conditions[45,46].

Beyond water electrolysis, RuO_2-based catalysts have demonstrated unique advantages in lithium-oxygen batteries, supercapacitors, and direct methanol fuel cells[47-49]. Each application imposes distinct performance requirements: Li-O_2 batteries demand dual ORR/OER functionality, supercapacitors require high specific capacitance and rate capability, and direct methanol fuel cells prioritize methanol oxidation activity and CO tolerance[47-49]. This diversified demand has driven RuO_2-based catalysts toward multifunctional composite designs.

Given the significant potential of RuO_2 in the OER and the increasing demand for developing more efficient oxygen evolution electrocatalysts, this review focuses on the latest research achievements of RuO_2-based catalysts under acidic conditions in water electrolysis, emphasizing the synergistic effect of nanostructures and modification strategies, as well as their practical applications in PEMWE devices. This review first outlines the OER mechanism in acidic electrolytes, and then systematically examines the morphological control of RuO_2 across 1D, 2D, and 3D architectures, establishing the structure-performance relationships that govern activity and stability. Subsequently, the modification strategies, including defect engineering, heteroatom doping, heterostructure construction, and phase engineering, that further optimize performance within each dimensional class are elaborated in detail. The design of various improvement strategies was highlighted, and the stability and reaction mechanism of the catalyst were summarized and analyzed in combination with structural regulation. To systematically investigate the viability of deploying RuO_2 catalysts within operational PEMWE systems at an industrial scale, this review initiates with a structural decomposition of PEMWE apparatus, elucidating the functional contributions of individual subsystems to overall device performance. Subsequently, the advancements pertaining to RuO_2 as an anodic constituent within the membrane electrode assembly are critically surveyed. The discussion culminates in a comprehensive assessment of the present trajectory of PEMWE technology toward industrial-scale maturation. Finally, it discusses the current application status of RuO_2 catalysts and the challenges they face. This provides useful insights for promoting the development of efficient RuO_2 electrocatalysts and integrating them into sustainable energy systems. This key analysis aims to stimulate innovative methods, promote the development of RuO_2-based electrocatalysts, and facilitate their practical application in energy conversion.

The field of RuO_2-based acidic OER electrocatalysis has witnessed a proliferation of review articles over the past five years, each contributing valuable perspectives from specific angles, including OER mechanisms, the activity-stability trade-off[50,51], regulation strategies, and PEMWE device integration[52-54]. More recently, reviews have begun to address industrial-scale considerations. However, a critical gap persists: existing reviews treat synthesis methods, support selection, defect structure, OER mechanism, and industrial manufacturability as largely independent topics, failing to establish the causal chain that connects them. This fragmentation obscures a fundamental reality, that the choice of synthesis method simultaneously constrains the feasible support materials, determines the defect landscape, governs the dominant OER mechanism pathway, and ultimately dictates whether the catalyst can ever be manufactured at industrial scale. This review is structured around the framework of "Synthesis-Structure-Mechanism-Performance-Industrialization", and explicitly traces the causal relationships across these five aspects in the research of RuO_2-based catalysts. Collectively, these five perspectives transform this review from a conventional "progress summary" into a design framework that enables researchers to trace the full consequence chain from synthesis choice to industrial deployment, identify the critical trade-offs at each decision node, and select optimal strategies that balance performance with manufacturability, a capability that no existing review provides.

2. The OER Mechanisms over RuO_2-Based Catalysts

As a highly active electrocatalyst for the OER, the reaction pathway of RuO_2 will vary depending on the operating conditions and the structure of the catalyst. Three primary mechanisms, the adsorbate evolution mechanism (AEM), LOM, and oxide pathway mechanism (OPM)-have been proposed to describe its OER behavior.

2.1 AEM

The adsorbate evolution mechanism is a classical pathway for the OER, with its activity highly dependent on the adsorption energy of intermediates. The AEM process follows a four-electron transfer step and occurs at the metal active sites. Under acidic conditions, the reaction proceeds through surface-adsorbed water molecules: H_2O loses electrons to form *OH, which subsequently undergoes deprotonation to yield *O; this intermediate then reacts with another H_2O molecule to generate *OOH, ultimately releasing O_2 (Figure 1b). The reaction pathway under acidic conditions is as follows[55,56]:

$$H_2O + * \rightarrow {}^*OH + H^+ + e^- \quad (1)$$

$${}^*OH \rightarrow {}^*O + H^+ + e^- \quad (2)$$

$$H_2O + {}^*O \rightarrow {}^*OOH + H^+ + e^- \quad (3)$$

$${}^*OOH \rightarrow * + O_{2(g)} + H^+ + e^- \quad (4)$$

The OER activity of RuO_2-based catalysts is critically influenced by the interaction strength between oxygen intermediates (*OH, *OOH) and active sites. For 1D RuO_2 nanostructures (e.g., nanowires, nanorods), the confined geometry can enhance charge transport, but the limited accessibility of active sites may lead to excessively strong oxygen binding, which could hinder the formation of *OOH intermediates. In contrast, 2D RuO_2 nanosheets offer a high density of exposed active sites and tunable surface electronic states, enabling a moderate oxygen-binding strength that balances adsorption/desorption kinetics and thereby optimizes the rate-determining step. 3D RuO_2 architectures (e.g., porous frameworks), while providing hierarchical structures with high surface areas, introduce complex interfaces that may create heterogeneous binding sites.

Operando ^{18}O-differential electrochemical mass spectrometry (DEMS) measurements have provided direct experimental validation for the AEM pathway on RuO_2-based catalysts. When the catalyst surface is pre-labeled with ^{18}O and OER is conducted in $H_2{}^{16}O$ electrolyte, exclusive evolution of $^{32}O_2$ ($^{16}O^{16}O$) without detectable $^{34}O_2$ ($^{18}O^{16}O$) signals confirms that oxygen in the evolved O_2 derives solely from water molecules rather than lattice oxygen, consistent with the AEM pathway[57].

2.2 LOM

The LOM pathway involves a non-concerted proton-electron transfer step that engages both metal cation active sites and lattice oxygen, proceeding through five intermediate species. Within the LOM, lattice oxygen directly participates in the reaction, forming oxygen vacancies, and completes the OER process through the oxidation and reduction of lattice oxygen. The key distinction between LOM and AEM lies in the reaction pathway: the conventional *OOH intermediate is absent, and instead, lattice oxygen directly participates in the formation of O-O bonds, completing the redox cycle through surface oxygen vacancies (Figure 1c). Under acidic reaction conditions, the reaction pathway is as follows[52]:

$$H_2O + {}^* \rightarrow {}^*OH + H^+ + e^- \tag{5}$$

$$^*OH \rightarrow {}^*O + H^+ + e^- \tag{6}$$

$$^*O + O_L \rightarrow O_2 + V_O \tag{7}$$

$$V_O + H_2O \rightarrow O_L + {}^*H + H^+ + e^- \tag{8}$$

$$^*H \rightarrow {}^* + H^+ + e^- \tag{9}$$

By bypassing *OOH formation and directly utilizing lattice oxygen for O_2 generation, the LOM pathway offers enhanced intrinsic activity and faster kinetics than the conventional AEM. However, lattice oxygen participation in LOM introduces instability in catalysts due to cation dissolution, oxygen vacancy accumulation, and structural reconstruction. RuO_2 nanostructures of different dimensionalities show distinct activity-stability trade-offs in the lattice oxygen mechanism-based OER: 1D nanostructures leverage anisotropic charge transport and high surface-to-volume ratios, facilitating efficient electron transfer and increased active site exposure. However, their elongated geometry may accelerate lattice oxygen depletion along specific crystallographic planes, leading to localized structural collapse and rapid degradation under prolonged OER conditions. 2D RuO_2 nanostructures exhibit exceptionally high catalytic activity due to their large lateral dimensions and atomic-scale thickness, which provide abundant surface-active sites and enhanced lattice oxygen mobility. However, their ultrathin nature also makes them particularly susceptible to structural degradation. 3D architectures provide interconnected networks for bulk oxygen diffusion and buffer lattice strain during oxygen redox cycles, thereby improving structural resilience. The multidimensional porosity also mitigates localized over-oxidation by distributing oxygen vacancy formation more uniformly. Nevertheless, their complex interfaces and slower mass transport kinetics may partially offset the activity advantages inherent to LOM.

Operando O K-edge X-ray absorption spectroscopy (XAS) has provided direct spectroscopic evidence for lattice oxygen activation during LOM-based OER on RuO_2. The emergence of intense pre-edge features at potentials above 1.4 V *vs.* RHE, assigned to electrophilic oxygen species (O^-/O^{2-}), confirms the oxidation of lattice oxygen that precedes its participation in O-O bond formation[58]. Concurrently, online scanning flow cell inductively coupled plasma mass spectrometry (SFC-ICP-MS) measurements reveal that the onset of Ru dissolution coincides precisely with the onset of OER current, establishing a direct causal link between lattice oxygen and catalyst degradation[11].

2.3 OPM

The OPM is reliant on a high coverage of reaction intermediates on the catalyst surface, with the formation of O-O bonds occurring through direct coupling between adjacent species. A key characteristic of this mechanism is that it shares the first two steps (*OH and *O formation) with the AEM, while omitting the formation of the hydroxyl oxide group (*OOH) (Figure 1d). Under acidic reaction conditions, the reaction pathway is as follows[53]:

$$H_2O + * \rightarrow {}^*OH + H^+ + e^- \quad (10)$$

$${}^*OH \rightarrow {}^*O + H^+ + e^- \quad (11)$$

$$2{}^*O \rightarrow O_2 \quad (12)$$

The OER performance and stability of catalysts are significantly influenced by their nanostructure dimensions (Figure 1e). 1D nanostructures facilitate efficient electron transport along their axial direction, enhancing charge transfer kinetics during *O and *OH generation. However, their limited surface area may restrict the density of active sites. 2D nanostructures maximize exposed active surfaces, promoting *O/*OH adsorption and interfacial reactivity. Their atomic thickness also optimizes mass diffusion, though stacking or restacking issues may reduce accessibility. 3D nanostructures integrate the advantages of 1D and 2D systems, offering interconnected pathways for charge transport, high surface area, and robust mechanical stability. Their porous networks further support rapid O_2 release via direct *O–*O coupling without inducing oxygen vacancies, a critical feature for maintaining structural integrity in OPM. Compared to the LOM pathway, OPM's reliance on *O coupling for O_2 formation avoids vacancy-related degradation, making all dimensional nanostructures inherently more stable. However, 2D and 3D architectures exhibit superior OER activity due to their optimized balance between active site density, charge transport, and mass transfer. This dimensional engineering highlights the importance of nanostructure design in achieving both high efficiency and durability in OPM-based electrocatalysts.

Experimental verification of the OPM pathway has been achieved through combined operando Raman spectroscopy and ^{18}O-DEMS measurements. The detection of direct *O–*O coupling intermediates via operando Raman, coupled with the absence of $^{34}O_2$ signals in ^{18}O-DEMS, provides compelling evidence for the OPM pathway on certain RuO_2-based heterostructure catalysts[59].

Precisely controlling the composition and structure of the catalyst can maximize the exposure of active sites, while structural modification can regulate the electronic structure of the catalyst[20,60]. This process affects the adsorption and desorption of intermediates on the catalyst surface during the OER, thereby modulating the reaction mechanism to enhance catalytic activity and durability[61]. For example, Chen and colleagues synthesized a Co-doped nanorod-like RuO_2 electrocatalyst[62]. This unique structure increases the number of exposed active sites while protecting the active metals from dissolution in acidic electrolytes, thereby improving both catalytic activity and durability. The significant improvement in OER performance primarily stems from the modulated electronic structure of Co-doped nanorod-like RuO_2, which facilitates a LOM rather than the conventional AEM. Wang and colleagues also synthesized Co-doped RuO_2, but its structure is that of nanosheets with a unique porous morphology[48]. This structural design modulates the electronic configuration, shifting the oxygen evolution reaction pathway from the detrimental LOM to a more efficient AEM. Consequently, the stability of the RuO_2 matrix in acidic environments is significantly enhanced. Therefore, through deliberate morphological control and structural engineering, the reaction mechanism can be optimized to enhance both catalytic activity and stability. For practical applications, future research should integrate morphological control with modification strategies to synergistically improve the electrocatalytic performance and long-term durability of ruthenium-based catalysts in acidic media.

These considerations yield the following design guidelines for RuO_2-based OER electrocatalysts: (1) For applications prioritizing stability: suppress LOM by strengthening the Ru–O bond, reducing oxygen vacancy concentration, or downshifting the Ru d-band center to increase ε_d-ε_p separation[30,57,63]. The resulting AEM-type catalyst will have moderate activity but excellent durability. (2) For applications prioritizing peak activity: enhance LOM by increasing Ru–O covalency, creating oxygen vacancies, or employing amorphous/defect-rich RuO_x[64,65]. The LOM-type catalyst will deliver exceptional activity but limited lifetime. (3) For the optimal balance: engineer OPM-enabling dual-site configurations through heteroatom doping, high-entropy design, or short-range-ordered Ru atom arrays on appropriate substrates[59,66,67]. The OPM-type catalyst can potentially break the activity–stability trade-off by combining scaling-relation-free activity with lattice-preserving stability. (4) For controlled LOM with self-healing: develop oxygen vacancy activation–replenishment cycles that allow controlled lattice oxygen participation while maintaining structural integrity through continuous vacancy refilling from the electrolyte[68].

A central debate in the RuO_2-based OER community concerns whether LOM should be completely suppressed or strategically harnessed. Our position, based on the evidence surveyed in this review, is that complete LOM suppression via AEM enforcement is a near-term strategy that improves stability but sacrifices the intrinsic activity advantage of RuO_2, while controlled LOM utilization with self-healing represents a potentially transformative long-term strategy but currently lacks experimental validation under industrial conditions. The rationale is as follows: AEM-type catalysts achieve excellent stability but their overpotentials remain constrained by the scaling relation. LOM-type catalysts achieve lower overpotentials but fail within tens of hours. The OPM pathway offers a theoretical escape from this dichotomy, but its geometric requirements are not naturally satisfied on pristine RuO_2 surfaces. We argue that the most productive research direction is not to choose between LOM suppression and LOM utilization, but to engineer catalysts where LOM contribution is minimized at low overpotentials but selectively activated at high overpotentials, with concurrent vacancy replenishment mechanisms that maintain structural integrity. This "adaptive mechanism switching" concept

requires dynamic operando monitoring under realistic PEMWE conditions, a capability that is only now becoming available with the development of high-time-resolution operando techniques.

It should be noted that in practical OER conditions, multiple mechanisms may operate simultaneously on the same catalyst, with their relative contributions determined by the local surface structure, defect distribution, and applied potential. The overall activity and stability are therefore determined by the weighted average of the contributions from each mechanism, and the optimal catalyst design should aim to maximize the OPM contribution while minimizing the LOM contribution.

The three OER pathways on RuO_2, AEM, LOM, and OPM, are not mutually exclusive but compete dynamically depending on the catalyst's electronic structure and operating conditions. The operating conditions of PEMWE: high current densities, elevated temperatures, and strongly acidic environments, profoundly influence the competition among OER pathways in ways that are often underappreciated.

At high anodic potentials, the Ru oxidation state increases ($Ru^{3+} \rightarrow Ru^{4+} \rightarrow Ru > n^{4+}$), which strengthens the Ru-O covalency and lowers the barrier for lattice oxygen oxidation. Operando XAS studies have shown that on pristine RuO_2, the Ru oxidation state increases continuously with potential without saturation[69,70], indicating progressive lattice oxygen activation that favors LOM. At high overpotentials, the surface coverage of *O increases significantly. When two adjacent O species are simultaneously populated, the OPM pathway (O + *O coupling) becomes kinetically accessible. However, on conventional RuO_2 (110) surfaces, the *O coverage at adjacent bridge sites is limited by the site geometry and the strong O-O repulsion, making OPM less favorable than on specially designed dual-site catalysts[71]. At high current densities, the local pH near the anode decreases (more acidic) due to inefficient proton removal, and O_2 bubble accumulation creates local mass transport limitations. The more acidic local environment accelerates Ru dissolution, while O_2 bubbles can cause mechanical stress on the catalyst layer. These effects create a positive feedback loop: LOM $\rightarrow$ Ru dissolution $\rightarrow$ local acidification $\rightarrow$ accelerated dissolution[72].

The high-temperature PEM working environment affects pathway competition through multiple mechanisms:

(1) Thermal activation of lattice oxygen. Elevated temperatures reduce the kinetic barrier for lattice oxygen participation. The activation energy for O-O coupling via LOM is typically lower than that for the *OOH formation step in AEM, meaning that LOM becomes increasingly competitive at higher temperatures. DFT calculations have shown that the energy difference between AEM and LOM pathways decreases with increasing temperature, favoring LOM at PEMWE operating temperatures[73,74].

(2) Accelerated Ru dissolution kinetics. At high-temperature, the dissolution rate is higher than at 25 °C, significantly shortening the catalyst lifetime. This thermal acceleration is particularly detrimental for LOM-dominated catalysts, where the dissolution rate is already high at room temperature.

(3) Enhanced water activation. Higher temperatures improve water adsorption and dissociation kinetics, which can favor AEM by facilitating the *OH $\rightarrow$ *O $\rightarrow$ *OOH sequence. However, this benefit is often outweighed by the simultaneous acceleration of LOM kinetics.

Recent operando studies have identified a critical potential threshold for LOM activation on RuO_2. Using operando DEMS with ^{18}O isotope labeling, it has been demonstrated that on pristine RuO_2, the $^{34}O_2$ signal becomes detectable above ~ 1.4 V *vs.* RHE and increases sharply above ~ 1.6 V[75]. This threshold corresponds to the onset of $Ru^{4+} \rightarrow Ru > n^{4+}$ oxidation, where the increased Ru oxidation state activates the lattice oxygen for nucleophilic attack on adjacent *O. Above this threshold, the LOM contribution to total O_2 evolution can reach 20-40% on unmodified RuO_2, directly correlating with accelerated Ru dissolution[76].

Heteroatom doping modulates the Ru-O covalency by altering the electron density distribution. Dopants with higher electronegativity or stable high oxidation states can withdraw electron density from Ru, lowering the Ru oxidation state and weakening the Ru-O covalency. This raises the oxygen vacancy formation energy, making LOM thermodynamically less favorable and shifting the pathway back to AEM. Lattice strain modulates the Ru-O bond length and orbital overlap, thereby tuning the Ru-O covalency. Compressive strain shortens the Ru-O bond and enhances covalency (favoring LOM), while tensile strain elongates the Ru-O bond and weakens covalency (suppressing LOM). Dual-Active Site Engineering for OPM: Instead of suppressing LOM by reverting to AEM (which is activity-limited), OPM provides an alternative pathway that achieves both high activity and high stability. OPM requires adjacent dual-active sites where two *O species can couple directly to form O_2 without lattice oxygen participation. Heterophase and grain boundary engineering provide a synergistic approach: the disordered/amorphous regions accommodate structural flexibility and generate abundant active sites, while the crystalline regions ensure efficient electron transport. The amorphous/crystalline interface acts as a "charge buffer" that prevents excessive charge accumulation on Ru sites, thereby inhibiting the transition to high oxidation states that trigger LOM[77]. Recent studies have revealed that the structure of interfacial water layers plays a critical role in OER pathway selection. A well-ordered interfacial water network can facilitate proton transfer in the AEM pathway, while a disordered water structure may favor LOM by enabling direct oxygen radical coupling. Wu *et al*. demonstrated that the interfacial water structure on RuO_2 can be modulated by surface chemistry, and that a more ordered hydrogen-bonded water network promotes AEM by facilitating efficient proton removal during *OOH formation[78].

We strongly recommend that future studies on RuO_2-based OER catalysts include at least one operando technique for pathway identification (preferably DEMS with ^{18}O labeling) to provide mechanistic evidence for the claimed LOM suppression. Without such evidence, claims of "LOM suppression" based solely on improved stability are speculative, as stability improvements can arise from multiple mechanisms unrelated to pathway switching.

While the preceding sections have individually described the reaction pathways of the AEM, LOM, and OPM, a systematic comparison of their applicability boundaries and condition-dependent preferences is essential for guiding the rational design of RuO_2-based OER electrocatalysts. Table 1 summarizes the key distinguishing features of the three mechanisms.

Table 1. Comparative summary of AEM, LOM, and OPM for OER on RuO_2-based catalysts.

Feature	AEM	LOM	OPM
O-O bond formation	*O + H_2O → *OOH (nucleophilic attack)	Lattice O_{latt} + *O → O-O (direct coupling)	*O + *O → O-O (radical coupling)
Active site requirement	Single metal site	Metal site + adjacent lattice oxygen	Dual metal sites (M_1-O-M_2)
Scaling relation	Constrained	Bypassed	Bypassed
Lattice oxygen involvement	None	Direct participation → oxygen vacancy formation	None (lattice preserved)
Catalyst stability	High (lattice intact)	Low (structural degradation via O vacancy accumulation)	High (lattice intact)
pH dependence	Weak (proton-coupled electron transfer)	Strong	Weak to moderate
Diagnostic signature	*OOH intermediate (Raman ~ 1,060-1,100 cm^{-1})	^{18}O-labeled O_2 product (DEMS); TMA^+ sensitivity	O-O intermediate; singlet O_2 detection

AEM: adsorbate evolution mechanism; LOM: lattice oxygen mechanism; OPM: oxide pathway mechanism; OER: oxygen evolution reaction; DEMS: differential electrochemical mass spectrometry; TMA^+: tetramethylammonium ion.

The three mechanisms present fundamentally different activity-stability landscapes: AEM offers the highest stability but is limited by the scaling relation constraint, which imposes a theoretical minimum overpotential of ~ 0.37 V[79]. For RuO_2 following AEM, the theoretical overpotential on the (110) surface is ~ 0.698 V[26]. LOM breaks the scaling relation and can achieve lower overpotentials, but at the cost of lattice oxygen consumption, oxygen vacancy accumulation, and progressive structural degradation[80]. This is the fundamental origin of the activity-stability trade-off for RuO_2: its high intrinsic activity under LOM is inseparable from its poor durability. OPM represents the most promising pathway for simultaneously achieving high activity and high stability: it bypasses the scaling relation through direct O-O coupling (avoiding the high-energy *OOH intermediate) while preserving the lattice oxygen framework[59]. However, OPM imposes stringent geometric requirements (appropriate dual-site distance and *O adsorption configuration) that are not naturally satisfied on pristine RuO_2 surfaces, necessitating deliberate structural engineering[81].

While low-dimensional RuO_2 nanostructures (1D, 2D, 3D) offer significant advantages in terms of active site exposure, charge transport, and mass diffusion, their enhanced OER activity often comes at the expense of structural stability, a fundamental trade-off that must be critically evaluated for practical PEMWE applications. The activity-stability trade-off in RuO_2-based OER electrocatalysts is fundamentally governed by three interconnected electronic and structural descriptors: Ru-O covalency, lattice strain, and work function. Understanding their individual and synergistic roles provides the theoretical foundation for rational catalyst design that decouples activity from stability.

The covalency of the Ru-O bond, defined as the degree of hybridization between Ru 4d and O 2p orbitals, has emerged as the central descriptor governing both OER activity and stability in RuO_2-based catalysts[13,82]. Strong Ru-O covalency activates lattice oxygen for participation in the LOM pathway, which bypasses the *OOH formation step and delivers higher intrinsic activity. However, this same lattice oxygen activation destabilizes the oxide framework. The facile removal of lattice oxygen generates oxygen vacancies that propagate structural degradation and promote Ru dissolution[31,83]. Conversely, weakened Ru-O covalency stabilizes the lattice oxygen framework by lowering the O 2p band center relative to the Fermi level, thereby raising the thermodynamic barrier for lattice oxygen oxidation and suppressing the LOM pathway in favor of the more stable AEM[82,84]. The trade-off is clear: weakening Ru-O covalency enhances stability but typically reduces intrinsic activity, as the less activated lattice oxygen also diminishes the electrophilicity of surface Ru sites for water adsorption and activation.

Lattice strain exerts profound and multifaceted effects on both the activity and stability of RuO_2 catalysts. (1) Compressive strain and activity enhancement: According to d-band theory, compressive strain in RuO_2 downshifts the Ru d-band center, weakening the adsorption of oxygen intermediates. Since RuO_2 is positioned on the strong-binding side of the OER volcano plot, this weakening of intermediate adsorption moves the catalyst toward the volcano apex, enhancing OER activity[85]. Chaudhary *et al.* systematically demonstrated that compressive strain in RuO_2 improves OER activity by optimizing the binding energies of reaction intermediates[86]. (2) Tensile strain and stability enhancement: Tensile strain upshifts the O 2p band center relative to the Fermi level, but counterintuitively, moderate tensile strain can enhance the thermodynamic stability of lattice oxygen. DFT calculations by Cao *et al.* showed that 1% tensile strain in RuO_2 results in the highest enthalpy change for lattice oxygen loss, indicating enhanced resistance to lattice oxygen depletion[85]. This is because tensile strain elongates Ru-O bonds, reducing the Ru-O covalency and thereby raising the energy barrier for lattice oxygen oxidation. (3) Cation-vacancy induced compressive strain localization: An alternative approach to strain heterogeneity involves cation vacancies rather than dopant insertion. Xue *et al.* demonstrated that Ru vacancies in RuO_2 generate localized lattice contraction rather than the tensile distortion typically associated with vacancy formation[87]. This compressive strain localization downshifts the d-band center of neighboring Ru sites, optimizing intermediate adsorption for enhanced activity, while the overall lattice expansion provides structural buffering against degradation. The covalency of Ru-O bonds is simultaneously modulated by the strain field, suppressing lattice oxygen activity and enhancing stability.

The work function of RuO_2-based catalysts serves as a valuable indicator of their susceptibility to electrochemical over-oxidation and dissolution. The work function reflects the minimum energy required to remove an electron from the catalyst surface. A higher work function indicates a greater resistance to electron loss, which correlates with reduced tendency for Ru^{4+} to be further oxidized to soluble Ru > $^{4+}$ species (e.g., RuO_4)[88]. In the context of OER, the anodic potential drives the oxidation of surface Ru sites; catalysts with higher work functions require higher overpotentials to achieve the same degree of surface oxidation, thereby inherently resisting over-oxidation.

The work function, Ru-O covalency, and lattice strain are not independent descriptors but are deeply interconnected. Compressive strain typically downshifts the d-band center, which can increase the work function by reducing the density of states near the Fermi level[85,88]. Simultaneously, the strain-induced modulation of Ru-O bond length directly affects the Ru_{4d}-O_{2p} hybridization.

While the preceding subsections have outlined the thermodynamic and kinetic features of AEM, LOM, and OPM on the basis of *ex situ* characterization and DFT calculations, direct experimental verification of the operative pathway under realistic OER conditions requires *in-situ*/operando techniques. The following subsection systematically surveys the key operando methods that have been employed to identify and distinguish these mechanisms on RuO_2-based catalysts.

2.4 *In-situ* /operando characterization for probing OER mechanisms

Understanding the dynamic structural evolution of RuO_2-based catalysts under operating conditions is essential for elucidating the true active sites, reaction mechanisms, and degradation pathways. Conventional ex-situ characterization techniques provide only static snapshots before and after catalysis, potentially missing critical transient intermediates and structural transformations that occur exclusively under anodic potentials. In recent years, the development and application of *in-situ*/operando characterization techniques have revolutionized our understanding of RuO_2-based acidic OER electrocatalysts. This subsection systematically summarizes the key operando techniques and their contributions to unraveling the dynamic behavior of RuO_2 during OER.

Operando XAS. Operando XAS is arguably the most powerful technique for probing the electronic structure and local coordination environment of Ru under realistic OER conditions. It encompasses two complementary modalities:

(1) X-ray absorption near edge structure (XANES). Ru K-edge XANES provides element-specific information on the oxidation state of Ru atoms during OER. By monitoring the edge position shift as a function of applied potential, researchers can track the dynamic oxidation of Ru^{4+} to higher valence states (Ru > 4+) under anodic polarization, which is directly linked to the over-oxidation and dissolution pathway ($RuO_2 \rightarrow RuO_4$). A landmark study by Deka *et al.* employed operando Ru K-edge XANES to demonstrate that crystalline RuO_2 undergoes a progressive shift toward higher Ru oxidation states at potentials above 1.4 V *vs.* RHE, whereas amorphous RuO_x maintains a relatively stable Ru valence, correlating with the superior stability of the amorphous phase[89].

(2) Extended X-ray absorption fine structure (EXAFS). Ru K-edge EXAFS yields quantitative information on the Ru-O and Ru-Ru bond distances and coordination numbers, enabling real-time monitoring of lattice expansion/contraction and coordination changes during OER. For instance, operando EXAFS measurements on $Mn_{0.2}RuO_2$ revealed that the Ru-O bond length contracts under OER conditions, indicating lattice strain modulation by the dopant that strengthens the Ru-O bond and suppresses lattice oxygen participation[90]. Similarly, operando EXAFS studies on interstitial C-doped RuO_2 (C-RuO_2-RuSe) demonstrated that the C-O covalent bonds within the RuO_2 lattice remain intact during OER, confirming the structural stabilization role of interstitial carbon[91].

DEMS with isotope labeling. DEMS coupled with ^{18}O isotope labeling is the definitive technique for distinguishing between AEM and LOM pathways by tracking the oxygen source in the evolved O_2. In a typical experiment, the catalyst surface is pre-labeled with ^{18}O by cycling in $H_2{}^{18}O$, and the OER is subsequently performed in $H_2{}^{16}O$. If the LOM pathway is operative, lattice ^{18}O atoms participate in O_2

formation, producing $^{34}O_2$ ($^{18}O^{16}O$) and $^{36}O_2$ ($^{18}O^{18}O$) signals. Conversely, exclusive detection of $^{32}O_2$ ($^{16}O^{16}O$) confirms the AEM pathway, where oxygen is derived solely from water.

As demonstrated in the GB-RuO_2 system, DEMS analysis revealed complete absence of $^{34}O_2$ and $^{36}O_2$ signals, providing compelling evidence that grain boundaries effectively suppress lattice oxygen participation and enforce the AEM pathway[57]. Similarly, DEMS analysis of the RuO_2/$CoMnO_3$ heterostructure showed notably low $^{34}O_2$ levels, supporting AEM dominance[92]. These examples illustrate how DEMS serves as a critical mechanistic probe for validating the design rationale of modification strategies aimed at suppressing LOM.

Operando Raman spectroscopy. Operando Raman spectroscopy provides molecular-level fingerprint information on surface intermediates and structural changes of RuO_2 under working potentials. The Raman spectrum of rutile RuO_2 exhibits characteristic bands at ~ 528 cm^{-1} (E_g mode), ~ 646 cm^{-1} (A_{1g} mode), and ~ 716 cm^{-1} (B_2g mode), which are sensitive to lattice strain, oxygen vacancy concentration, and surface oxidation states. Recent studies have demonstrated that operando Raman can track the dynamic evolution of oxygen species on RuO_2 during OER. For GB-V-RuO_2, *in-situ* Raman spectroscopy revealed the emergence of a new peak at ~ 1,019 cm^{-1} under anodic potentials, assigned to superoxide (*OO) intermediates, confirming the lattice oxygen oxidation pathways exist simultaneously on the catalyst[93]. For RuO_2 heterojunction catalysts, operando Raman has been used to monitor the reversible cycling of oxygen species under working potentials, revealing that the heterojunction structure facilitates the reversible formation and consumption of surface oxygen intermediates, thereby improving both activity and stability[94]. Additionally, operando Raman studies on Rh-doped RuO_2 demonstrated that oxygen vacancies serve as active sites for water adsorption and activation, with the Raman peak intensity of oxygen vacancy-related modes correlating directly with OER activity[95].

Operando Fourier transform infrared spectroscopy (FTIR). Operando FTIR spectroscopy enables the identification of adsorbed reaction intermediates on the catalyst surface under potential control. In the RuO_2/MoO_3 system, operando FTIR spectra recorded at 1.6 V *vs.* RHE revealed a distinct absorption band corresponding to *OO intermediates on MoO_3 sites, providing direct experimental evidence for the oxygen spillover mechanism from RuO_2 to MoO_3[96]. This technique is particularly valuable for detecting short-lived intermediates that cannot be captured by ex-situ methods, and for verifying the proposed dual-site OPM pathway in heterostructured catalysts.

***In-Situ* electrochemical transmission electron microscopy/scanning electron microscope (EC-TEM/EC-SEM).** *In-situ* electrochemical TEM and SEM enable direct real-space visualization of morphological and structural changes of RuO_2 catalysts under electrochemical conditions. Deka *et al.* employed operando EC-SEM to observe the surface reconstruction of amorphous and crystalline RuO_x during OER, revealing that amorphous RuO_x undergoes reversible surface restructuring while crystalline RuO_2 experiences irreversible dissolution at grain boundaries[89]. This direct visualization provides crucial insights into the degradation mechanism: crystalline RuO_2 dissolves preferentially at under-coordinated sites (edges, corners, grain boundaries), while amorphous phases exhibit self-healing behavior through dynamic surface reconstruction. These observations rationalize the enhanced stability of amorphous-crystalline hybrid structures and grain boundary-engineered RuO_2.

***In-Situ* electrochemical impedance spectroscopy (EIS).** *In-situ* EIS under potentiostatic conditions provides dynamic information on charge transfer resistance (R_{ct}), double-layer capacitance, and ion transport kinetics during OER. By tracking the evolution of R_{ct} as a function of applied potential and operation time, researchers can identify the onset of catalyst degradation (sudden increase in R_{ct}) and correlate it with structural changes observed by other operando techniques. For RuO_2 heterojunction catalysts, *in-situ* EIS has revealed that the interfacial charge transfer resistance remains stable during OER, confirming the robust electronic coupling at the heterointerface[93,94].

The power of operando characterization lies not in any single technique but in the synergistic combination of multiple complementary methods. A correlative operando framework, combining operando XAS (electronic/coordination), DEMS (mechanistic), and *in-situ* EC-TEM (morphological), provides the most comprehensive picture of the structure-mechanism-stability relationship. For example, simultaneous operando XANES and DEMS measurements can directly correlate Ru oxidation state changes with LOM activation, while combining operando Raman with *in-situ* EIS can link intermediate formation kinetics with charge transfer efficiency. Future studies should increasingly adopt such multi-technique operando approaches, particularly under PEMWE-relevant conditions, to bridge the gap between laboratory half-cell measurements and industrial device performance.

3. Morphological Control of RuO_2-Based Catalysts

The catalytic performance of RuO_2-based electrocatalysts is fundamentally governed by their nanoscale morphology, which determines the density and accessibility of active sites, the efficiency of charge and mass transport, and the mechanical resilience under operating conditions. Dimensional engineering, encompassing 1D, 2D, and 3D architectures, provides a primary design lever for optimizing these parameters before any chemical modification is applied. This section systematically examines how each dimensional class influences OER activity and stability in acidic media, establishes structure-performance correlations, and identifies the inherent trade-offs that motivate the modification strategies discussed in Section 4.

3.1 One-dimensional RuO_2 nanostructures

One-dimensional RuO_2 nanostructures, including nanowires, nanotubes, and nanorods, offer several intrinsic advantages for acidic OER. Their anisotropic geometry provides directional electron transport pathways along the axial direction, reducing charge transfer resistance and facilitating efficient electron delivery to active sites[97,98]. The high aspect ratio also promotes preferential exposure of specific crystal facets (e.g., the (110) plane of rutile RuO_2), which can be engineered to maximize the density of under-coordinated Ru sites that serve as OER active centers. Additionally, the one-dimensional morphology provides accessible channels for reactant diffusion and rapid O_2 bubble release, mitigating mass transport limitations at high current densities.

Barman *et al*. reported highly crystalline RuO_2 nanowires grown on carbon nitride (1D-RuO_2-CN_x), which exhibited a lower overpotential (η_{10} = 218 mV) and significantly higher stability compared to commercial RuO_2 in acidic media[99]. The excellent catalytic activity was attributed to the combined effects of exposed active sites, one-dimensional morphology, and the highly crystalline rutile structure. Similarly, Bhowmik *et al*. demonstrated that RuO_2 nanowires on g-C_3N_4 support achieved efficient OER across all pH values, with the 1D morphology ensuring rapid electron transport and structural stability[99].

However, 1D RuO_2 nanostructures face inherent limitations. Their confined geometry can lead to excessively strong oxygen binding at limited active sites, hindering the formation of *OOH intermediates and increasing the overpotential. More critically, the stability and durability of 1D RuO_2-based electrocatalysts under acidic conditions remain insufficient for practical PEMWE deployment. The elongated geometry may accelerate lattice oxygen depletion along specific crystallographic planes under LOM-dominated conditions, leading to localized structural collapse. To address these limitations, researchers have adopted strategies such as defect engineering and heteroatom doping to enhance catalytic performance while preserving the one-dimensional structure, as detailed in Section 4.1.1 and Section 4.2.1.

3.2 Two-dimensional RuO_2 nanostructures

Two-dimensional RuO_2 nanostructures, particularly ultrathin nanosheets, represent an ideal platform for maximizing active site exposure and optimizing interfacial charge transfer. Their atomic-scale thickness provides exceptionally high surface-to-volume ratios, ensuring that a large fraction of Ru atoms is surface-accessible and electrochemically active[100,101]. The 2D configuration enables intimate and large-area contact with both the electrode and the electrolyte, guaranteeing faster interfacial charge transfer. Quantum confinement effects in ultrathin RuO_2 nanosheets enhance electron mobility, further improving OER kinetics[42].

Kong *et al*. demonstrated that free-standing 2D Ru nanosheets exhibit high activity toward water splitting, with the ultrathin architecture maximizing the utilization of Ru atoms[101]. Zhao *et al*. reported defect-rich ultrathin RuO_2 nanosheets synthesized via a molten salt method, achieving an overpotential of only 199 mV at 10 mA cm^{-2} and a Tafel slope of 38.2 mV dec^{-1} in 0.5 M H_2SO_4, significantly outperforming commercial RuO_2 (325 mV)[102]. The 2D morphology was essential for achieving high active site density and efficient mass diffusion.

Despite these advantages, 2D RuO_2 faces persistent challenges. Its ultrathin nature makes them particularly susceptible to structural degradation under prolonged OER operation: lattice oxygen depletion along the 2D plane can propagate rapidly, leading to sheet fragmentation and catalyst deactivation. Stacking or restacking of nanosheets during electrode fabrication can reduce the accessible surface area, partially negating the morphological advantages. Limited mass activity and poor durability under high-current-density conditions restrict their industrial viability. These limitations motivate the defect engineering and doping strategies discussed in Section 4.1.2 and Section 4.2.2.

3.3 Three-dimensional RuO_2 nanostructures

Three-dimensional RuO_2 architectures, including hierarchical frameworks, hollow spheres, and porous networks, address the limitations of lower-dimensional structures by integrating interconnected charge transport pathways, high surface areas, and robust mechanical stability. The 3D porosity provides hierarchical mass transport channels for efficient electrolyte penetration and O_2 bubble release, a critical requirement for sustained high-current-density operation. Moreover, the open 3D architecture maximizes atomic utilization by minimizing the proportion of catalytically inactive surfaces that are embedded in supporting materials[103].

Chen *et al*. reported a multi-scale defect RuO_2 bicontinuous nanoreactor (MD-RuO_2-BN) with interpenetrating networks of RuO_2 and pore channels, achieving an overpotential of 196 mV at 10 mA cm^{-2} in 0.5 M H_2SO_4 and maintaining water electrolysis activity for 50 h in a PEMWE single cell, significantly outperforming both K-RuO_2 and commercial RuO_2[104]. The 3D bicontinuous architecture simultaneously provided abundant defect sites, interconnected mass transport pathways, and structural resilience against dissolution.

However, 3D RuO_2 nanostructures also present challenges. Their complex interfaces may create heterogeneous binding sites with inconsistent catalytic behavior. Slower mass transport kinetics in dense 3D networks may partially offset the activity advantages. The synthesis of dimensionally controlled 3D RuO_2 remains challenging, as metastable nanostructures tend to aggregate into thermodynamically favored particles during fabrication[43]. These challenges are addressed through the heterostructure engineering

and interstitial doping strategies discussed in Section 4.3.3 and Section 4.4.3.

Importantly, morphological control alone is insufficient to meet the durability requirements of industrial PEMWE. The inherent activity-stability trade-offs identified above necessitate complementary modification strategies, defect engineering, heteroatom doping, heterostructure construction, and phase engineering, which are systematically discussed in Section 4. These strategies are applied within each dimensional class to further optimize the electronic structure, suppress detrimental LOM pathways, and enhance resistance to Ru dissolution under harsh acidic and high-potential conditions.

The morphological advantages discussed above provide a structural foundation for catalytic performance, yet the intrinsic activity and stability of RuO_2 remain fundamentally governed by its electronic structure. The following section examines how targeted modification strategies, defect engineering, heteroatom doping, and heterointerface construction, can further optimize the electronic and geometric properties of RuO_2 across different dimensional architectures.

4. Regulation Strategies of RuO_2-Based Catalysts

Having established that morphological dimensionality constrains the accessible OER pathways, we now examine how three core modification strategies, defect engineering, heteroatom doping, and heterointerface construction, selectively modulate the electronic structure to shift the mechanism preference. Defect engineering primarily modulates the local coordination environment and creates additional active sites, suppressing LOM by strengthening the Ru-O bond at defect-adjacent sites. Heteroatom doping directly tunes the Ru d-band center and Ru-O covalency through charge redistribution, enabling bidirectional pathway switching (LOM → AEM or AEM → LOM) depending on dopant electronegativity.

Heterointerface construction introduces interfacial charge redistribution and oxygen spillover mechanisms, enabling dual-pathway catalysis (AEM + OPM) that can simultaneously bypass the scaling relation and preserve lattice integrity. Critically, the effectiveness of each strategy is dimensionality-dependent: defect engineering is most effective in 2D architectures where grain boundaries can be densely packed; doping is universally applicable but requires dimensionality-specific optimization of dopant solubility; heterointerface construction is most powerful in 3D architectures where conductive supports provide continuous electron pathways. This strategy-mechanism-dimensionality coupling provides the organizing principle for the following subsections.

Common synthesis routes for RuO_2-based catalysts include solvothermal/hydrothermal methods, electrodeposition, and phosphidation, among others. The catalytic performance of RuO_2-based catalysts in water splitting can be systematically optimized by strategically regulating their electronic structure, interfacial interactions, phase composition, and support architecture. These approaches work synergistically to enhance charge transfer kinetics, fine-tune the adsorption energies of reaction intermediates, and improve structural stability, thereby delivering superior electrocatalytic activity and durability.

The synthesis method fundamentally determines the catalyst's crystal structure, defect chemistry, particle morphology, support interaction, and ultimately its OER performance and durability. However, a catalyst that exhibits exceptional laboratory performance may be entirely impractical for industrial deployment if its synthesis route cannot be scaled reproducibly and cost-effectively. This section provides a systematic horizontal comparison of four representative synthetic routes, hydrothermal synthesis, molten salt method, electrospinning, and *in-situ* calcination, along with two industrially relevant reference methods (Adams fusion and sol-gel/Pechini), evaluating each across six critical dimensions: (1) structural control capability, (2) defect engineering capability, (3) catalyst-support interaction engineering, (4) reproducibility, (5) scalability and cost, and (6) industrial manufacturability.

Hydrothermal synthesis. Ru precursors are dissolved in aqueous solution with structure-directing agents and reacted in a sealed autoclave at 120-250 °C under autogenous pressure for 6-48 h, followed by washing, drying, and post-annealing at 300-600 °C. For example, RuO_2/TiO_2-x (60 wt% RuO_2) via hydrothermal deposition on TiO_2 nanosheets has an η_{10} 218 mV and is stable for 50 h at 10 mA cm^{-2} in 0.5 M H_2SO_4[105]. Hierarchical RuO_2/RuTi/Ti composite via hydrothermal/temperature-varied calcination is stable for 200 h at 500 mA cm^{-2} in PEMWE[106]. **Molten Salt Method.** Ru precursors are mixed with molten salt media (NaCl/KCl, $NaNO_3/KNO_3$, Na_2SO_4/K_2SO_4, or eutectic mixtures) and heated above the salt melting point (typically 300-900 °C) for 0.5-12 h. The molten salt acts as both solvent and structure-directing medium. After reaction, the salt is removed by water washing, and the product is dried. For example, defect-rich ultrathin RuO_2 nanosheets via $NaNO_3$/KCl molten salt have an η_{10} of 194 mV and are stable for 600 h at 10 mA cm^{-2}[107]. **Electrospinning.** A polymer solution (typically PVP, PAN, or PVA in DMF/ethanol) containing Ru precursors and optionally support precursors is electrospun into nanofibers using a high-voltage electric field (10-25 kV) between a spinneret and collector. The as-spun polymer/Ru composite fibers are then calcined at 400-800 °C in air to decompose the polymer and crystallize RuO_2. For example, Ru-RuO_2@Co/CNF bifunctional catalysts are efficient acidic and alkaline overall water splitting[108]. ***In-Situ* Calcination/Thermal Decomposition.** Ru precursors are directly deposited onto a substrate by dip-coating, spray-coating, or brush-painting, followed by thermal decomposition (calcination) at 300-500 °C in air. The Ru precursor decomposes *in-situ* to form RuO_2 directly on the substrate surface. Multiple coating-calcination cycles are often used to build up the desired catalyst loading. For example, RuO_2 on Ti felt via dip-coating/calcination at 350 °C and N-RuO_2/TiN composite via two-step calcination both are directly used as highly active and stable PEMWE anodes[109,110]. **Adams Fusion Method.** $RuCl_3 \cdot Xh_2O$ is mixed with $NaNO_3$ (flux ratio 1:6 to 1:10) and fused at 450-550 °C for 1-3 h. The $NaNO_3$ acts as both an oxidizing agent and a flux medium. After cooling, the product is washed

extensively with water to remove $NaNO_3$ and NaCl byproducts. This is the oldest and most established method for RuO_2/IrO_2 synthesis, widely used as the benchmark preparation method in OER literature[111]. **Sol-Gel/Pechini Method.** Ru precursors are dissolved in a chelating agent and polymerized with ethylene glycol to form a polymeric resin. The resin is dried and calcined at 300-600 °C to decompose the organic matrix and crystallize RuO_2. Based on the aforementioned preparation methods, the advantages and disadvantages of each method are summarized below, as shown in Table 2.

Table 2. The advantages and disadvantages of different preparation methods.

Methods	Advantages	Disadvantages
Hydrothermal	Morphology control\Defect engineering\Heteroatom doping\Low crystallization temperature	Batch-to-batch variability\Limited throughput\Long synthesis time\Solvent waste\Scale-up challenge\Safety concerns
Molten Salt	Unique defect structures\Morphology versatility\Lattice engineering\Short reaction time\No high-pressure equipment	High temperature\Salt residue contamination\Salt waste management
Electrospinning	1D nanostructure\Compositional flexibility\Tunable Ru oxidation state	Carbon support corrosion\Low Ru loading\Calcination-induced structural changes\Reproducibility sensitivity
In-Situ Calcination	Direct electrode fabrication\Strong catalyst-substrate bonding\Simple equipment\Controllable loading	Limited morphology control\Low surface area\Precursor waste
Adams Fusion	Simple\Well-established; produces crystalline RuO_2 with good OER activity	Large $NaNO_3$ consumption\Extensive washing required
Sol-Gel/Pechini	Excellent compositional homogeneity\Tunable particle size via calcination temperature\Compatible with multiple dopants\Lower temperature than Adams fusion\No salt waste	Organic decomposition releases CO_2, CO, NO_x\Long processing time\Batch-to-batch variability in resin crosslinking\Residual carbon contamination possible

Ru: ruthenium; 1D: one-dimensional; OER: oxygen evolution reaction.

Develop hybrid synthesis strategies that combine the strengths of multiple methods. Several promising hybrid approaches have emerged such as hydrothermal and calcination. Hydrothermal growth of RuO_2 nanostructures on TiO_2/Ti substrates, followed by low-temperature calcination (300-400 °C) to strengthen catalyst-substrate bonding without excessive sintering. This combines hydrothermal's structural control with calcination's industrial compatibility. Sol-gel precursor mixing for compositional homogeneity, followed by molten salt calcination for defect engineering. This combines sol-gel's atomic-level mixing with molten salt's unique defect generation. The path from laboratory catalyst discovery to industrial PEMWE deployment requires careful consideration of synthesis route manufacturability based on our comparative analysis.

4.1 Defect modification

4.1.1 Effect of 1D RuO_2-based catalysts

An effective way to improve the activity and stability of RuO_2-based electrocatalysts for the acidic OER is to introduce defect engineering, such as grain boundaries and oxygen vacancies. Introducing defect engineering in one-dimensional RuO_2-based electrocatalysts can adjust the electronic structure and active sites on the catalyst surface. For example, Ru wavy nanowires with an ultrathin feature and many defects were synthesized by a highly universal wet-chemical approach[112]. TEM images (Figure 2a,b,c,d,e) clearly show that Ru NWs exhibit highly wavy morphology with ultrathin diameter and many kinks. The measured lattice distance of only 0.214 nm was shown in the high-resolution TEM (HR-TEM), revealing that the structural feature of Ru NWs is the (002) interface of hcp Ru. After thermal treatment at 250 °C in air for 1 h, a new RuO_2 phase was generated while the overall nanowire morphology was largely preserved. The measured lattice distance of 0.224 nm, corresponding to the (200) interplane of RuO_2, was observed. In addition, many defects around the kinks (red dotted lines) were observed, which can provide additional active sites to enhance performance. The experimental results showed that in 0.5 M H_2SO_4 electrolyte, the electrocatalytic OER performance of RuO_2 NWs is higher than that of other metal NWs (Ir, Pt, Rh) electrocatalysts. The overpotential of RuO_2 NWs is 234 mV at 10 mA cm^{-2} in 0.5 M H_2SO_4, while the commercial Ir/C shows larger overpotentials, as shown in Figure 2f. In addition, Figure 2g shows that the stability of RuO_2 NWs was also evaluated by using continuous galvanostatic measurements with an overpotential change of less than 45 mV in 0.5 M H_2SO_4 during 20 h tests. The research found that water adsorbs onto the Ru sites and gradually decomposes into oxygen, protons, and electron pairs. The key adsorption configurations of the intermediate species in the oxygen evolution reaction include *OOH, *OH, and *O. Thus, RuO_2 NWs follow the AEM pathway. Moreover, the evolution of Gibbs free energy in the OER process indicates that the OER overpotential decreases from 0.73 V to 0.39 V when Ru point defects occur (Figure 2h). Additionally, after

introducing Ru point defects, neighboring Ru atoms form dangling bond connections with oxygen atoms, and more electrons migrate from oxygen atoms to Ru atoms, making their d-band centers closer to the Fermi level, as shown in Figure 2i, thereby optimizing their adsorption free energy and OER overpotential. Zhu *et al.* reported that solid solution Ru-manganese oxide nanowires with oxygen-rich vacancies (O_V) (V-$Ru_xMn_{1-x}O_2$) were used to enhance the activity and durability of acidic OER in RuO_2-based catalysts[113]. SEM reveals that V-$Ru_xMn_{1-x}O_2$ has a wire-like structure, as shown in Figure 2j. TEM image further revealed the wire structure of the V-$Ru_xMn_{1-x}O_2$ NWs and showed that these V-$Ru_xMn_{1-x}O_2$ are composed of V-$Ru_xMn_{1-x}O_2$ sub-nanoparticles (sub-NPs), which provide the V-$Ru_xMn_{1-x}O_2$ NWs with a porous structure (Figure 2k). The high-angle annular dark-field scanning TEM (HAADF-STEM) image in Figure 2l further observed nano-crystalline porous structure of V-$Ru_xMn_{1-x}O_2$ NWs. The O1s spectrum in Figure 2m shows that there is a distinct peak at 531.9 eV, corresponding to O_V. Meanwhile, the electron paramagnetic resonance (EPR) spectra of V-$Ru_xMn_{1-x}O_2$ NWs are presented in Figure 2n. At g = 2.003, different signals can be observed, further verifying that electrons are captured in O_V. The catalytic activity and durability of V-$Ru_xMn_{1-x}O_2$ NWs towards the OER is evaluated in 0.5 M H_2SO_4. **Figures 2**o, p show that the OER catalyzed by the V-$Ru_xMn_{1-x}O_2$ NWs only needs an overpotential of ~ 200.0 mV to drive a current density of 10 mA cm^{-2} and a Tafel slope of 48.97 mV dec^{-1}, which are much lower than those of commercial RuO_2 (Com-RuO_2). The V-$Ru_xMn_{1-x}O_2$ NWs also exhibit excellent durability for the acidic OER, as shown in Figure 2q. Throughout a prolonged acidic OER durability test conducted at 10 mA cm^{-2}, the operating potential remained stable, showing no obvious increase even after 600 h. This proves that the durability of $Ru_xMn_{1-x}O_2$ NWs is much higher than that of Com-RuO_2. Oxygen vacancies are crucial for the excellent OER activity demonstrated by the V- $Ru_xMn_{1-x}O_2$ nanowire catalysts. Analysis of the free energy profile (Figure 2r) identifies the kinetic bottleneck for the OER on the V-$Ru_xMn_{1-x}O_2$ (110) surface: the step involving the evolution of *OOH to molecular oxygen (O_2), and it also indicates that the V-$Ru_xMn_{1-x}O_2$ nanowire follows the AEM reaction pathway. This step presents a low energy barrier of 0.38 eV at U = 1.23 V, which is only about half of the corresponding barrier on RuO_2 (110) (0.76 eV). Interestingly, while the introduction of oxygen vacancies (OVs) lowers the OER barrier in V-$Ru_xMn_{1-x}O_2$ (110) relative to the O_V-free counterpart (0.47 eV), an excessively high O_V concentration is counterproductive. Computational results confirm this, showing that the model with more O_V near the active site (Vmore-$Ru_xMn_{1-x}O_2$ (110)) displays an increased energy barrier. Therefore, the O_V level must be optimized to achieve peak catalytic activity.

Based on the experimental findings, it can be conclusively demonstrated that the strategic implementation of defect engineering plays a pivotal role in enhancing the OER performance of 1D RuO_2-based electrocatalysts in acidic media. By deliberately introducing controlled defects such as oxygen vacancies, cationic vacancies, or lattice distortions, the electronic structure of the catalyst undergoes significant modulation. The optimized structure enables more efficient stabilization and transformation of the key intermediates (*O, *OH, and *OOH) along the OER pathway. This capability is most impactful at the rate-limiting step, effectively alleviating the substantial energy barrier that commonly limits conventional RuO_2 catalysts. Experimental characterization combined with density functional theory calculations indicates that these engineering defects generate local electron-deficient regions and an optimized metal-oxygen coordination environment, effectively reducing the energy barrier of the potential-limiting step. This defect engineering approach not only provides atomic-level insights into the optimization of active sites, but also establishes a scalable framework for designing high-performance electrocatalysts in PEMWE.

4.1.2 Effect of 2D RuO_2-based catalysts

The electronic structure of catalytic active sites is predominantly governed by their surface coordination environments. Introducing defects into catalysts provides a powerful means to tailor both the surface atomic arrangement and the local coordination, thereby modulating the electronic properties for enhanced catalysis[114]. Therefore, precise defect engineering emerges as a pivotal strategy for controllably optimizing the OER performance of 2D RuO_2-based materials. Significant research efforts have consequently been directed toward harnessing defects to enhance their electrocatalytic efficacy. He *et al.* reported a grain-boundary-rich porous nanosheet (GB-RuO_2) as an excellent acidic OER electrocatalysis by salt-assisted recrystallization, and the schematic routes for synthesizing GB-RuO_2 porous nanosheet rich in grain boundaries are shown in Figure 3a[57]. The structural characteristics of GB-RuO_2 nanosheets were systematically investigated through advanced microscopy techniques. Initial morphological examination via TEM revealed a distinctive porous nanosheet architecture, as demonstrated in Figure 3b. HR-TEM analysis further elucidated the nanoscale organization, showing that these porous structures consist of interconnected nanoparticles averaging 4.5 ± 0.3 nm in diameter. Crystallographic characterization exposed significant boundary features within the nanosheets, particularly highlighted in Figure 3c where dotted lines demarcate prevalent grain boundaries. Subsequent magnification of these regions (Figure 3d,e,f,g) provided detailed visualization of both grain boundaries and twin boundaries at atomic resolution. These microscopic investigations collectively confirm the successful synthesis of two-dimensional RuO_2 nanostructures exhibiting dual critical features: an ultrathin profile with inherent porosity, coupled with a high density of structural discontinuities in the form of grain boundaries. This unique combination of morphological and crystallographic properties positions GB-RuO_2 NS as a promising candidate for advanced catalytic applications. Atomic force microscopy (AFM) measurements quantitatively determined the ultrathin nature of the material, with a measured thickness of approximately 3.0 nm (Figure 3h). The electrochemical performance and stability of the catalysts were systematically evaluated in **Figure** 3i,j,k. As demonstrated by the linear sweep voltammetry (LSV) profiles and corresponding Tafel analysis in Figure 3i,j, the GB-RuO_2 catalyst achieved superior OER activity, requiring an overpotential of merely 187 mV to reach 10 mA cm^{-2} alongside an exceptionally low Tafel slope of 34.5 mV dec^{-1}. This performance markedly surpasses both commercial RuO_2

(η_{10} = 252 mV, 66.1 mV dec^{-1}) and amorphous RuO_2 (η_{10} = 211 mV, 64.4 mV dec^{-1}), highlighting the structural advantages of the GB-RuO_2 architecture. The enhanced catalytic efficiency is attributed to its unique nanostructure comprising ultrasmall nanograins and ultrathin porous nanosheets, which collectively maximize the exposure of electrochemically active sites through optimized surface area utilization. Long-term stability assessments (Figure 3k) further confirm the robustness of GB-RuO_2, exhibiting a minimal potential decay of 46 mV during continuous operation at 10 mA cm^{-2} over 140 hours. In stark contrast, both commercial and amorphous RuO_2 counterparts demonstrate rapid performance degradation, failing within 13 h and 40 h respectively under identical testing conditions. This pronounced durability difference underscores the critical role of grain boundary engineering and nanostructure design in stabilizing catalytic activity during prolonged electrochemical operation. DEMS coupled with ^{18}O isotope labeling is a powerful operando technique for identifying the oxygen source in evolved O_2, thereby distinguishing between AEM and LOM pathways. DEMS was employed to investigate the influence of grain boundaries on the OER mechanism of GB-RuO_2. This methodology involved isotopic labelling of the catalyst surface with ^{18}O, enabling precise tracking of oxygen sources during the OER process through real-time monitoring of evolved O_2 species. The detection of $^{34}O_2$ (comprising one ^{18}O and one ^{16}O atom) would indicate lattice oxygen-mediated pathway activation, as it requires oxygen exchange between lattice oxygen (^{18}O) and water-derived oxygen (^{16}O from $H_2{}^{16}O$). As illustrated in Figure 3l, the predominant oxygen species detected was $^{32}O_2$ (^{16}O-^{16}O), with complete absence of $^{36}O_2$ (^{18}O-^{18}O) signals. This isotopic distribution pattern provides compelling experimental evidence that grain boundaries effectively suppress lattice oxygen participation in the OER process. The observed inhibition of oxygen exchange mechanisms strongly suggests that GB-RuO_2 predominantly follows the adsorbate evolution mechanism pathway during OER, where oxygen intermediates are derived exclusively from water molecules rather than the metal oxide lattice. This fundamental mechanistic shift accounts for the enhanced catalytic stability of GB-RuO_2, as suppression of lattice oxygen involvement mitigates structural degradation typically associated with LOM pathways in RuO_2-based oxide catalysts. The ^{18}O-DEMS methodology employed for GB-RuO_2 exemplifies a broader trend in the field toward using isotope labeling to unambiguously assign OER mechanisms. Complementary operando EIS and ATR-SEIRAS FTIR measurements on GB-RuO_2 further confirmed that grain boundaries stabilize lattice oxygen by modulating the local electronic environment, as evidenced by the absence of lattice oxygen activation features in the operando Raman spectra even at potentials up to 1.6 V *vs*. RHE[57]. In addition, Zhao *et al*. developed a rapid and facile molten salt method for the fabrication of defect-rich ultra-thin RuO_2 NSs as OER catalysts, as shown in Figure 3m[102]. The as-synthesized RuO_2 nanosheets exhibit a characteristic two-dimensional morphology with lateral dimensions extending to several micrometers, as demonstrated in Figure 3n. These RuO_2 NSs display pronounced electron beam transparency, a hallmark of their ultrathin structural nature. Cross-sectional analysis (Figure 3o) reveals an interlayer spacing of approximately 1.6 nm between adjacent nanosheets, as highlighted in the inset. High-resolution STEM imaging (Figure 3p) discloses a polycrystalline architecture with randomly oriented nanograins, delineated by distinct grain boundaries (indicated by green guidelines). Atomic-resolution characterization (Figure 3q) further exposes abundant multiscale structural imperfections within the RuO_2 NSs, including dislocations and intergranular boundaries. Significantly, HAADF-STEM analysis identifies high-density ruthenium vacancy sites (marked by blue dashed circles in Figure 3r,s), manifested as localized intensity reductions in the atomic column contrast. These intrinsic structural defects, spanning from atomic-scale vacancies to mesoscopic grain boundaries-collectively modulate the local electronic environment of the RuO_2 NSs, thereby exerting substantial influence on their catalytic performance. The electrocatalytic OER performance of RuO_2 NSs was systematically compared with annealed RuO_2 NSs and commercial RuO_2 nanoparticles through LSV analyses normalized to geometric surface area, Ru mass loading, and electrochemical active surface area (ECSA), as illustrated in Figure 3t. Notably, the pristine RuO_2 NSs exhibit superior catalytic activity, requiring merely 199 mV overpotential to achieve a geometric current density of 10 mA cm^{-2}. This represents a significant improvement over both annealed RuO_2 NSs (244 mV, 55 mV higher) and commercial RuO_2 nanoparticles (325 mV, 126 mV higher). The enhanced performance is further corroborated by Tafel analysis (inset of Figure 3t), where the RuO_2 NSs demonstrate a slope of 38.2 mV dec^{-1}, approaching the theoretical 40 mV dec^{-1} value associated with the *OOH intermediate formation as the rate-determining step. In contrast, the annealed RuO_2 NSs (54.1 mV dec^{-1}) and commercial counterpart (71.2 mV dec^{-1}) display slopes closer to 60 mV dec^{-1}, indicative of an alternative rate-limiting oxygen coupling mechanism involving the *O intermediate. Long-term stability assessments via chronopotentiometry (Figure 3u) reveal exceptional durability for RuO_2 NSs, exhibiting minimal potential increases of 10 mV and 32 mV during 6 h of operation at 1 and 10 mA cm^{-2}, respectively. This stability markedly surpasses that of commercial RuO_2 nanoparticles, which suffer rapid activity degradation within 2,200 seconds at 1 mA cm^{-2} (Figure 3u inset). The combined metrics of low overpotential, favorable Tafel kinetics, and robust stability position the unannealed RuO_2 NSs as a superior OER catalyst, with performance enhancements attributed to their optimized nanostructure and preserved active sites compared to thermally treated or commercial counterparts. Density functional theory investigations were conducted to elucidate the role of Ru vacancies in modulating the OER activities on RuO_2 (110) and RuO_2 (100) surfaces. As illustrated in Figure 3v, pristine RuO_2 (110) and RuO_2 (100) surfaces exhibit OER overpotentials of 0.82 V (A1) and 0.79 V (B1), respectively, primarily constrained by the energetically unfavorable formation of *OOH intermediates during the potential-determining step (*O + H_2O → *OOH + H^+ + e^-) in the AEM pathway. This kinetic limitation arises from the strong Ru^{5c}-*O chemical interaction and the intrinsic scaling relationship between *OH and *OOH adsorption energies. Notably, the introduction of Ru^{5c} vacancies adjacent to active sites substantially enhances OER performance, reducing the overpotentials to 0.54 V and 0.45 V for RuO_2 (110) and RuO_2 (100) surfaces, respectively, corresponding to significant decreases of 0.28 V and 0.34 V compared to their defect-free counterparts. As demonstrated in Figure 3w, the vacancy-induced electronic structure modification effectively weakens the *O binding strength relative to *OOH, thereby lowering

the activation energy barrier for the *O to *OOH transition. This mechanistic alteration optimizes the reaction thermodynamics and substantially improves the overall OER catalytic efficiency on both crystallographic surfaces.

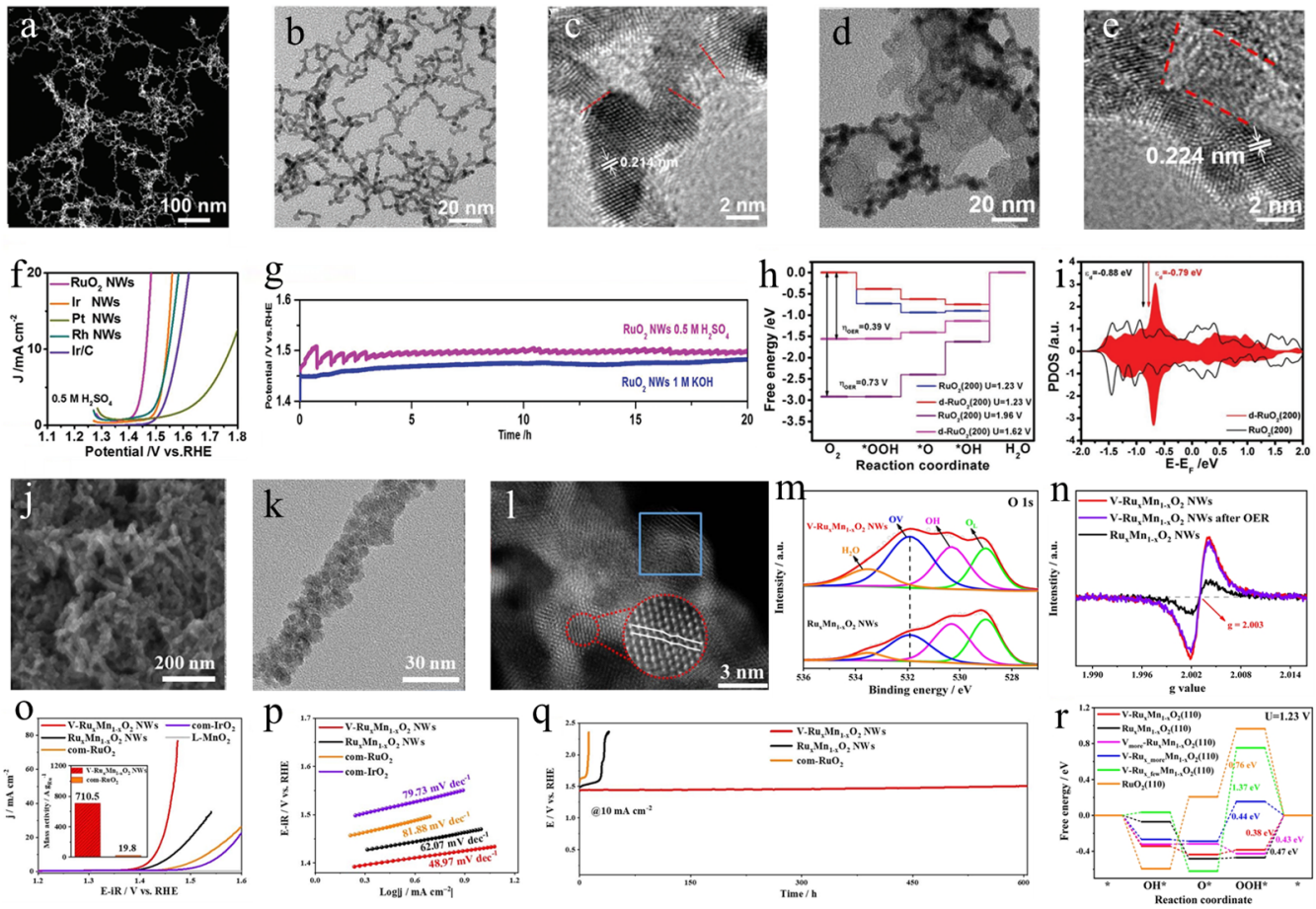


Figure 2. (a) HAADF-STEM image; (b) TEM image and (c) HR-TEM image of the Ru NWs; (d) TEM image; (e) HAADF-STEM images of the RuO_2 NWs obtained from Ru NWs after heat treatment; (f) OER activities of different electrocatalysts in 0.5 M H_2SO_4; (g) chronopotentiometry curves of RuO_2 NWs in 0.5 M H_2SO_4 at 5 mA cm^{-2}; (h) The free energy profiles of OER processes on perfect and defected RuO_2-(200) surface under an acidic environment while considering the effect of the equilibrium potential (U = 1.23 V) and the applied electrode potential; (i) The d orbital distribution of the Ru-atom site on pristine and defect RuO_2-(200) surface (marked by green color). Reproduced with permission from reference[112]. Copyright © 2018 John Wiley & Sons; (j) SEM; (k) TEM; (l) HAADF-STEM image of V-$Ru_xMn_{1-x}O_2$ NWs; XPS spectra of (m) O 1 s; (n) EPR spectra; (o) Polarization curves; The inset shows the mass activity of the catalysts at an overpotential of 240.0 mV; (p) Tafel slopes; (q) Chronopotentiometry curves; (r) Free energy diagram of the OER. Reproduced with permission from reference[113]. Copyright © 2023 Royal Society of Chemistry. TEM: transmission electron microscopy; HAADF-STEM: high-angle annular dark-field scanning TEM; HR: high-resolution; NWs: nanowires; OER: oxygen evolution reaction; SEM: scanning electron microscope; XPS: X-ray photoelectron spectroscopy; EPR: electron paramagnetic resonance.

Defect engineering has proven to be a powerful strategy for enhancing the performance of 2D RuO_2-based electrocatalysts. Structural defects, including grain boundaries, nanocrystalline grains, and atomic-scale vacancies, modulate the electronic structure, suppress the LOM pathway, and reduce the energy barrier for the *O-to-*OOH transition, thereby synergistically enhancing both catalytic activity and stability. Grain boundaries, as structural discontinuities, not only increase the surface area and expose more active sites but also suppress lattice oxygen participation, which is often associated with structural degradation. Instead, they promote the AEM, enabling stable and efficient OER kinetics. The presence of ultrathin porous nanosheets and interconnected nanoparticles further enhances the accessibility of electrochemically active sites, ensuring optimal utilization of the surface area. Atomic-level defects, such as Ru vacancies, further enhance OER performance by weakening the binding strength of oxygen intermediates and reducing the activation energy barrier for critical rate-determining steps. High-density vacancies disrupt the intrinsic scaling relationship between *OH and *OOH adsorption energies, thereby optimizing the reaction thermodynamics. Collectively, these multiscale defects spanning from atomic-scale vacancies to mesoscopic grain boundaries synergistically enhance the catalytic efficiency of RuO_2 nanostructures, making them highly promising candidates for advanced electrocatalytic applications.

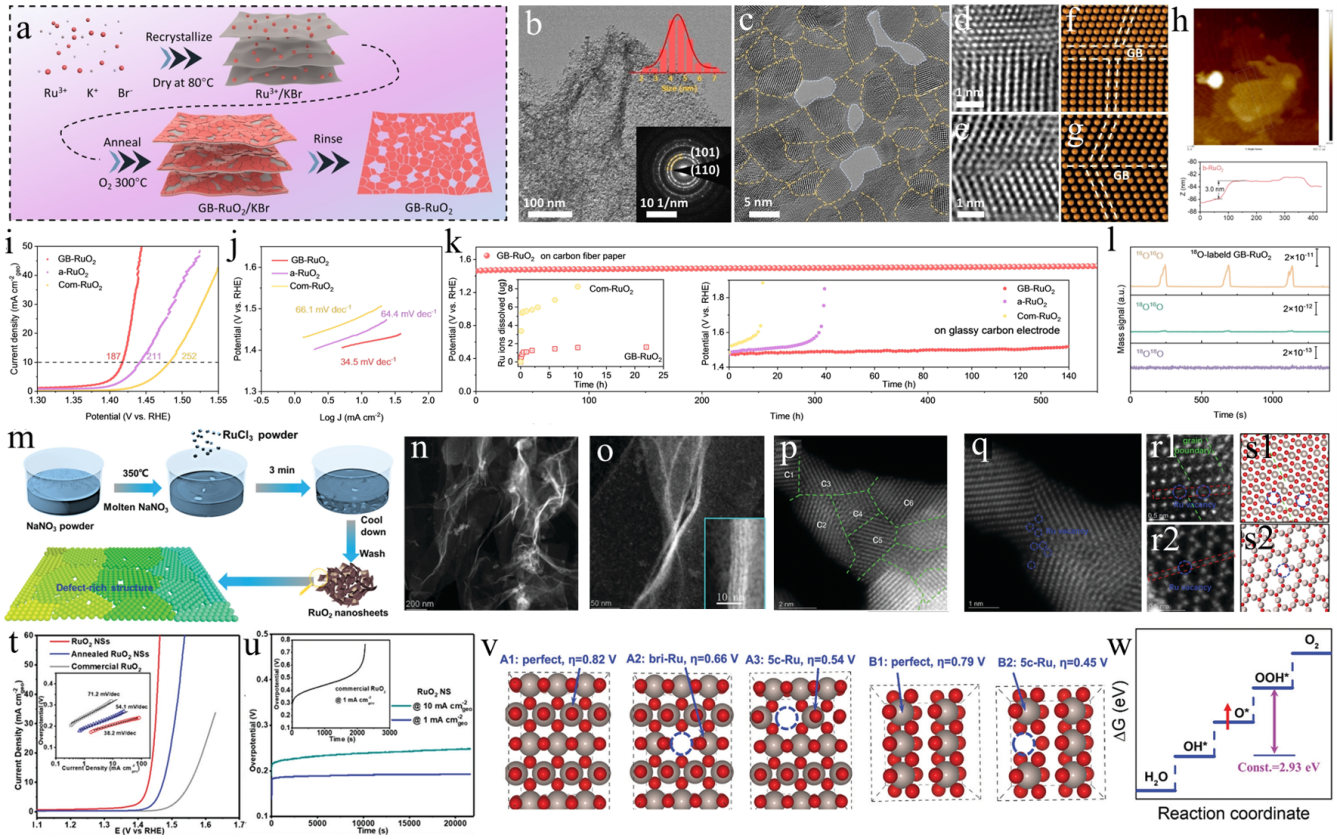


Figure 3. (a) The schematic routes for synthesizing GB-RuO_2 porous nanosheet rich in grain boundaries; (b) TEM images; (c) HR-TEM images of GB-RuO_2; The corresponding SAED image and grain size profile of GB-RuO_2 illustrated in (b); (d, e) High-magnification images; (f, g) Simulated structure of grain boundary; (h) AFM images of GB-RuO_2; The bottom shows their thickness; (i) Electrocatalytic OER performance; (j) Tafel slopes of GB-RuO_2, a-RuO_2 and Com-RuO_2 in 0.1 M $HClO_4$; (k) CP tests of GB-RuO_2, a-RuO_2 and Com-RuO_2 on glassy carbon electrode (illustration on the right) and carbon paper at 10 mA cm^{-2} in 0.1 M $HClO_4$; Time dependent ion dissolution of Com-RuO_2 and GB-RuO_2 during OER (illustration on the left); (l) DEMS signals of O_2 products for ^{18}O-surface labelled GB-RuO_2, in the 0.1 M $HClO_4$ using $H_2{}^{16}O$ as solvent. Reproduced with permission from reference[57]. Copyright © 2024 John Wiley & Sons; (m) Schematic illustration for the synthesis procedure of the RuO_2 NSs; (n, o) STEM images of RuO_2 NSs at a lower magnification with different view directions; (p) Representative high-resolution STEM images of the RuO_2 NSs; the dashed line points out the grain boundaries; (q, r) Atomic STEM images of the RuO_2 NSs; (s) The corresponding atomic models of (r); (t) OER polarization curves and the corresponding Tafel plots of the electrocatalysts in O_2-saturated 0.5 M H_2SO_4; (u) Chronopotentiometry test of the RuO_2 NSs at a current density of 1 and 10 mA cm_{geo}^{-2} for 6 h; the inset shows the chronopotentiometry test of commercial RuO_2 nanoparticles at 1 mA cm_{geo}^{-2}; (v) Two-dimensional volcano plot constructed using the descriptors of ΔG_{*O}-ΔG_{*OH} and ΔG_{*OOH}-ΔG_{*O}; (w) Schematic showing the origin of OER activity improvement upon introducing a Ru vacancy. Reproduced with permission from reference[102]. Copyright © 2020 Royal Society of Chemistry. Insets show the configurations of O-terminated RuO_2 (110) and RuO_2 (100) surfaces where the Ru vacancy and active sites are marked by a dashed circle and arrow, respectively; A and B denote the RuO_2 (110) and RuO_2 (100) surfaces, respectively. The spheres colored in brown and red represent Ru and O atoms, respectively. CP: corresponding chronopotentiometry; TEM: transmission electron microscopy; HR: high-resolution; SAED: selective area electron diffraction; AFM: atomic force microscopy; OER: oxygen evolution reaction; DEMS: differential electrochemical mass spectrometry; STEM: scanning TEM; NSs: nanosheets.

4.1.3 Effect of 3D RuO_2-based catalysts

Owing to the critical issue of insufficient stability, the practical deployment of RuO_2 in acidic OER remains challenging. Consequently, significant research has been directed toward improving the long-term stability of RuO_2-based catalysts. Designing ultra-small and defective 3D RuO_2-based electrocatalysts is a promising strategy for achieving excellent OER stability in acidic media. Yan *et al.* reported a novel approach, which involves the carbon nanotube (CNT) support, the carbon coating, and defect engineering, to improve the catalytic activity and stability of RuO_2 for the acidic OER[115]. The ultrathin nitrogen doped carbon (NC) coated oxygen-vacancy rich RuO_2 nanoparticles (NPs) supported on the CNTs (NC@Vo-RuO_2/CNTs-350) are synthesized through a controlled calcination in air, as shown in Figure 4a. The NC@Vo-RuO_2/CNTs-350 catalyst maintains exceptional stability in acidic OER, exhibiting negligible activity loss after continuous operation for over 900 h. A typical TEM image of the NC@Vo-RuO_2/CNTs-350 hybrid (Figure 4b) reveals the successful growth of RuO_2 NPs on CNT supports. HR-TEM analysis (Figure 4c) demonstrates the well-defined crystallinity of these RuO_2 NPs, exhibiting distinct lattice fringes corresponding to the (110), (101), and (211) crystallographic planes characteristic of rutile-structured RuO_2. X-ray photoelectron spectroscopy (XPS) characterization provides critical insights into the chemical states of the composite. The deconvoluted Ru $3p_{3/2}$ spectrum (Figure 4d) shows two peaks at 462.8 eV and 465.7 eV, corresponding to Ru^{4+} and

Ru^{3+} species, respectively. The unambiguous detection of Ru^{3+} serves as direct evidence for the presence of oxygen vacancies (V_O) in the RuO_2 lattice. This conclusion is further corroborated by the O 1s spectrum analysis (Figure 4e), which reveals multiple oxygen-containing components: lattice oxygen (O_L) in RuO_2 at 529.7 eV, oxygen species adjacent to Vo sites at 531.2 eV, Ru-OH bonds ($\approx$ 530.5 eV), C = O/C-O functional groups at 532.0 eV, and surface-adsorbed oxygen-containing species such as physisorbed H_2O. The coexistence of these oxygen states, particularly the Vo-associated component, provides complementary verification of oxygen vacancy formation in the RuO_2 structure. A low overpotential (η_{10}) of approximately 170.0 mV is required for the NC@Vo-RuO_2/CNTs-350 catalyst to reach 10 mA cm^{-2} in acidic OER, as confirmed by LSV (Figure 4f), underscoring its superior activity. This performance is further corroborated by Tafel analysis, which provides critical insights into the reaction kinetics and mechanistic behavior of the catalyst. The exceptional stability of NC@Vo-RuO_2/CNTs-350 is underscored by chronopotentiometry measurements (Figure 4g), revealing a minimal overpotential increase of < 15 mV over an extended OER operation period exceeding 900 h. In stark contrast, control catalysts, including c-RuO_2, Vo-RuO_2/CNTs-350, Vo-RuO_2/CNTs-400, and Vo-RuO_2-500, exhibit complete activity loss after 9, 28, 299, and 189 h of testing, respectively. Such a remarkable disparity in stability strongly implicates the pivotal role of the ultrathin NC shell encapsulating the RuO_2 NPs. The NC layer effectively mitigates chemical corrosion of the active RuO_2 NPs under harsh acidic OER conditions, thereby preserving structural integrity and catalytic functionality. This study establishes a robust structure-stability correlation, emphasizing the significance of protective carbon-based architectures in enhancing the durability of oxide-based electrocatalysts for acidic water oxidation.

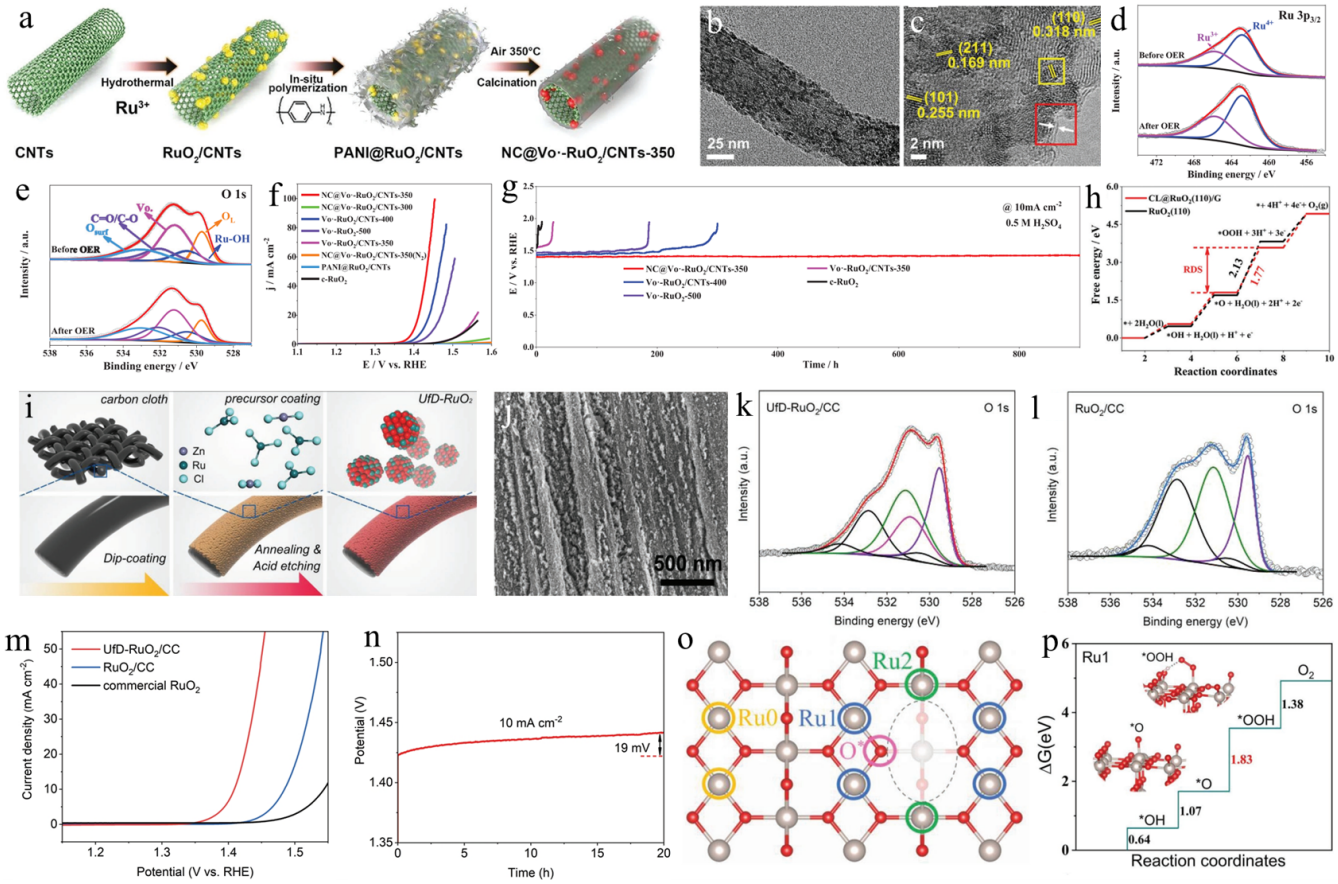


Figure 4. (a) Synthesis illustration of NC@Vo··-RuO_2/CNTs-350; (b) TEM; (c) HR-TEM of the NC@Vo··-RuO_2/CNTs-350; XPS spectra of (d) Ru 3p; (e) O 1 s for NC@Vo··-RuO_2/CNTs-350 before and after the OER test; (f) OER polarization curves; (g) Chronopotentiometry curves of the catalysts; (h) Free energy diagram of the OER. Reproduced with permission from reference[115]. Copyright © 2023 John Wiley & Sons; (i) Illustration of the synthetic route for the UfD-RuO_2/CC; (j) SEM images of UfD-RuO_2/CC; XPS spectra of UfD-RuO_2/CC in the (k) O 1s regions and that of RuO_2/CC in the (l) O 1s regions; (m) Polarization curves of UfD-RuO_2/CC, RuO_2/CC, and commercial RuO_2/CC after capacitance-correction and iR-correction; (n) Stability test of UfD-RuO_2/CC at a fixed potential of 1.42 V. All experiments were carried out in 0.5 m H_2SO_4 (o) Top view of defective RuO_2 structure. Gray and red spheres present Ru and O atoms, respectively; (p) The calculated free-energy profiles of OER on the Ru1 sites. Reproduced with permission from reference[116]. Copyright © 2019 John Wiley & Sons. NC: nitrogen-doped carbon; CNT: carbon nanotube; TEM: transmission electron microscopy; HR: high-resolution; XPS: X-ray photoelectron spectroscopy; OER: oxygen evolution reaction; CC: carbon cloth; Ru: ruthenium.

The calculation and analysis of the OER free energy curve for the CL@RuO_2 (110)/G system based on the AEM reaction pathway identifies the *O to *OOH conversion as the rate-determining step, with an associated energy barrier of 1.77 eV (Figure 4h). This thermodynamic limitation contrasts favorably with the pristine RuO_2 (110) system, which demonstrates a substantially higher energy

barrier of 2.13 eV for the same potential-limiting step in its OER pathway. The marked reduction in activation energy (Δ_E = 0.36 eV) directly correlates with enhanced catalytic performance, providing a theoretical foundation for the experimentally observed superior OER activity of NC@Vo-RuO_2/CNTs-350 compared to conventional c-RuO_2. This comparative analysis underscores the critical role of structural optimization in CL@RuO_2 (110)/G for facilitating the energetically demanding *OOH formation process, thereby improving overall catalytic efficiency in oxygen evolution processes. As depicted in Figure 4i, Ge *et al*. employed dip coating followed by annealing and acid etching to synthesize carbon cloth (CC)-supported ultrafine RuO_2 nanoparticles with abundant defects[116]. As shown in the SEM image (Figure 4j), UfD-RuO_2 nanoparticles are homogeneously distributed across the carbon cloth substrate. Furthermore, deconvolution of the O 1s XPS spectra (Figure 4k,l) identifies multiple chemical environments, providing insight into the material's composition. Deconvolution of the spectra identifies characteristic peaks at 529.5 eV corresponding to lattice oxygen (Ru-O) in the RuO_2 crystalline structure, accompanied by spectral features at 531.1 eV that are conventionally assigned to satellite transitions and surface-bound hydroxyl species (Ru-OH). Notably, the UfD-RuO_2/CC composite exhibits an additional spectral component centered at 530.9 eV, which displays a positive binding energy shift relative to the lattice oxygen signal. This emergent peak aligns with prior reports attributing such features to oxygen vacancy defects in transition metal oxides. The observed chemical shift can be rationalized by the modified electronic environment surrounding oxygen atoms proximal to these defect sites, consistent with the formation of under-coordinated oxygen species in vacancy-rich systems. The electrochemical performance of UfD-RuO_2/CC for the OER demonstrates marked superiority over its RuO_2/CC counterpart, as evidenced by comparative polarization analyses. A substantially lowered overpotential of 179 mV is sufficient for the UfD-RuO_2/CC electrode to reach 10 mA cm^{-2}, as shown in Figure 4m, demonstrating its exceptional catalytic activity. In contrast, conventional RuO_2/CC requires a significantly higher overpotential of 254 mV to attain the same current density, highlighting the performance enhancement enabled by the UfD structural modification. Long-term stability evaluation under galvanostatic operation at 10 mA cm^{-2} reveals the robust durability of UfD-RuO_2/CC, with a marginal overpotential increment of 19 mV observed over 20 h of continuous operation (Figure 4n). This operational stability notably surpasses that of UfD-RuO_2 deposited on glassy carbon electrodes (GCE), a distinction attributed to the enhanced mechanical integration between the UfD-RuO_2 catalyst layer and the conductive CC substrate. The three-dimensional CC architecture effectively mitigates catalyst delamination during vigorous gas evolution, thereby maintaining structural integrity and electrochemical interface stability throughout prolonged electrocatalytic processes. Comprising both six- and five-coordinated Ru atoms, the pristine RuO_2 (110) surface features unsaturated five-coordinated sites (Ru0, Figure 4o), which act as the catalytically active centers. Computational analysis of free energy profiles (Figure 4p) reveals that the potential-determining step corresponds to the transformation from *O to *OOH intermediates, and it also follows the AEM reaction pathway. Notably, the Ru2 site, originally six-coordinated, undergoes structural modification to participate in catalytic processes. For the critical *O to *OOH transition, the Ru1 site demonstrates a significantly reduced energy barrier of 1.83 eV, representing a 0.25 eV improvement compared to the Ru0 site. This enhanced activity is partially attributed to the strengthened hydrogen-bond interaction between the *OOH intermediate's hydrogen atom and adjacent two-coordinated oxygen species. Furthermore, density functional theory calculations elucidate that surface defects not only generate additional active sites but also modulate the electronic configuration of pre-existing five-coordinated Ru atoms, thereby synergistically optimizing both catalytic site availability and intrinsic activity. Collectively, these results reveal an atomic-scale mechanistic understanding of the structure-activity correlation in RuO_2-based electrocatalysts.

In addition to the nanoparticle-on-support architecture, designing intrinsically three-dimensional RuO_2 frameworks with hierarchical porosity represents a more fundamental approach to maximizing active site accessibility and mass transport efficiency. Chen *et al*. reported a multi-scale defect RuO_2 bicontinuous nanoreactor (MD-RuO_2-BN) synthesized via a molten salt-assisted strategy using KCl-LiCl as the molten salt medium at 500 °C[104]. The bicontinuous architecture features interpenetrating networks of RuO_2 and pore channels, creating a double-continuous structure that simultaneously provides: (1) abundant defect sites including Ru vacancies, O vacancies, and interatomic boundaries confirmed by HR-TEM and XRD; (2) interconnected mass transport pathways for efficient electrolyte penetration and O_2 bubble release; and (3) structural resilience against dissolution under high current density conditions. Theoretical simulations reveal that low-coordination Ru atoms at defect sites not only enhance catalytic activity but also effectively inhibit lattice oxygen oxidation and high-valent Ru dissolution through weakened Ru-O interaction. The MD-RuO_2-BN catalyst achieves a low overpotential of 196 mV at 10 mA cm^{-2} in 0.5 M H_2SO_4. Notably, when integrated into a PEMWE single cell, the MD-RuO_2-BN-based electrolysis maintains water electrolysis activity for 50 h, while both K-RuO_2 and commercial RuO_2 experience a clear decline within only 25 h. This work demonstrates that the bicontinuous nanoreactor architecture, which intrinsically integrates defect engineering with 3D hierarchical porosity, offers superior performance compared to simply depositing defective nanoparticles onto external supports.

A cross-dimensional comparison of defect engineering reveals that the stability enhancement factor scales inversely with the dimensionality-dependent lattice oxygen mobility. In 1D V-$Ru_xMn_{1-x}O_2$ nanowires, oxygen vacancies lower the OER barrier (0.38 eV *vs*. 0.76 eV for pristine RuO_2 (110)) but an excessively high O_V concentration is counterproductive, increasing the energy barrier, a finding that establishes the critical principle of optimal defect density. In 2D GB-RuO_2, grain boundaries suppress LOM by modulating the local electronic environment, as confirmed by ^{18}O-DEMS showing complete absence of $^{34}O_2$ signals, providing the most direct mechanistic evidence among all defect engineering studies. In 3D NC@Vo-RuO_2/CNTs-350, the carbon coating provides physical protection that complements the electronic effect of oxygen vacancies, achieving 900 h stability that far exceeds what electronic

modulation alone can deliver. This comparison reveals a fundamental insight: the stability contribution from defect engineering transitions from predominantly electronic (1D) to predominantly structural/mechanical (3D) as dimensionality increases. In 1D, defects modulate the electronic structure to optimize intermediate adsorption; in 2D, grain boundaries create local electronic environments that suppress lattice oxygen activation; in 3D, the defect-engineered nanoparticles require additional physical protection (carbon coating, support confinement) to achieve industrial relevant stability. This dimensional transition has a critical implication: defect engineering alone is insufficient for 3D architectures, it must be combined with protective strategies (carbon coating, support confinement) to achieve the stability required for PEMWE deployment. The 900 h stability of NC@Vo-RuO_2/CNTs-350 versus the < 30 h stability of uncoated Vo-RuO_2/CNTs-350 provides the most compelling evidence for this conclusion.

4.2 Doping modification

4.2.1 Effect of 1D RuO_2-based catalysts

The deliberate doping of foreign elements, particularly transition metals, serves as a powerful method to boost catalytic performance. This improvement stems from the intentional modulation of the catalyst's electronic structure. A prime example is 1D RuO_2 doped with elements like Fe, Mn, Co, or Pt, whose altered electronic configuration results in superior activity and durability relative to pristine RuO_2[60,62,117,118]. For example, Liu *et al*. reported the preparation of a new class of Te-RuO_2 porous nanotubes through a template-based procedure, with the key steps depicted in Figure 5a[119]. The porous nanotube structure is retained in Te-RuO_2, as inherited from the original Te/$RuTe_2$ hybrids. TEM results (Figure 5b) confirm this morphology, showing nanotubes with an approximate diameter of 40 nm and wall thickness of 6 nm. As indicated by the HAADF-STEM image in Figure 5c, a minor lattice strain is observed in the (101) planes, a distortion ascribed to the incorporation of Te atoms. Moreover, the inset of Figure 5c presents the electron energy loss spectroscopy (EELS) spectrum acquired from a randomly chosen nanotube. This spectrum corroborates the presence of Te atoms within the Te-RuO_2 nanotube structure. The Te-RuO_2 nanotubes exhibit remarkable OER activity and stability in acidic media (0.1 M $HClO_4$). In detail, Te-RuO_2 exhibits a low overpotential of merely 171 mV to achieve a current density of 10 mA cm^{-2}. This value is significantly lower than those required by P-RuO_2 (205 mV) and C-RuO_2 (302 mV), representing reductions of 34 mV and 131 mV, respectively (Figure 5d). Chronopotentiometry measurements at 10 mA cm^{-2} (Figure 5e) demonstrate that the Te-RuO_2 nanotubes exhibit excellent stability, with a mere 95 mV overpotential increase after 50 h of continuous operation, outperforming both P-RuO_2 and C-RuO_2. The Gibbs free energy changes of the RuO_2 and Te-RuO_2 models in different models, and free energies of four elementary steps at different constant potentials were calculated, confirming that the doping of Te can effectively enhance the intrinsic activity of the RuO_2 nanotubes (Figure 5f). Among these, the activated *OOH intermediates exhibits the highest value, which is the rate-determining step, and the Te-RuO_2 nanotubes demonstrate the reaction mechanism of AEM. As shown in Figure 5f, doping Te into the RuO_2 lattice reduces the free energy barrier by approximately 0.29 eV relative to pristine RuO_2 (101). This lowered barrier indicates more favorable OER energetics on the Te-RuO_2 (101) surface. Collectively, these findings demonstrate that Te incorporation optimizes the reaction energetics, leading to superior acidic OER performance of the modified RuO_2 catalyst. The results of density of states (DOS) indicate that the DOS of Te-RuO_2 (101) near the Fermi level is much higher than that of RuO_2 (Figure 5g). The d-band center theory suggests that a higher electron density near the Fermi level strengthens the adsorption of key OER intermediates (*OH, *O, and *OOH). This enhanced adsorption thus facilitates the overall OER kinetics. On the other hand, leveraging the high electrical conductivity and vacant 3d orbitals of transition metals, doping them into 1D RuO_2 frameworks presents an effective method to engineer electrocatalysts with enhanced performance for water splitting. Madhu *et al*. reported the development of Co-doped RuO_2 nanorods, with a corresponding synthesis schematic shown in Figure 5h[120]. As evidenced by the field-emission SEM (FE-SEM) and HR-TEM images in Figure 5i,j, Co-RuO_2 exhibits an aggregated structure composed of nanorods. Energy-dispersive X-ray spectroscopy (EDS) mapping analysis confirms that all expected elements (Co, Ru, O, and C) are uniformly dispersed throughout the rod-like Co- RuO_2 structure (Figure 5k). The homogeneous color mapping further indicates the absence of other elemental impurities. This result proves that Co was successfully mixed into the 1D RuO_2 structure. From the LSV results (Figure 5l), Co-RuO_2 demonstrates superior OER activity, requiring an overpotential of only 328 mV to reach 10 mA cm^{-2}, which is lower than that of RuO_2 (342 mV) and significantly lower than Co_3O_4 (600 mV). The Tafel slopes for Co-RuO_2, RuO_2, and Co_3O_4 are 74, 91, and 168 mV dec^{-1}, respectively (Figure 5m). The lowest value for Co- RuO_2 corresponds to faster interfacial electron transfer kinetics compared to the other catalysts. Moreover, long-term durability testing at 10 mA cm^{-2} for 24 h in 0.5 M H_2SO_4 confirms the highly stable nature of the Co-RuO_2 catalyst, with minimal activity degradation, as shown in Figure 5n. XPS analysis confirmed the possible effect of Co on the enhancement of OER kinetics (Figure 5o,p). In Co-doped RuO_2, the Ru 3d XPS peak shifts positively by 0.23 eV, a change attributed to reduced electron density on Ru^{4+}. This electronic modulation thereby facilitates the binding of reactive species (H_2O or OH^-), leading to enhanced OER kinetics at a reduced overpotential relative to pure RuO_2.

Recent experimental investigations and theoretical calculations have demonstrated that the strategic incorporation of heteroatom dopants into catalysts significantly enhances the electrocatalytic performance of 1D RuO_2 nanostructures in acidic OER systems. Through systematic doping engineering, the modified catalyst achieves optimized Gibbs free energy landscapes by precisely regulating the adsorption/desorption energetics of oxygen-containing intermediates on active sites. This optimization is accompanied by substantial electronic structure modulation, as evidenced by XPS and density functional theory simulations, which reveal enhanced charge transfer capabilities and optimized d-band center positioning. The synergistic effects between

heteroatom-induced lattice strain and electronic redistribution collectively contribute to remarkable improvements in both catalytic activity and stability. These findings provide critical insights into the design principles of advanced electrocatalysts for PEMWE, addressing the long-standing challenges of catalyst dissolution and sluggish kinetics in strongly acidic OER environments.

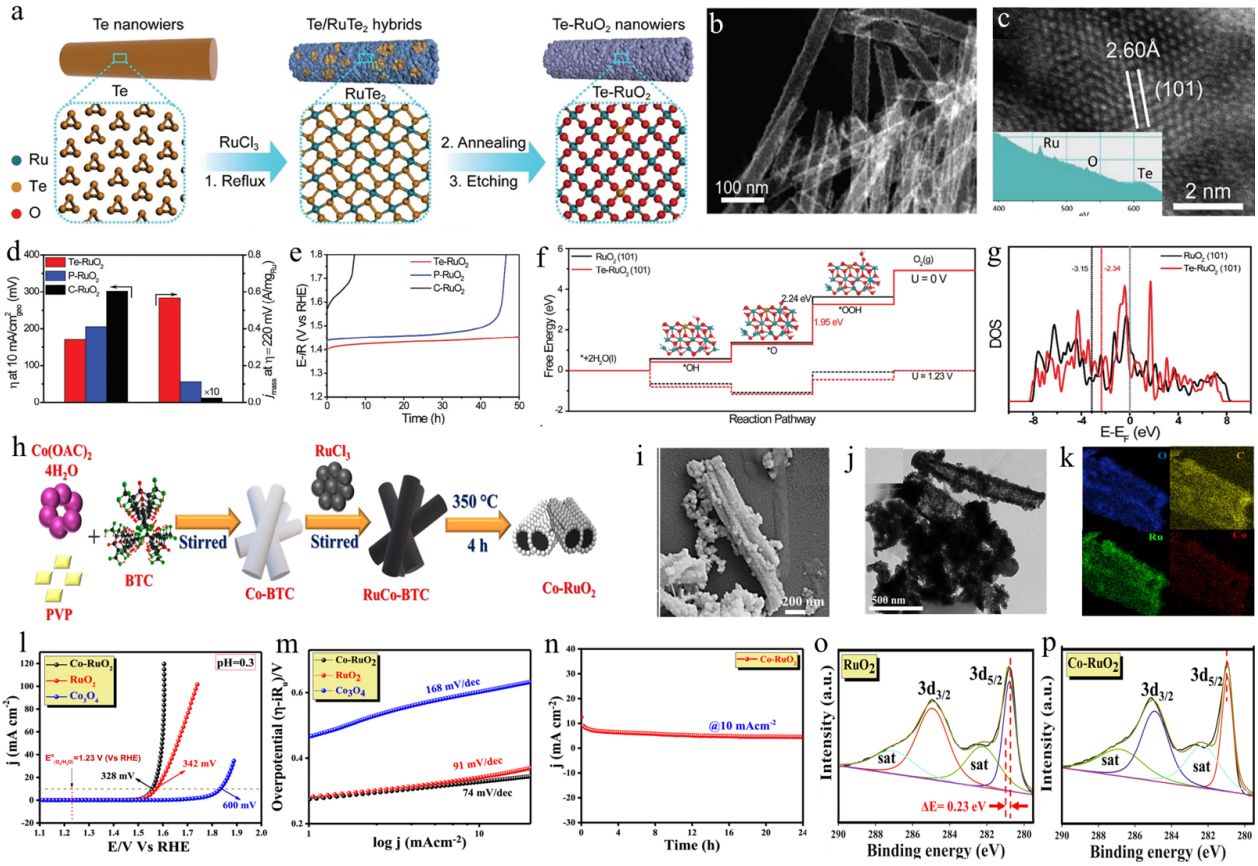


Figure 5. (a) Schematic illustration of the preparation of Te-RuO_2 nanotubes; STEM image (b) and the atomic resolution STEM image (c) of Te-RuO_2 nanotubes; The inset in (c) is the EELS analysis; (d) Overpotential at 10 mA cm^{-2} and mass activity at 220 mV for Te-RuO_2, P-RuO_2, and C-RuO_2; (e) Chronopotentiometry performance under a constant current density of 10 mA cm^{-2} up to 50 h; (f) The calculated free energy diagrams for Te-RuO_2 (101) and RuO_2 (101); (g) The calculated free energy diagrams for Te-RuO_2 (101) and RuO_2 (101). Reproduced with permission from reference[119]. Copyright © 2023 Wiley-VCH GmbH; (h) Schematic representation of the formation of Co-RuO_2 nanorods; (i) FE-SEM images of Co-RuO_2; (j) Low- to high-magnified HR-TEM images of Co-RuO_2; (k) color mapping results of mixed elements Co, Ru, O, and C, respectively; (l) LSV polarization curves of the nanorod-like Co-RuO_2, RuO_2, and Co_3O_4 catalysts at a scan rate of 5 mV s^{-1} in 0.5 M H_2SO_4; (m) Tafel plots; (n) chronoamperometric analysis of Co-RuO_2 for 24 h; (o, p) Deconvoluted XPS spectrum of the Ru 3d orbital for both RuO_2 and Co-RuO_2. Reproduced with permission from reference[120]. Copyright © 2021 American Chemical Society. Ru: ruthenium; STEM: scanning transmission electron microscopy; EELS: electron energy loss spectroscopy; FE-SEM: field-emission SEM; HR: high-resolution; LSV: linear sweep voltammetry; XPS: X-ray photoelectron spectroscopy.

4.2.2 Effect of 2D RuO_2-based catalysts

Doping with foreign elements has been demonstrated to be an effective strategy for improving stability, primarily by widening the energy gap between the O 2p orbitals and the Fermi level[121]. The research and application of doping with foreign elements in 2D RuO_2-based electrocatalysts have also achieved great results[95]. For example, Liu *et al.* reported a novel Pd-doped RuO_2 catalyst comprising two-dimensional nanosheets formed by stacked nanoparticles, which was synthesized via a salt-template-assisted method (Figure 6a)[42]. The structural and compositional characteristics of the $Pd_{0.08}Ru_{0.02}O_2$ catalyst were systematically investigated through advanced characterization techniques. As revealed by TEM and HAADF-STEM analyses (Figure 6b,c), the material exhibits a well-defined two-dimensional nanosheet architecture. EDS quantification demonstrated excellent agreement between the measured Pd/Ru atomic ratio (0.08:0.92) and the precursor stoichiometry (Figure 6d), confirming precise compositional control and successful Pd incorporation into the host matrix. Notably, X-ray diffraction analysis (Figure 6e) revealed that the Pd doping process preserves the fundamental rutile-type crystal structure, with Pd atoms substituting Ru sites within the characteristic M-O_6 octahedral framework. This structural retention highlights the compatibility of Pd dopants with the parent RuO_2 lattice while maintaining the essential coordination geometry required for catalytic functionality. The electrochemical performance evaluation (Figure 6f) revealed significant differences in OER kinetics among the catalysts. Notably, at a current density of 10 mA cm^{-2}, the measured overpotentials demonstrated a distinct activity hierarchy: $Pd_{0.08}Ru_{0.92}O_2$ (204 mV) < RuO_2 NSs (226 mV) < commercial RuO_2 (Com-RuO_2) (308 mV). This

progression highlights the crucial role of morphological engineering, where the 2D architecture and nanoscale dimensions of RuO_2 NSs substantially enhance charge transfer efficiency compared to conventional Com-RuO_2. The remarkable 22 mV overpotential reduction achieved through Pd doping in $Pd_{0.08}Ru_{0.92}O_2$ exemplifies the electronic modulation effect induced by noble metal incorporation. This strategic doping alters the local electronic environment of Ru active sites, potentially optimizing the adsorption/desorption energetics of oxygen-containing intermediates during OER, a phenomenon consistent with previous studies on transition metal oxide modifications. The enhanced catalytic performance aligns with established principles of alloying effects in electrocatalysis, where heteroatom introduction modifies d-band center positions and surface reactivity. Furthermore, the exceptional operational stability of $Pd_{0.08}Ru_{0.92}O_2$ under sustained electrolysis at 10 mA cm^{-2} (Figure 6g) underscores the structural reinforcement provided by Pd integration. This durability enhancement likely originates from improved corrosion resistance and mitigated surface reconstruction during prolonged operation, critical advantages for practical water electrolysis applications. The combined improvements in both activity and stability position Pd-Ru oxide hybrids as promising candidates for advanced electrocatalytic systems. Through density functional theory calculations, the electronic structure modulation induced by Pd incorporation into RuO_2 was systematically investigated, with particular emphasis on the Ru 4d orbitals. As illustrated in Figure 6h, the analysis of the DOS spectra unveiled a distinct shift in the Ru 4d band (ed) from 1.08 eV in pristine RuO_2 to 1.15 eV in the $Pd_{0.08}Ru_{0.92}O_2$ system. The upward shift of the Ru d-band center leads to a widened energy gap between the Ru 4d states and the Fermi level. This electronic modification thereby fine-tunes the adsorption strength of oxygen intermediates on the active sites. Furthermore, based on the AEM reaction pathway, the Gibbs free energy (Δ_G) profiles for the OER pathways, presented in Figure 6i, demonstrated that the potential-determining step (PDS) for all examined catalysts resides in the transition between *OOH and *O intermediates. Comparative analysis revealed a substantial reduction in the PDS energy barrier from 1.82 eV for RuO_2 to 1.74 eV for the $Pd_{0.08}Ru_{0.92}O_2$ catalyst. This marked decrease in activation energy underscores the critical role of Pd co-doping in optimizing the adsorption/desorption equilibrium of reactive species, which is essential for enhancing the overall OER kinetics. The synergistic electronic regulation achieved through Pd incorporation thus emerges as a pivotal strategy for tailoring the catalytic performance of Ru-based oxide systems. A key challenge for Ru-based electrocatalysts is their instability, which originates from lattice oxygen (O_L) oxidation and oxygen vacancy (O_V) generation. Therefore, a primary design goal is to stabilize the O_L and suppress O_V formation. Elemental doping offers an effective route to achieve this, leading to simultaneous improvements in activity and durability[123]. A trace S-doped RuO_2-based nanosheet (Ru/S NSs-400) with a thickness of 2.5 nm by the thiol-assisted strategy was successfully prepared[122]. As illustrated in Figure 6j, HAADF-STEM characterization demonstrates the characteristic curled nanosheet morphology of the Ru/S NSs-400 material. Quantitative elemental analysis via SEM-EDS (Figure 6k) reveals a Ru: S atomic ratio of 92.4:7.6, indicating substantial S removal during thermal processing. X-ray diffraction analysis (Figure 6l) confirms the preservation of the rutile RuO_2 crystal structure in the Ru/S NSs-400 material. Cross-sectional thickness measurements across two representative regions (Figure 6m,n,o) yield values of 2.7 nm and 2.4 nm, respectively, confirming the formation of ultrathin nanostructures. These structural features collectively suggest effective morphological control during the synthesis process, with thermal treatment promoting both structural refinement and elemental composition optimization. With a remarkably low overpotential of merely 219 mV to achieve 10 mA cm^{-2}, the Ru/S NSs-400 catalyst demonstrates exceptional activity for the acidic OER, as shown in Figure 6q. This performance significantly outperforms its counterparts, including Ru/S NSs-250 (275 mV), Ru/S NSs-500 (252 mV), and the benchmark Ir/C catalyst (309 mV), underscoring its superior efficiency in lowering the energy barrier for OER. Beyond catalytic activity, long-term stability is a critical parameter for evaluating Ru-based OER catalysts under acidic conditions. Remarkably, chronopotentiometry measurements reveal that Ru/S NSs-400 maintains exceptional stability over 600 h of continuous operation at 10 mA cm^{-2}, exhibiting negligible current density decay (Figure 6p). In stark contrast, the commercial Ir/C catalyst undergoes rapid deactivation within just 5 h under identical conditions. Notably, the durability of Ru/S NSs-400 surpasses all previously reported Ir-free Ru-based OER catalysts, positioning it as a groundbreaking candidate for sustainable water splitting technologies. This unprecedented stability, combined with high activity, highlights its transformative potential for advancing cost-effective and durable electrolysis systems. In contrast to pristine RuO_2, which exhibits a d-band center positioned at -3.34 eV, the Ru/S NSs-400 catalyst demonstrates a notable negative shift in its d-band center to -3.62 eV (Figure 6s). This downward displacement relative to the Fermi level arises from the synergistic effects of S incorporation and oxygen vacancy (O_V) formation. This electronic structure engineering reduces the binding energy of oxygen intermediates to the Ru active centers, thereby facilitating the oxygen evolution reaction by diminishing its free energy barrier. As established, the intermediate products involved in the AEM reaction pathway are *OH, *O, and *OOH. The density functional theory simulations based on this further elucidate the atomic-level mechanism underlying the enhanced OER activity induced by S doping. Comparative analysis reveals that S doping substantially lowers the PDS energy barrier to 1.77 eV, corresponding to a reduced overpotential of 0.54 V (Figure 6t). The improved catalytic performance originates from the downward shift of the Ru d-band center upon S substitution. Owing to S lower electronegativity compared to oxygen, S atoms withdraw electron density from Ru centers during bonding, inducing a redistribution of Ru's d-orbital electrons away from the Fermi level. This electronic structure modification enables self-regulation of intermediate adsorption/desorption energetics on Ru active sites. The optimized adsorption strength of OER species directly correlates with the diminished PDS energy barrier, providing a fundamental electronic rationale for the catalytic enhancement observed in S-doped RuO_2 systems (Figure 6u). Collectively, these findings establish a structure-activity relationship wherein strategic anion doping tailors d-band electronic states to optimize reaction pathways in transition metal oxide electrocatalysts.

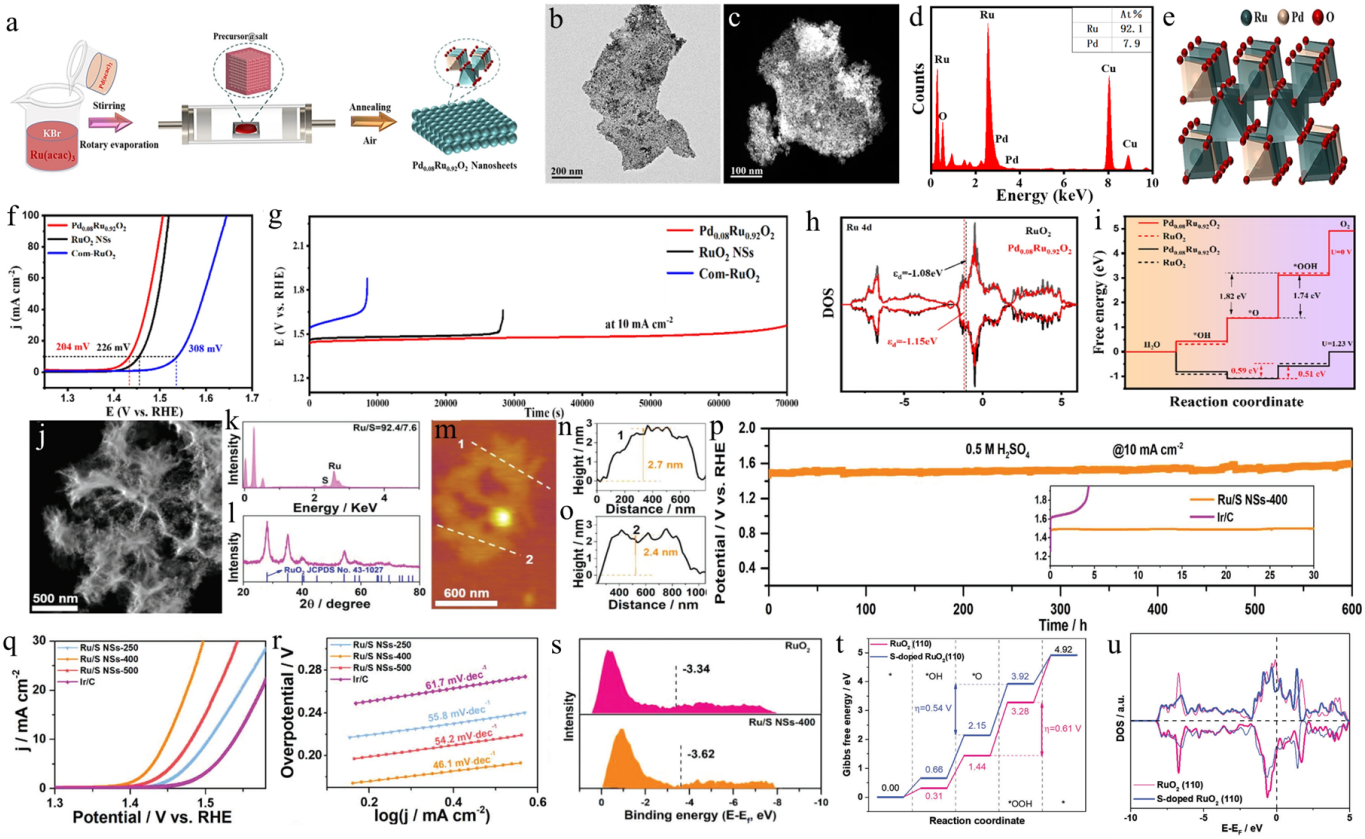


Figure 6. (a) Schematic route for the synthesis of $Pd_{0.08}Ru_{0.92}O_2$; (b) TEM images; (c) HAADF-STEM image; (d) EDS pattern of $Pd_{0.08}Ru_{0.92}O_2$; (e) Crystal structure model of rutile $Pd_{0.08}Ru_{0.92}O_2$; (f) LSV polarization curves with 95% iR compensation of $Pd_{0.08}Ru_{0.92}O_2$, RuO_2 NSs, and Com-RuO_2; (g) Chronopotentiometry curves of $Pd_{0.08}Ru_{0.92}O_2$, RuO_2 NSs, and Com-RuO_2; (h) DOS plots of Ru 4d states in RuO_2 and $Pd_{0.08}Ru_{0.92}O_2$; (i) Gibbs free-energy diagram for RuO_2 and $Pd_{0.08}Ru_{0.92}O_2$. Reproduced from reference[42]. CC BY 4.0; (j) HAADF-STEM image; (k) SEM-EDS; (l) XRD pattern; (m) AFM image; (n, o) corresponding height profiles; (p) Chronopotentiometry curves of Ru/S NSs-400 and Ir/C at 10 mA cm^{-2}; The inset in (p) is the enlarged chronopotentiometry curves at the initial stage; (q) LSV curves; (r) Tafel slopes; (s) Surface valence band photoemission spectra of Ru/S NSs-400 and commercial RuO_2; (t) Comparisons of free energy evolution diagrams on RuO_2 and S-doped RuO_2; (u) The projected d orbitals of the active Ru atoms with and without S doping. Reproduced with permission from reference[122]. Copyright © 2023 Wiley-VCH GmbH. TEM: transmission electron microscopy; HAADF-STEM: high-angle annular dark-field scanning TEM; EDS: energy-dispersive X-ray spectroscopy; LSV: linear sweep voltammetry; Ru: ruthenium; NSs: nanosheets; DOS: density of states; SEM: scanning electron microscope; AFM: atomic force microscopy.

Clearly, the hybridization doping of foreign elements is conducive to regulating the electronic structure on the surface of the 2D RuO_2-based electrocatalyst, making the d-band center closer to the Fermi level. Moreover, foreign element doping 2D RuO_2 would self-adjust the adsorption of the OER species and is responsible for the lower energy barrier of PDS, which boosts the OER activity and stability in an acidic medium. Collectively, these findings underscore the importance of foreign element doping in tailoring the properties of RuO_2-based electrocatalysts, offering a promising avenue for the development of advanced, cost-effective, and sustainable water splitting technologies.

4.2.3 Effect of 3D RuO_2-based catalysts

Due to the characteristic that the incorporation of foreign elements can effectively regulate the electronic structure of RuO_2-based catalysts, it has also been widely studied in 3D structure design, such as ultra-small Sn-RuO_2 nanoparticles[124], Sr, Cr co-doped RuO_2[125] and Cu-doped RuO_2 hollow porous polyhedral structures[126]. Owing to the optimized surface configuration and altered electronic structure, these catalysts display a remarkable OER performance. For instance, Wang *et al.* reported that the single-site Pt-doped RuO_2 hollow nanospheres (SS Pt-RuO_2 HNSs) were applied as high-performance electrocatalysts for overall acidic water splitting[127]. The structural characteristics of the synthesized SS Pt-RuO_2 HNSs were systematically investigated through advanced microscopic analysis. As revealed by the TEM image in Figure 7a, the sample exhibits a successfully formed hollow spherical structure. High-resolution elemental mapping reveals a distinctive atomic distribution where Pt atoms exist predominantly as isolated species, evidenced by discrete bright spots in Figure 7b. Detailed atomic-scale line profile analysis of selected regions (Figure 7c,d,e,f,g,h) provides conclusive evidence for the monodispersed incorporation of Pt atoms within the RuO_2 matrix. Crystallographic examination through fast Fourier transform (FFT) patterns (Figure 7d) identifies the predominant exposure of (110) and (101) crystallographic planes along the [111] zone axis, consistent with the tetragonal RuO_2 structure. Crucially, the

atomic-resolution structural model (Figure 7e) demonstrates that Pt atoms exclusively occupy Ru lattice positions while maintaining the host oxide's tetragonal symmetry, confirming the single-site substitution mechanism. This atomic-level substitution pattern preserves the parent oxide's structural integrity while introducing isolated Pt active sites, a critical feature for catalytic applications requiring precise atomic configuration control. The SS Pt-RuO_2 HNSs demonstrate exceptional OER performance, as evidenced by their remarkably low overpotential of 228 mV to achieve a current density of 10 mA cm^{-2} (Figure 7i). Comparative analysis reveals that the SS Pt-RuO_2 HNSs exhibit the smallest Tafel slope among the evaluated catalysts, including RuO_2 HNSs, and commercial RuO_2, indicating accelerated reaction kinetics for OER. A comprehensive evaluation of catalytic activity parameters, particularly overpotentials and Tafel slopes, confirms the superior OER performance of SS Pt-RuO_2 HNSs over both RuO_2-based counterparts. Furthermore, long-term stability tests highlight a critical advantage of the SS Pt-RuO_2 HNSs: their overpotential remains stable over 100 h of continuous operation, in stark contrast to commercial RuO_2, which suffers from rapid performance degradation characterized by a sharp increase in overpotential within approximately 2 h (Figure 7j). This pronounced stability enhancement positions SS Pt-RuO_2 HNSs as a promising candidate for sustainable electrochemical applications requiring durable OER catalysts. As illustrated in Figure 7k, the *O dissociation energy of SS Pt-RuO_2 HNSs exhibits a substantial 1.22 eV elevation compared to pristine RuO_2, demonstrating enhanced lattice oxygen stability that effectively mitigates oxidative dissolution during electrocatalytic operation. Projected density of states (PDOS) analysis (Figure 7m) reveals a key electronic structure difference: the Ru 4d orbitals in Pt-RuO_2 are notably closer to the Fermi level than in pure RuO_2. This shift optimizes electron transfer during oxygen evolution, further substantiating the structural enhancement. The thermodynamic advantage is quantitatively confirmed through PDS calculations, revealing reduced energy barriers with Δ_G values of 1.738 eV for SS Pt-RuO_2 HNSs versus 2.02 eV for undoped RuO_2 (Figure 7l). This indicates that the catalytic reaction pathway of SS Pt-RuO_2 HNSs is AEM, and it has better reaction kinetics. These coordinated electronic and energetic modifications, achieved through single-atom Pt doping and interstitial carbon engineering, synergistically enhance both catalytic activity and operational durability, as evidenced by exceptional stability during 100 h continuous operation in PEMWE. In addition, a simple sol-gel method was employed to construct a La-doped RuO_2 catalyst featuring a Ru-O-La asymmetric configuration, aimed at modulating electron redistribution. The electron redistribution can be adjusted and the excessive oxidation at the Ru center can be eliminated, thereby improving the performance of RuO_2, as shown in Figure 7n[128]. The morphological and structural characteristics of RuO_2 and La-doped $La_xRu_{1-x}O_2$ were systematically investigated through advanced electron microscopy techniques. SEM analysis (Figure 7o) revealed that both RuO_2 and $La_xRu_{1-x}O_2$ maintain nanoparticle configurations, indicating that controlled La doping does not significantly alter the morphological characteristics of the RuO_2 matrix. This observation was further corroborated by TEM studies, which demonstrated comparable nanoparticle morphologies for both $La_{0.1}Ru_{0.9}O_2$ (Figure 7c) and pristine RuO_2 (Figure 7p). Quantitative analysis of the TEM images established an average particle size of 3.54 ± 0.61 nm for the $La_{0.1}Ru_{0.9}O_2$ sample. Crystallographic evaluation through selective area electron diffraction (SAED) patterns (Figure 7q) confirmed the polycrystalline nature of $La_{0.1}Ru_{0.9}O_2$, with diffraction rings corresponding to the characteristic lattice planes of RuO_2. This structural consistency suggests that La incorporation preserves the fundamental crystalline architecture of the host material. Complementary chemical analysis via EELS detected distinct La M-edge signals in the $La_{0.1}Ru_{0.9}O_2$ spectrum, providing direct evidence for successful lattice integration of La atoms into the RuO_2 framework. Collectively, these multimodal characterizations confirm that strategic La doping achieves atomic-level substitution while maintaining the structural integrity and nanoscale morphology of the RuO_2 system. The LSV profiles presented in Figure 7r demonstrate the OER activities of $La_xRu_{1-x}O_2$ solid solutions compared to commercial RuO_2 and synthesized RuO_2. Among the investigated catalysts, $La_{0.1}Ru_{0.9}O_2$ emerges as the most electrochemically efficient material, achieving a current density of 10 mA cm^{-2} at a notably low overpotential of 188 mV. This performance surpasses those of its compositional analogues: $La_{0.05}Ru_{0.95}O_2$ (228 mV), $La_{0.2}Ru_{0.8}O_2$ (249 mV), and $La_{0.3}Ru_{0.7}O_2$ (558 mV). Furthermore, the optimized $La_{0.1}Ru_{0.9}O_2$ catalyst demonstrates superior catalytic efficiency relative to both laboratory-synthesized RuO_2 (235 mV) and commercial RuO_2 benchmarks (270 mV), highlighting the critical role of La incorporation in enhancing OER activity within this material system. Furthermore, chronopotentiometry measurements demonstrate that $La_{0.2}Ru_{0.8}O_2$ maintains stable operation at 10 mA cm^{-2} with significantly lower potential increase compared to pristine RuO_2, confirming the enhanced durability conferred by La incorporation (Figure 7s). The doping of La induces a notable shift in the oxygen 2p band center toward the Fermi level, as evidenced in Figure 7t. This electronic structure modification effectively narrows the energy separation between the Ru 4d band center and the O 2p band center, thereby strengthening the Ru-O covalent character. Such enhanced covalency serves dual functions: it mitigates lattice oxygen participation in the OER process while concurrently improving the structural integrity of the $La_{0.1}Ru_{0.9}O_2$ catalyst. These synergistic effects create favorable conditions for the AEM pathway to dominate during acidic OER operation. Comparative free energy profiles (Figure 7u) reveal critical differences in reaction pathways between $La_{0.1}Ru_{0.9}O_2$ and pristine RuO_2, and $La_{0.1}Ru_{0.9}O_2$ follows the AEM reaction path. Both systems share the *OOH formation step as the rate-determining step (RDS), yet the La-doped catalyst demonstrates a substantially reduced energy barrier of 1.802 eV compared to RuO_2 of 1.998 eV. This 0.196 eV reduction in activation energy provides quantitative evidence for the crucial role of Ru-O-La asymmetric configurations in catalytic enhancement. The structural distortion introduced by La substitution likely optimizes intermediate adsorption energetics while maintaining charge transfer efficiency, ultimately accounting for the improved OER performance under acidic conditions.

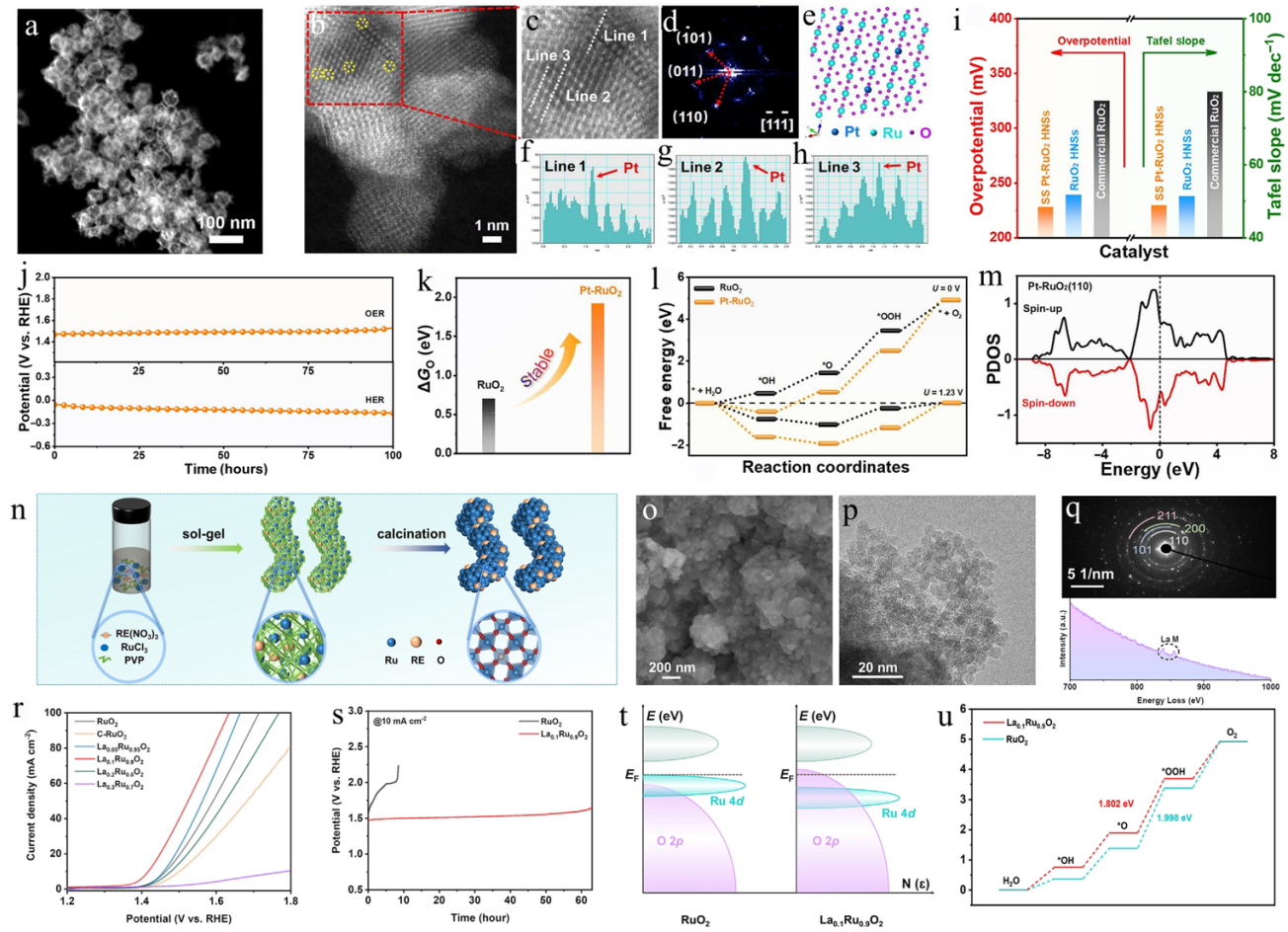


Figure 7. (a) HAADF-STEM image; (b) high-resolution HAADF-STEM image of SS Pt-RuO_2 HNSs; (c) High-resolution HAADF-STEM image obtained from the area highlighted with red rectangles in (b); (d) FFT pattern; (e) crystal structure model of SS Pt-RuO_2 HNSs; (f, g, h) Line-scanning intensity profile obtained from the area highlighted with white lines in (c); (i) Histogram of overpotentials at 10 mA cm^{-2} and Tafel slopes of various catalysts; (j) Chronopotentiometry tests of SS Pt-RuO_2 HNS for OER and HER in 0.5 M H_2SO_4 at 10 mA cm^{-2}; RHE; (k) The calculated dissociation energy of *O in RuO_2 and Pt-RuO_2, respectively; (l) The free energy profiles of OER process on RuO_2 and SS PtRuO_2 HNSs under the applied overpotential of 0 and 1.23 V (RHE), respectively; (m) The PDOS of 4d orbitals of surface Ru atoms in Pt-RuO_2. Reproduced from reference[127]. CC BY 4.0; (n) Schematic of RE-RuO_2 preparation (RE: La, Ce, Pr, Nd, Sm, and Eu); Morphological characterization of $La_{0.1}Ru_{0.9}O_2$; (o) SEM image; (p) TEM image; (q) SAED and EELS patterns; (r) LSV curves at 10 mA cm^{-2} and current densities at 1.6 V of commercial RuO_2, RuO_2, and $La_xRu_{1-x}O_2$; (s) Chronopotentiometry curves of RuO_2 and $La_{0.1}Ru_{0.9}O_2$ at 10 mA cm^{-2}; (t) Schematic band structure of RuO_2 and $La_{0.1}Ru_{0.9}O_2$; (u) Reaction free energy of the acidic OER on RuO_2 and $La_{0.1}Ru_{0.9}O_2$. Reproduced from reference[128]. CC BY 4.0. TEM: transmission electron microscopy; HAADF-STEM: high-angle annular dark-field scanning TEM; FFT: fast Fourier transform; OER: oxygen evolution reaction; HER: hydrogen evolution reaction; RHE: reversible hydrogen electrode; PDOS: projected density of states; SEM: scanning electron microscope; SAED: selective area electron diffraction; EELS: electron energy loss spectroscopy; LSV: linear sweep voltammetry; Ru: ruthenium.

Due to the characteristic that the incorporation of foreign elements can effectively regulate the electronic structure of RuO_2-based catalysts, it has also been widely studied in 3D structure design. A representative example is the Cu-doped RuO_2 hollow porous polyhedra reported by Su *et al.*, which were synthesized through a facile one-step annealing of a Ru-exchanged Cu-BTC metal-organic framework (MOF) derivative[126]. This MOF-templated strategy is particularly advantageous for constructing 3D hollow architectures, as the Cu-BTC polyhedral morphology is faithfully replicated during the Ru exchange and subsequent thermal decomposition process. The resulting Cu-RuO_2 hollow porous polyhedra are composed of ultrasmall nanocrystals that assemble into a well-defined polyhedral shell with abundant mesopores. This unique 3D architecture provides multiple structural benefits: (1) the hollow interior and porous shell enable efficient electrolyte penetration and rapid O_2 bubble release, critical for sustained high-current-density operation; (2) the ultrasmall nanocrystal building blocks maximize the density of exposed active sites while maintaining structural coherence; and (3) the Cu dopants modulate the electronic structure of Ru active sites, optimizing the adsorption energetics of OER intermediates. The Cu-RuO_2 hollow porous polyhedra exhibit a low overpotential of 188 mV at 10 mA cm^{-2} in 0.5 M H_2SO_4 and demonstrate remarkable stability for 8 h of continuous operation, significantly outperforming commercial RuO_2. This work establishes MOF-templated synthesis as a versatile route for constructing 3D doped RuO_2 hollow architectures that synergistically combine morphological and electronic advantages. In addition, ultra-small Sn-RuO_2 nanoparticles

supported on N-doped carbon polyhedra ($Sn_{0.1}$-RuO_2@NCP) were developed through a similar MOF-derived strategy, achieving an overpotential of 178 mV at 10 mA cm^{-2} and maintaining stability for 150 h[124]. The Sr, Cr co-doped RuO_2 system demonstrates that synergistic co-doping can simultaneously activate Sr sites and buffer Cr effects on RuO_2 electronic structures, yielding an overpotential of 214 mV with 300 h stability[125].

A systematic comparison across all doping studies reveals a unifying principle: the dopant electronegativity relative to Ru determines the direction of pathway switching. Dopants more electronegative than Ru (e.g., Pt, Pd) withdraw electron density, downshift the Ru d-band center, weaken Ru-O covalency, and suppress LOM in favor of AEM, enhancing stability at moderate activity cost. Dopants less electronegative than Ru (e.g., S, La) induce a more complex electronic redistribution: S doping downshifts the d-band center through anion-induced charge transfer, while La doping narrows the ε_d-ε_p separation through O 2p band center upshift. Both effects strengthen Ru-O covalency paradoxically while suppressing lattice oxygen participation through structural distortion, a mechanism distinct from simple electronegativity-based predictions. This reveals a critical gap in the current theoretical framework: the d-band center model alone cannot predict pathway switching when dopants induce simultaneous electronic and structural modifications. A more comprehensive descriptor incorporating both ε_d shift and local geometric distortion is needed. Furthermore, comparing the stability outcomes across dopants reveals a striking correlation: catalysts with demonstrated ^{18}O-DEMS evidence for AEM dominance consistently exhibit superior stability to those where pathway switching is inferred only from improved stability or DFT calculations. This observation reinforces our earlier recommendation that operando mechanistic evidence should be a prerequisite for claims of LOM suppression.

4.3 Coupling modification

4.3.1 Effect of 1D RuO_2-based catalysts

The unique synergistic effects at hetero-interfaces serve as a key driver for performance enhancement. Constructing composite heterostructures that incorporate 1D RuO_2 with other components is therefore highly effective in boosting both electrocatalytic activity and stability. In addition, the electrocatalytic performance of the composite material will be further enhanced through the effective electron transfer between different components. Therefore, constructing advanced heterostructures through powerful synergistic effects and electronic effects provides an effective approach for improving the electrocatalytic performance of 1D RuO_2, notably its activity and long-term stability. Inspired by those findings, Samanta *et al*. developed IrO_2-decorated RuO_2 nanowires anchored on a carbon support via a straightforward synthetic approach[129]. The TEM images of IrO_2-RuO_2/C, as shown in Figure 8a,b, reveal that small nanoparticles are interspersed among the randomly aligned RuO_2 nanowires, forming an interconnected network. The nanorods have lengths ranging from 80 to 180 nm, with diameters of 12 to 45 nm. The SAED image (Figure 8c) confirms the polycrystalline nature of the IrO_2-RuO_2/C. The HR-TEM images of IrO_2-RuO_2/C are displayed in Figure 8d, suggesting the presence of RuO_2 and IrO_2 on the compound. Based on the observed lattice fringes with spacings of 3.2 Å and 2.6 Å, the crystallographic planes can be assigned to the (110) and (101) facets of either RuO_2 or IrO_2, respectively. Attributed to the abundant phase interfaces observed by HR-TEM, which provide active sites, the IrO_2-RuO_2/C hybrid demonstrates exceptional OER performance in acid. It achieves 10 mA cm^{-2} at a low overpotential of 188 mV, significantly outperforming commercial RuO_2 (330 mV) and IrO_2 (360 mV) (Figure 8e). Its superior kinetics are confirmed by a Tafel slope of 42 mV dec^{-1}, which is lower than those of the commercial benchmarks (Figure 8f) and indicates a favorable reaction pathway involving a reversible second-electron transfer. This enhanced activity is coupled with excellent operational stability, as evidenced by a mere 73 mV potential shift during chronopotentiometry testing, far exceeding the stability of the commercial catalysts within 3 hours (Figure 8g). The OER activity and impedance study of IrO_2-RuO_2/C and the physical mixture are shown in Figure 8h,i, indicating very low charge transfer resistance and high OER catalytic performance of IrO_2-RuO_2/C over the physical mixture, RuO_2 NSs/C, and IrO_2 NSs/C.

The enhanced activity stems from the strong synergistic interaction between RuO_2, IrO_2, and N@C, which optimizes reaction kinetics and structural stability, leading to superior performance and extended catalyst lifetime. The enhanced catalytic activity of IrO_2-RuO_2/C can be linked to its greater surface oxophilicity. This is evidenced by CO-stripping voltammetry (Figure 8j), which shows a markedly lower CO oxidation onset potential for IrO_2-RuO_2/C than for the commercial RuO_2 or IrO_2 counterparts. A series of RuO_2/MoO_3 catalysts with abundant and intimate interfaces between RuO_2 and MoO_3 were prepared by the simple electrospinning-subsequent calcination method, which also showed excellent OER activity and durability in an acidic environment[96]. The as-synthesized RuO_2/MoO_3 electrocatalyst exhibits a typical nanowire structure, as clearly shown in the TEM images provided in Figure 8k,l. HR-TEM image (Figure 8m) suggests the mixed biphasic structure of RuO_2/MoO_3. The observed lattice fringes with spacings of 0.258 nm and 0.320 nm match the (101) and (110) planes of RuO_2, and the 0.328 nm spacing aligns with the (021) plane of MoO_3. The RuO_2/MoO_3 nanowire electrocatalyst exhibits superior activity, achieving 10 mA cm^{-2} at a low overpotential of 167 mV (Figure 8n). This value is 41 mV and 48 mV lower than those required by RuO_2 nanowires (208 mV) and c-RuO_2 (215 mV). The Tafel slopes for RuO_2/MoO_3, RuO_2, and c-RuO_2 are 65, 76, and 92 mV dec^{-1}, respectively (Figure 8o). The lowest value for RuO_2/MoO_3 corresponds to the most favorable reaction kinetics. The RuO_2/MoO_3 electrocatalysts delivered an impressively negligible decay of OER performance after 300 h of continuous operation at 10 mA cm^{-2} in 0.5 M H_2SO_4 (Figure 8p). The stability tests revealed distinct degradation patterns: a 120 mV overpotential rise for RuO_2 nanowires over 150 h, and a rapid activity loss for c-RuO_2 within merely 3 h, respectively. DFT calculations reveal that the highest energy barrier of RuO_2/MoO_3 is lower than that of pristine RuO_2. The highest

energy barrier of RuO_2/MoO_3 leads to a theoretical overpotential of 370 mV (Figure 8q), whereas a higher overpotential of 870 mV is required to stimulate the LOM pathway for RuO_2 (Figure 8r). Theoretical calculations indicate that the *O intermediate exhibits a longer bond length on MoO_3 (1.474 Å) than on RuO_2 (1.316 Å). Operando FTIR spectroscopy provided direct experimental evidence for this oxygen spillover mechanism: at 1.6 V *vs.* RHE, a distinct absorption band corresponding to *OO intermediates was detected on MoO_3 sites but not on pristine RuO_2, confirming the preferential migration of *O species from RuO_2 to adjacent MoO_3 and their subsequent coupling with lattice oxygen. This elongation aligns with the observed redshift in the infrared spectrum (Figure 8s,t), confirming the preferential formation of *OO on MoO_3. Consequently, *O species generated on RuO_2 can spill over to adjacent MoO_3 sites, where they combine with lattice oxygen to form O_2. This oxygen spillover process, thermodynamically favorable due to the involvement of MoO_3 lattice oxygen, plays a dual role: it inhibits the formation of oxygen vacancies on RuO_2 and suppresses Ru over-oxidation and dissolution. These combined effects ultimately enhance both the activity and stability of the catalyst for the acidic OER.

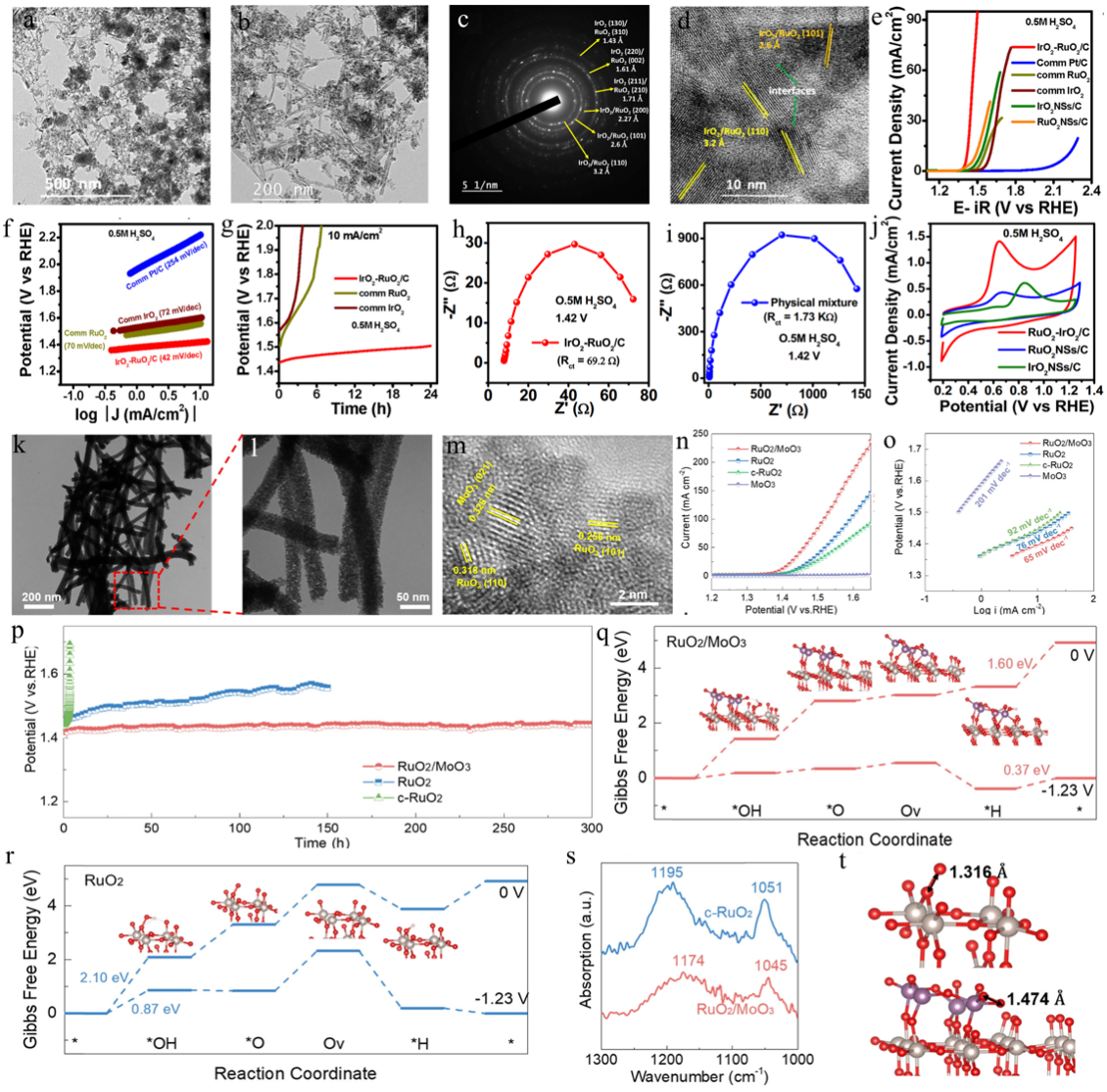


Figure 8. (a, b) TEM images; (c) SAED image; (d) HR-TEM image of IrO_2-RuO_2/C; (e) iR-corrected OER polarization curves of IrO_2-RuO_2/C, commercial RuO_2, commercial IrO_2, commercial Pt/C, RuO_2 NSs/C, and IrO_2 NSs/C in 0.5 M H_2SO_4; (f) Tafel plots; (j) Comparison of the chronopotentiometry curves of IrO_2-RuO_2/C, commercial RuO_2, and commercial IrO_2 in 0.5 M H_2SO_4; (h, i) Nyquist plot of IrO_2-RuO_2/C and physical mixture, respectively; (j) CO stripping experiments of IrO_2-RuO_2/C, comm RuO_2, and comm IrO_2 in 0.5 M H_2SO_4. Reproduced with permission from reference[129]. Copyright © 2022 American Chemical Society; (k) Low; (l) high magnification TEM images of RuO_2/MoO_3; (m) HR-TEM image of RuO_2/MoO_3; (n) LSV curves of RuO_2/MoO_3, RuO_2, c-RuO_2, and MoO_3; (o) Tafel slopes of RuO_2/MoO_3, RuO_2, c-RuO_2, and MoO_3; (p) Chronopotentiometry tests of RuO_2/MoO_3, RuO_2, and c-RuO_2; (q) The calculated energy barrier diagram of RuO_2/MoO_3; (r) The calculated energy barrier diagram of RuO_2; (s) O-O intermediate coupling distance in RuO_2 and RuO_2/MoO_3; (t) *OO intermediates recorded by operando FTIR spectra at a potential of 1.6 V *vs.* RHE for RuO_2 and RuO_2/MoO_3. Reproduced with permission from reference[96]. Copyright © 2024 Royal Society of Chemistry. TEM: transmission electron microscopy; SAED: selective area electron diffraction; HR: high-resolution; OER: oxygen evolution reaction; LSV: linear sweep voltammetry; FTIR: Fourier transform infrared spectroscopy; RHE: reversible hydrogen electrode.

Constructing heterostructures by integrating secondary components with 1D RuO_2 enhances acidic OER performance through synergistic interfacial effects. Notably, the oxygen spillover mechanism enables reactive *O intermediates to migrate from RuO_2 to adjacent phases, thereby preventing lattice oxygen participation and suppressing Ru dissolution.

Having established the efficacy of heterostructure engineering in 1D RuO_2 systems, we now turn to two-dimensional architectures, where the large lateral dimensions and atomic thickness of nanosheets offer distinct advantages for interfacial charge transfer and active site accessibility.

4.3.2 Effect of 2D RuO_2-based catalysts

In the OER process, the difference between LOM and AEM lies in the formation of -O-O after the deprotonation of *OH to *O, and the corresponding V_O-O-O (LOM) or *OOH (AEM), which is usually the step that determines the rate. Both the electronic structure and the local coordination of the Ru-O active site exert a critical influence on the OER mechanism, dictating the favored reaction pathway from a thermodynamic perspective and defining the kinetic bottleneck (rate-determining step)[130]. In this respect, by synthesizing heterojunction catalysts to optimize the performance of Ru active sites, where electron transfer and spatial confinement are used to enhance the activity and stability of RuO_2-based catalysts. Inspired by those findings, Zhang *et al.* reported the solid-phase pyrolysis synthesis of low-Ru-content $RuO_2/CoMnO_3$ nanosheet catalysts (CMR), which demonstrate high OER mass activity, as depicted in Figure 9a[92]. The morphological and structural characteristics of CMR-2 were systematically investigated through advanced microscopy techniques. As evidenced by the SEM image (Figure 9b), the material exhibits a hierarchical architecture composed of numerous nanosheets, which are further constructed from densely packed nanometer-sized nanoparticles. Complementary EDS elemental mapping (Figure 9c) confirms the homogeneous spatial distribution of Ru, Co, and Mn species throughout the nanostructure, indicating successful compositional integration. HR-TEM analysis (Figure 9d) reveals distinctive crystallographic features with two types of lattice fringes exhibiting interplanar spacings of 0.27 nm and 0.32 nm. These measurements correspond precisely to the (104) crystallographic plane of $CoMnO_3$ (PDF #65-3696) and the (110) plane of RuO_2 (PDF #43-1027), respectively. This interfacial coexistence strongly suggests the formation of heterojunctions between RuO_2 and $CoMnO_3$ phases. Such heterostructure engineering is particularly advantageous for enhancing acidic OER performance, as it potentially facilitates optimized charge transfer kinetics and improved structural durability during electrocatalytic operation. The synergistic interplay between these crystalline phases, coupled with the nanoscale architectural design, likely contributes to the observed enhancement in both catalytic activity and long-term stability under harsh acidic conditions. The acidic OER performance of the CMR catalyst series was comprehensively assessed via comparative electrochemical analysis. As illustrated in Figure 9e, CMR-2 demonstrates superior current density profiles within the potential range of 1.40-1.59 V versus RHE compared to both CMR-1 and CMR-3. Quantitative analysis reveals that CMR-2 achieves a significantly lower overpotential of □210 mV at 10 mA cm^{-2}, outperforming CMR-1 (~ 250 mV) and CMR-3 (~ 284 mV). Notably, despite sharing similar synthetic protocols with CMR-2, commercial RuO_2 exhibits substantially higher overpotential (294 mV) under identical testing conditions, highlighting the unique catalytic advantages of the CMR-2 formulation. Kinetic investigation through Tafel analysis (Figure 9f) further corroborates the enhanced OER activity of CMR-2, displaying sequentially lower Tafel slopes of 65.9, 71.6, 73.8, and 91.8 mV dec^{-1} for CMR-1, CMR-2, CMR-3, and RuO_2, respectively. The exceptional kinetic profile of CMR-2 is attributed to optimized electronic structure modifications arising from well-engineered $RuO_2/CoMnO_3$ heterointerface interactions, which facilitate improved charge transfer efficiency. Long-term stability assessment via chronopotentiometry (Figure 9g) demonstrates CMR-2's remarkable operational durability, maintaining a stable potential of ~ 1.5 V for 500 hours at 10 mA cm^{-2}. The observed potential increments remain relatively moderate, with a gradual increase of ~ 40 mV after 200 h (equivalent to 200 μV h^{-1}) and ~ 140 mV after 500 h (280 μV h^{-1}), suggesting progressive but manageable catalyst degradation under prolonged acidic OER conditions. This comprehensive performance evaluation positions CMR-2 as a promising candidate for acid-stable OER electrocatalysis. To elucidate the reaction mechanism with enhanced clarity, online DEMS coupled with isotope labeling was employed. Figure 9h quantifies the relative contents of oxygen isotopologues ($^{32}O_2$, $^{34}O_2$, and $^{36}O_2$), revealing notably low $^{34}O_2$ levels that signify limited lattice oxygen involvement. This observation strongly supports the dominance of the AEM over the lattice oxygen-mediated mechanism in the CMR-2 catalyst. The mechanistic preference for AEM, as schematically illustrated in Figure 9i, accounts for the superior structural stability of CMR-2 compared to conventional RuO_2 catalysts. Complementary DFT calculations elucidate the underlying mechanism for the enhanced OER activity at the $RuO_2/CoMnO_3$ heterointerface, providing atomic-level insights into the optimized interfacial charge transfer dynamics. Notably, the d-band center of CMR-2 resides at -2.55 eV relative to the Fermi level (Figure 9j,k), significantly lower than RuO_2 (-1.65 eV). This electronic structure modification weakens the adsorption energy of reaction intermediates on the catalyst surface. Furthermore, the O p-band center analysis reveals a downward shift to -3.08 eV for CMR-2 versus -2.70 eV for RuO_2, rationalizing the restricted lattice oxygen activation during acidic OER processes. Free energy diagrams (Figure 9l) demonstrate distinct mechanistic pathways: RuO_2 exhibits a 1.96 eV energy barrier for *OOH formation as the RDS, while CMR-2 shows a reduced RDS barrier of 1.67 eV associated with *OOH deprotonation. Theoretical overpotential calculations corroborate these findings, yielding 0.44 V for CMR-2 versus 0.73 V for RuO_2. These computational results collectively highlight the critical role of the $RuO_2/CoMnO_3$ heterointerface in facilitating electron transfer through Co-O-Ru/Mn-O-Ru bridges, thereby optimizing both OER activity and operational stability under acidic conditions.

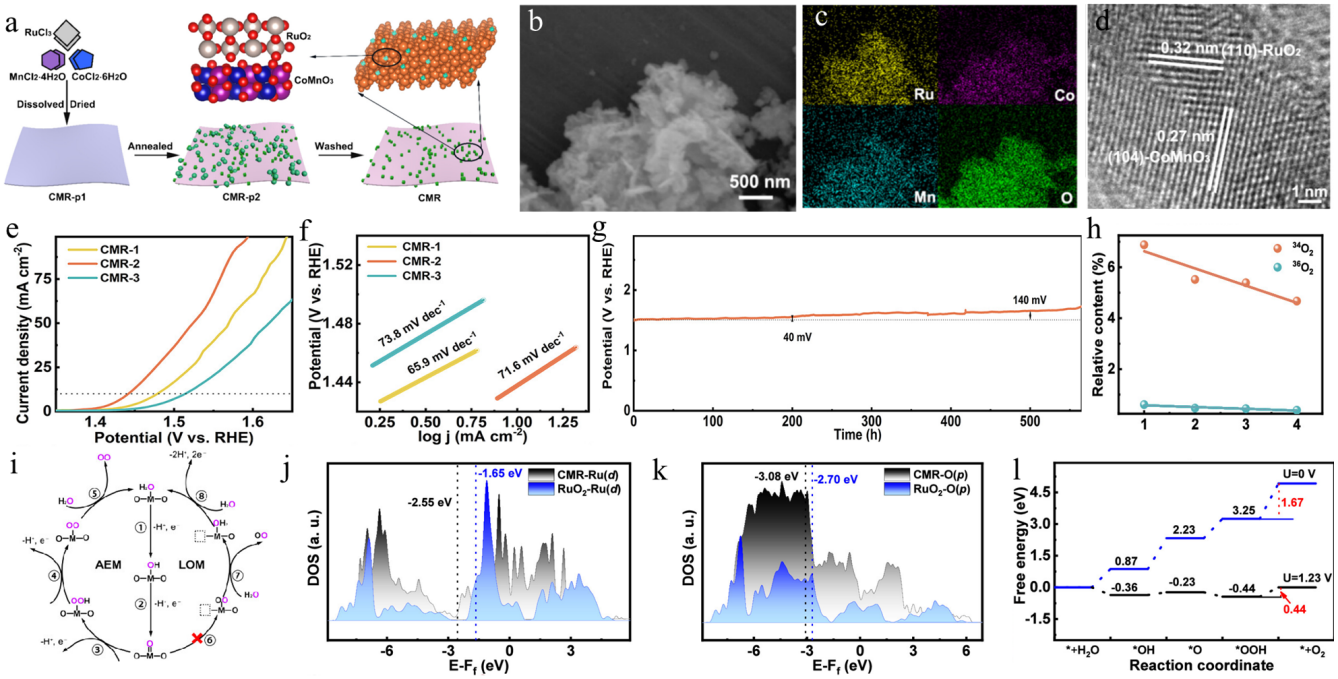


Figure 9. (a) Schematic Diagram for Synthesizing CMR by the Solid-Phase Pyrolysis Method; (b, c) SEM and corresponding elemental mapping images of Ru, Co, Mn, and O; (d) HR-TEM image of CMR-2; (e) LSV curves; (f) Tafel slopes; (g) Chronopotentiometry curves; (h) the contents of $^{34}O_2$, and $^{36}O_2$ in the products during four CV runs; (i) schematic diagram for the OER mechanisms; (j) DOS curves of Ru(d) for CMR and RuO_2; (k) DOS curves of O(p) for CMR and RuO_2; (l) Free energy step diagrams of the OER on CMR. Reproduced with permission from reference[92]. Copyright © 2024 American Chemical Society. Ru: ruthenium; CMR: RuO_2/$CoMnO_3$ nanosheet catalysts; SEM: scanning electron microscope; HR: high-resolution; TEM: transmission electron microscopy; OER: oxygen evolution reaction; DOS: density of states.

The integration of coupling and synergistic strategies endows 2D RuO_2-based electrocatalysts with increased active site density, enhanced electrical conductivity, and optimized adsorption capacity. The research findings highlight that the strategic implementation of coupling effects and synergistic interactions plays a pivotal role in enhancing the electrocatalytic performance of 2D RuO_2-based materials. Through the coupling effect, the structural integration of RuO_2 nanosheets with conductive substrates or functional additives enables efficient electron transport pathways, significantly improving electrical conductivity while suppressing charge accumulation. Concurrently, the synergistic effect facilitates optimized atomic coordination and surface electronic states, which collectively increase the density of catalytically active sites exposed on the material surface. Furthermore, these coordinated strategies synergistically modulate the adsorption/desorption behavior of reactive intermediates (e.g., OER intermediates in water splitting) through electron redistribution at interfacial regions, thereby achieving optimized binding energy for reaction species. Such multi-dimensional optimization not only promotes faster reaction kinetics but also ensures structural durability during prolonged operation. The combined advantages position these engineered 2D RuO_2 electrocatalysts as promising candidates for advanced energy conversion technologies, particularly in oxygen evolution reaction systems.

4.3.3 Effect of 3D RuO_2-based catalysts

Notably, heterostructures alter the original d-band configuration of the active centers, thereby augmenting catalytic activity and stability. These abundant heterostructures within the catalysts expose more edges with increased catalytic activity, providing additional active sites that promote the OER[131]. The construction of heterostructures has been widely studied in 3D Ru-based catalysts[132-134]. For example, to harness the stability and activity enhancement offered by CeO_2, RuO_2-CeO_2 nanoparticle heterostructures were grown on carbon cloth (RuO_2-CeO_2-CC) via an electrodeposition-calcination method by Song *et al.*, with the synthesis route illustrated in Figure 10a[135]. The structural and morphological characteristics of the RuO_2-CeO_2-CC electrocatalyst were systematically investigated through advanced microscopy techniques. SEM analysis (Figure 10b) verified the robust anchoring of RuO_2 and CeO_2 nanoparticles onto the carbon cloth substrate, providing a structural basis for the exceptional operational stability observed during OER evaluations. Further nanoscale characterization via TEM and HR-TEM revealed intimate interfacial contact between RuO_2 and CeO_2 nanoparticles, forming abundant heterostructures (Figure 10c). Analysis of the lattice fringes indicates spacings of 0.311 nm and 0.320 nm, which can be assigned to the CeO_2 (111) and RuO_2 (110) planes, respectively. Complementary HAADF-STEM imaging (Figure 10d) revealed interconnected lattice fringes with periodicities of 0.269 nm and 0.320 nm, which are attributed to the (200) plane of CeO_2 and a distorted (110) plane of RuO_2, respectively. These crystallographic features collectively demonstrate the formation of coherent heterointerfaces between the metal oxide components, which are critical for enhanced charge transfer and structural integrity during electrocatalytic processes. The RuO_2-CeO_2-CC composite electrocatalyst demonstrated

superior OER performance, achieving current densities of 10, 50, and 100 cm_{geo}^{-2} at remarkably low overpotentials of 180, 220, and 242 mV, respectively. This performance significantly surpassed that of its monometallic counterparts (Figure 10e): CeO_2-CC required an excessively high overpotential of 658 mV to reach 10 mA cm_{geo}^{-2}, while RuO_2-CC exhibited a comparatively lower but still substantial overpotential of 275 mV at the same current density. Kinetic analysis revealed a favorable Tafel slope of 58.9 mV dec^{-1} for RuO_2-CeO_2-CC, indicative of enhanced reaction kinetics relative to CeO_2-CC (350.1 mV dec^{-1}) and RuO_2-CC (64.4 mV dec^{-1}). These metrics collectively highlight the synergistic effects arising from the Ru-O-Ce oxygen-bridged architecture, which effectively reduces the activation energy barrier for OER intermediates. Long-term stability testing further distinguished RuO_2-CeO_2-CC, maintaining stable OER activity for 1,000 hours at 10 mA cm_{geo}^{-2} with a minimal applied potential of 1.41 V *vs* RHE (Figure 10f). In stark contrast, RuO_2-CC exhibited rapid performance degradation under identical conditions. The exceptional durability of the composite catalyst underscores the critical role of Ru-O-Ce heterointerfaces in mitigating Ru dissolution through two complementary mechanisms: interfacial charge redistribution and lattice strain modulation within the RuO_2 structure. This dual stabilization strategy establishes RuO_2-CeO_2-CC as a promising candidate for durable AWE systems. The OER mechanisms of RuO_2 and RuO_2-CeO_2 catalysts were systematically investigated through reaction profiles derived from their respective elementary steps (Figure 10g). For pristine RuO_2, the OER proceeds predominantly via the AEM, involving a four-step proton-coupled electron transfer sequence: $H_2O \rightarrow {}^*OH \rightarrow {}^*O \rightarrow {}^*OOH \rightarrow O_2$. In this pathway, the RDS corresponds to *OOH formation, presenting a substantial free energy barrier of 2.10 eV. Notably, the introduction of CeO_2 to form RuO_2-CeO_2 heterostructures induces distinct mechanistic modifications. This hybrid catalyst enables concurrent OER operation through both AEM and oxide path mechanisms, with spatial segregation of active sites: non-interface Ru sites mediate the conventional AEM pathway, while interfacial Ru sites activate a dual-site OPM pathway. The interfacial charge redistribution and modulated *OH adsorption characteristics at Ru interface sites facilitate the emergence of the OPM route. Within this mechanism, the formation of the $^*OH$ and $^*O$ intermediate emerges as the RDS, exhibiting a significantly reduced free energy barrier of 1.88 eV compared to pristine RuO_2. This energetic optimization lowers the theoretical overpotential to 0.65 eV, representing a 24% reduction relative to the pure RuO_2 system. The synergistic interplay between RuO_2 and CeO_2 at their heterointerface thus establishes enhanced charge transfer capabilities and optimized intermediate stabilization, collectively contributing to the superior OER performance observed in the RuO_2-CeO_2 hybrid catalyst. Liu and colleagues developed an acid-treated RuO_2/Co_3O_4 electrocatalyst characterized by low Ru content and a well-defined heterointerface. This design enables simultaneous enhancement of both stability and activity, overcoming their typical trade-off (Figure 10h)[136].

X-ray diffraction analysis (Figure 10i) confirms the coexistence of spinel Co_3O_4 and rutile RuO_2 phases in the composite, with the characteristic RuO_2 diffraction peaks (marked by asterisks) clearly identifiable. TEM analysis further elucidated the structural characteristics of the catalyst. As evidenced by the TEM images presented in Figure 10j, the catalyst exhibits an irregular particulate morphology. A magnified view in Figure 10k reveals the *in-situ* growth of numerous RuO_2 nanoparticles on the Co_3O_4 support matrix. HR-TEM examination, as shown in Figure 10l, identifies distinct lattice fringes corresponding to both components of the composite material. Specifically, the spinel-structured Co_3O_4 support demonstrates characteristic (311) and (422) crystallographic planes, while the deposited RuO_2 particles display (101) and (110) lattice planes consistent with the rutile-phase structure. This interfacial crystallographic evidence conclusively confirms the successful heterostructure integration of RuO_2 nanoparticles with the Co_3O_4 substrate through the synthesis process. The linear-sweep voltammetry LSV polarization profiles presented in Figure 10m demonstrate that the acid-treated RuO_2/Co_3O_4 composite exhibits a substantially reduced OER overpotential of 152 mV, markedly lower than those of commercial RuO_2 (221 mV) and pristine Co_3O_4 (463 mV). This hybrid catalyst further displays robust electrochemical activity, achieving an overpotential of 165 mV at a current density of 10 mA cm^{-2}. To assess operational stability, chronopotentiometry evaluations were conducted in 0.5 M H_2SO_4 electrolyte, revealing exceptional durability of the acid-treated RuO_2/Co_3O_4 system. The catalyst maintained stable performance for over 150 h with a minimal potential increase rate of 0.67 mV h^{-1}, as illustrated in Figure 10n. These findings collectively establish that acid-treated RuO_2/Co_3O_4 combines superior catalytic activity with exceptional acid tolerance, addressing two critical requirements for practical electrocatalytic applications in acidic environments. The acid-treated RuO_2/Co_3O_4 heterostructure demonstrates enhanced acidic OER performance through synergistic electronic and structural modifications. Oxygen vacancies generated during acid treatment induce a partial charge imbalance via electron transfer from Ru octahedral sites (R_{oust}) to Co octahedral sites (Co_{oct}), establishing a robust electron coupling effect at the heterointerface (Figure 10o). Post-operando analysis of Co oxidation states reveals dynamic electron redistribution during OER, where electron-deficient Ru_{oct}-O-Co_{oct} (III) units facilitate electron transfer from adjacent Co^{2+} sites through oxygen-bridged pathways. This interfacial charge compensation mechanism effectively suppresses over-oxidation of active Ru species to soluble RuO_4, thereby preserving catalytic durability in acidic media. Mechanistic studies indicate the system follows an AEM involving four concerted proton-electron transfer steps at the catalyst surface: $H_2O \rightarrow {}^*OH \rightarrow {}^*O \rightarrow {}^*OOH \rightarrow {}^*O_2$ (Figure 10p). Structural defects including oxygen vacancies and heterogeneous interfaces synergistically optimize intermediate adsorption energetics, particularly lowering the energy barrier for *OOH formation. Crucially, the strong interfacial electron coupling preferentially stabilizes Ru active sites against oxidative deactivation through electronic modulation, while maintaining favorable adsorption characteristics for OER intermediates. This dual functionality of electronic protection and enhanced active site accessibility underpins the material's exceptional acidic OER stability, establishing a design paradigm for durable electrocatalysts in proton-exchange membrane systems.

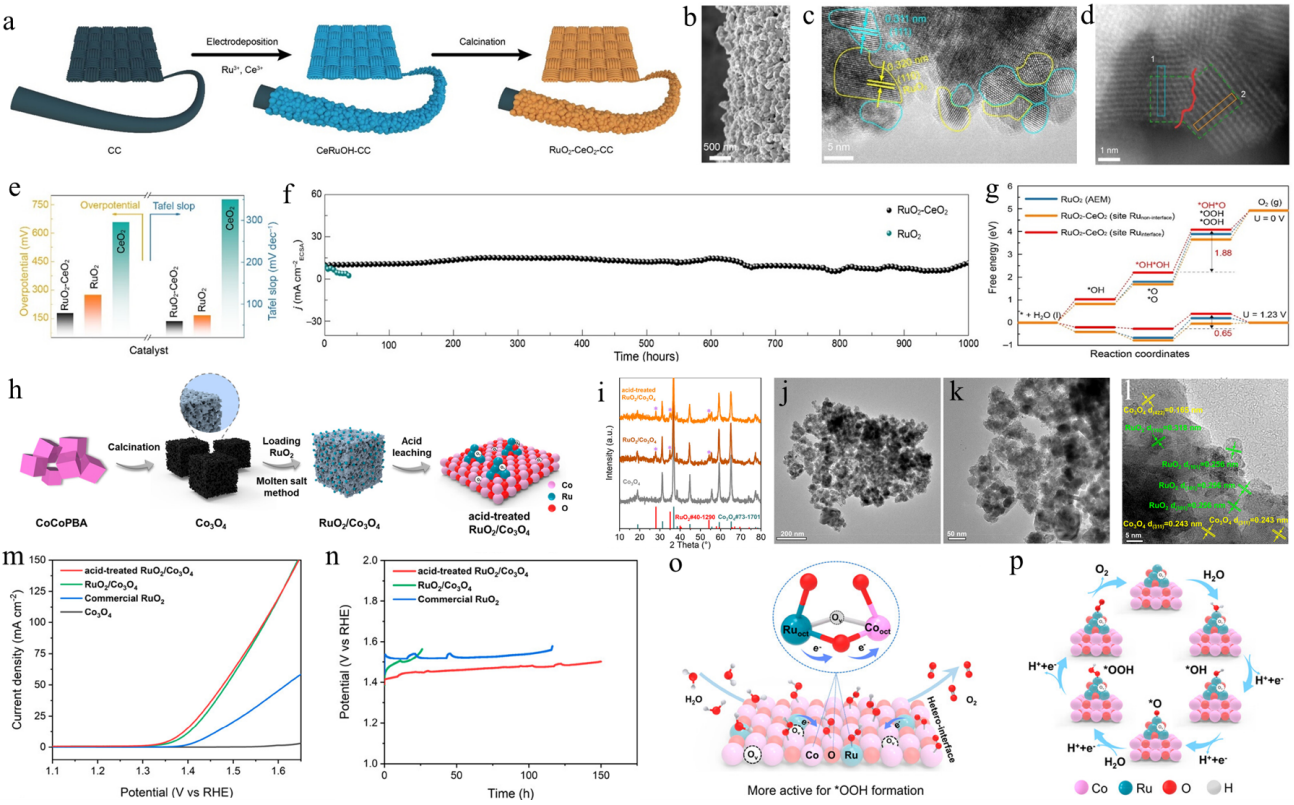


Figure 10. (a) Schematic illustration of the synthesis of the RuO_2-CeO_2-CC catalyst; (b, c) SEM images; (d) TEM image; (e) Histograms of overpotentials at 10 mA cm_{geo}^{-2} and Tafel slopes for various catalysts; (f) Time-dependent current density curves for RuO_2-CeO_2-CC and RuO_2-CC at 1.41 V versus RHE and commercial RuO_2-CC at 1.51 V versus RHE; (g) Free energy diagrams for the preferred OER paths on the surfaces of RuO_2 and RuO_2-CeO_2. Reproduced with permission from reference[135]. Copyright © 2024 American Chemical Society; (h) Schematic illustration of the synthesis of acid-treated RuO_2/Co_3O_4; (i) XRD spectra of acid-treated RuO_2/Co_3O_4, RuO_2/Co_3O_4, and Co_3O_4 (PDF 73-1701 and 40-1290 for Co_3O_4 and RuO_2, respectively). Asterisks correspond to the peaks of RuO_2; (j, k) TEM images of acid-treated RuO_2/Co_3O_4 at different scales; (l) HR-TEM image of acid-treated RuO_2/Co_3O_4 with crystal planes of Co_3O_4 (yellow) and RuO_2 (green); (m) Geometric LSV polarization curves of acid-treated RuO_2/Co_3O_4, RuO_2/Co_3O_4, commercial RuO_2, and Co_3O_4; (n) Chronopotentiometry curves of acid-treated RuO_2/Co_3O_4, RuO_2/Co_3O_4, and commercial RuO_2; (o) Schematic illustration of heterointerface electron migration in acid-treated RuO_2/Co_3O_4; (p) OER pathway in an acidic electrolyte for acid-treated RuO_2/Co_3O_4. Reproduced with permission from reference[136]. Copyright © 2024 American Chemical Society. Ru: ruthenium; SEM: scanning electron microscope; TEM: transmission electron microscopy; RHE: reversible hydrogen electrode; OER: oxygen evolution reaction; HR: high-resolution.

In addition to oxide-oxide heterojunctions, metal-oxide heterostructures within 3D hollow architectures have emerged as a promising design paradigm. Wu *et al.* reported a nitrogen-doped carbon coated porous Ru/RuO_2 heterojunctional hollow sphere (Ru/RuO_2/NC) as a bifunctional electrocatalyst for acidic OER and HER[132]. The Ru/RuO_2/NC hollow spheres feature a unique tri-functional architecture: (1) the metallic Ru domains provide high electrical conductivity and serve as HER active sites; (2) the RuO_2 domains serve as OER active sites with optimized intermediate adsorption; and (3) the NC coating protects the internal structure from acidic corrosion while maintaining electron transport pathways. The heterojunction between Ru and RuO_2 creates a built-in electric field that facilitates interfacial charge transfer, optimizing the adsorption/desorption energetics of OER intermediates. The Ru/RuO_2/NC catalyst achieves an overpotential of 211 mV at 10 mA cm^{-2} in 0.5 M H_2SO_4 with a Tafel slope of 39.1 mV dec^{-1}, and maintains exceptional stability over 100 h of continuous operation. This remarkably low degradation rate positions Ru/RuO_2/NC among the most durable Ru-based acidic OER catalysts reported to date, demonstrating the synergistic benefits of combining metal-oxide heterojunctions with 3D hollow architecture and protective carbon coating.

The most significant finding from the heterointerface studies is the emergence of dual-pathway OER catalysis as a distinct advantage of heterostructure design over single-component strategies. In RuO_2-CeO_2-CC, non-interface Ru sites mediate AEM while interfacial Ru sites activate OPM, achieving a 24% reduction in theoretical overpotential compared to pure RuO_2. In RuO_2/MoO_3, the oxygen spillover mechanism enables *O migration from RuO_2 to MoO_3, where lattice oxygen participates in O-O coupling, this represents a controlled LOM that occurs on the secondary phase rather than on RuO_2, thereby protecting the RuO_2 lattice from vacancy-induced degradation. In acid-treated RuO_2/Co_3O_4, interfacial electron coupling suppresses Ru over-oxidation while maintaining favorable *OOH adsorption energetics. These three mechanisms, dual-pathway catalysis, oxygen spillover, and interfacial charge redistribution, represent fundamentally different routes to breaking the activity-stability trade-off, and their relative merits can be critically

assessed: (1) Dual-pathway catalysis offers the best thermodynamic advantage (lowest theoretical overpotential) but requires precise control of interfacial site geometry; (2) Oxygen spillover provides the most robust lattice protection but depends on the thermodynamic favorability of *O migration, which varies with the secondary phase; (3) Interfacial charge redistribution is the most synthetically accessible but provides only moderate stability enhancement. A critical gap across all heterointerface studies is the lack of operando evidence for the proposed dual-pathway mechanism: while DFT calculations support the thermodynamic feasibility, direct experimental verification remains absent. Future studies should prioritize such correlative operando measurements to validate the dual-pathway hypothesis.

4.4 Other modification

4.4.1 Effect of 1D RuO_2-based catalysts

By constructing a unique asymmetric structure, a single unit can possess multi-functional properties, which can expose the active sites on the surface of the 1D RuO_2 electrocatalyst to a greater extent. Named after the two-faced Roman deity, Janus nano-architectures represent a developing category of nanostructures characterized by the integration of distinct components into one asymmetric, "two-faced" system[137]. Chen *et al.* reported, for the first time, a facile process to prepare well-dispersed RuO_2 nanorods on carbon supports (Ru/RuO_2 NB/C)[138]. In this process, carbon substrates promote the partial reduction of RuO_2 to Ru at relatively low temperatures (~ 300 °C) without any other reductants, as shown in Figure 11a. As shown in HAADF-STEM images (Figure 11b,c), the Ru/RuO_2 NB/C catalyst formed under PAP (300) adopts a unique nanosized boomerang shape. These structures, indicated with red circles, consist of a kinked original rod with an additional arm. The material exhibits a Janus structure at the kink, featuring two distinct arms. This is evidenced by lattice fringe measurements (Figure 11d,e): the original arm retains the 0.318 nm spacing of RuO_2 (110), whereas the newly grown arm displays a spacing of 0.233 nm, characteristic of the Ru (100) facet. The OER activities in acidic media, quantified by the η_{10} overpotential, rank as follows (Figure 11f): Ru/RuO_2 NB/C (276-330 mV) > c-RuO_2/C (343-428 mV) > other tested electrocatalysts. This confirms the superior activity of RuO_2-based materials, with the Janus nanostructure showing the lowest overpotential range. The Tafel slopes measured in acidic solution are 69.0 and 120 mV dec^{-1} for Ru/RuO_2 NB/C and c-RuO_2/C, respectively (Figure 11g). The significantly lower value for Ru/RuO_2 NB/C is consistent with its more favorable reaction kinetics. The excellent charge-transfer capability of Ru/RuO_2 NB/C is evidenced by EIS. As shown in Figure 11h, it exhibits the lowest R_{ct}, signifying faster interfacial electron transfer and thus more favorable OER kinetics. The Ru/RuO_2 NB/C catalyst demonstrates exceptional operational stability, a key parameter for practical OER applications, maintaining 92% activity over 20 hours (Figure 11i). Post-electrolysis HR-TEM characterization (Figure 11j) confirms that the Janus Ru/ RuO_2 nano-boomerang morphology and crystalline structure are well preserved after 20 h of OER operation at overpotentials of 80 and 300 mV, providing direct structural evidence for the robustness of this asymmetric architecture under acidic OER conditions. This performance originates from its innovative Janus architecture, comprising distinct Ru and RuO_2 arms, which inspired a novel design paradigm. Consequently, the developed method offers a versatile and scalable route to fabricate acidic electrocatalysts with integrated high activity, durability, and thermal stability for overall water splitting.

1D RuO_2-based nanomaterials have garnered significant attention in the field of electrocatalysis due to their exceptional catalytic performance, structural stability, and tailored surface properties. In recent studies, RuO_2 nanorods and their derivatives, particularly those with 1D nanostructures, have demonstrated remarkable potential as electrocatalysts for the oxygen evolution reaction in acidic conditions. These materials combine high surface area, ultraviolet-visible absorption capabilities, and active sites that facilitate charge transfer and water oxidation processes, making them highly suitable for water splitting applications. The unique Janus nanostructure, where two distinct phases (Ru and RuO_2) coexist on the same nanoscale, further enhances the catalytic activity of RuO_2-based materials. This structure provides a synergistic effect, with Ru offering increased conductivity and RuO_2 providing active sites for OER, thus improving the overall kinetics and efficiency of the reaction. Additionally, the structural stability of 1D nanomaterials under dynamic working conditions is crucial for long-term applications, as it ensures sustained performance and durability. The scalable synthesis methods developed for these 1D RuO_2-based catalysts have also been a significant advancement, addressing the practical challenges of large-scale production. These methods pave the way for the integration of RuO_2-based nanomaterials into real-world energy systems, such as hydrogen fuel production and renewable energy storage. Overall, the study of 1D RuO_2-based electrocatalysts has not only deepened our understanding of their catalytic mechanisms but also provided a foundation for the development of more efficient and stable materials for sustainable energy applications.

4.4.2 Effect of 2D RuO_2-based catalysts

Complementing other performance-enhancement strategies, phase engineering is increasingly recognized for optimizing Ru-based catalysts. Its appeal lies in the concurrent engineering of high-density active sites and robust chemical stability, crucial for acidic OER[139]. The amorphous regions confer structural adaptability to Ru-based catalysts, leading to greater tolerance to strain and deformation. This ultimately reduces the dissolution rate of Ru active sites, resulting in stability superior to that of their crystalline counterparts[140]. In view of this, Zeng *et al.* proposed an order-disorder structure optimization strategy. This approach utilized RuO_2 nanosheets with well-defined amorphous-crystalline heterointerfaces supported on carbon cloth (a/c-RuO_2/CC) to achieve efficient water oxidation, particularly under acidic conditions[141]. The preparation of a/c-RuO_2/CC involves first growing aligned Co-MOF

nanosheets on carbon cloth. This is done by reacting Co^{2+} with 2-methylimidazole in water at room temperature to form Co-MOF/CC, as illustrated in Figure 12a. SEM analysis reveals the uniform growth of Co-MOF nanosheet arrays on CC, as distinctly illustrated in Figure 12b. HR-TEM characterization of a/c-RuO_2 nanosheets (Figure 12c) unveils the presence of quasi-transparent nano-holes (demarcated by white dashed circles), which correspond to structural lattice defects. Further magnification in Figure 12d elucidates the spatial distribution of these defects, predominantly localized within amorphous domains, while adjacent crystalline regions exhibit well-defined lattice fringes with a measured interplanar spacing of 0.25 nm, consistent with the (101) crystallographic plane of RuO_2. The coexistence of amorphous and crystalline phases in the a/c-RuO_2/CC architecture is conclusively verified by SAED analysis (inset, Figure 12c), which displays characteristic diffuse halo patterns indicative of amorphous material alongside discrete diffraction spots corresponding to crystalline domains, thereby confirming the formation of distinct amorphous-crystalline interfacial boundaries. LSV analysis reveals that the a/c-RuO_2/CC composite exhibits remarkably enhanced performance for the acidic oxygen evolution reaction. The structurally ordered-disordered hybrid catalyst achieves an exceptionally low overpotential of 150 mV at 10 mA cm^{-2}, significantly outperforming both crystalline RuO_2/CC (234 mV) and amorphous RuO_2/CC (198 mV), while showing substantial improvement over commercial RuO_2 (390 mV) (Figure 12e). This enhanced activity is further corroborated by Tafel analysis, where a/c-RuO_2/CC exhibits superior reaction kinetics with a Tafel slope of 47 mV dec^{-1}, markedly lower than its crystalline (78 mV dec^{-1}) and amorphous (72 mV dec^{-1}) counterparts (Figure 12f). The improved charge transfer characteristics are quantitatively confirmed through electrochemical impedance spectroscopy, revealing lower R_{ct} in the hybrid structure compared to single-phase materials (Figure 12g). Notably, the structural engineering confers exceptional operational stability, with a/c-RuO_2/CC maintaining stable performance over 24 h of continuous operation, contrasting sharply with the 115 mV potential increase observed in amorphous RuO_2 /CC and the complete failure of crystalline RuO_2/CC within 4 h (Figure 12h). This durability enhancement aligns with recent advances in defect-rich amorphous/crystalline RuO_2 systems, where phase boundary engineering effectively mitigates structural degradation during prolonged OER operation. The performance metrics position this hybrid architecture as a promising candidate for proton exchange membrane electrolysis, particularly when considering both activity metrics and long-term stability requirements. As depicted in Figure 12i, the dissociation energy (E_d) of amorphous-crystalline RuO_2 (a/c-RuO_2) is calculated as 1.21 eV, exhibiting a notable reduction compared to its fully amorphous counterpart (a-RuO_2, 1.30 eV). This downward shift in Ed toward the Fermi level confirms the regulatory effect of amorphous-crystalline boundary engineering on electronic structure. Remarkably, the structural order-disorder configuration in a/c-RuO_2 demonstrates a 0.16 eV E_d reduction relative to crystalline RuO_2 (c-RuO_2, 1.05 eV), suggesting optimized interfacial electronic interactions between catalytic surfaces and reaction intermediates. The PDS analysis in the AEM reaction pathway (Figure 12j,k,l) reveals *OOH species formation as the rate-limiting step for both a-RuO_2 (1.96 eV) and c-RuO_2 (2.23 eV). Significantly, a/c-RuO_2 achieves the most favorable thermodynamic pathway with a substantially lowered energy barrier of 1.77 eV, demonstrating 13.7% and 26.0% reductions compared to amorphous and crystalline phases, respectively. This barrier reduction mechanism can be calculated to arise from synergistic effects between crystalline ordering and amorphous flexibility, where boundary-induced charge redistribution facilitates oxygen intermediate stabilization. The attenuated energy barrier directly correlates with reduced oxygen evolution reaction overpotential, establishing structure-property relationships crucial for advanced electrocatalyst design.

Therefore, the order-disorder structure optimization strategy, implemented by constructing amorphous-crystalline phase boundaries in 2D RuO_2 nanosheets, establishes an effective design pathway. This approach enables the development of RuO_2-based electrocatalysts with high activity and long-term durability for acidic OER, suitable for energy-related applications. The recently proposed order-disorder structure optimization strategy for two-dimensional RuO_2 nanosheets demonstrates remarkable potential in advancing OER catalysis under acidic conditions. This innovative approach strategically manipulates the atomic arrangement to create amorphous-crystalline phase boundaries within the RuO_2 matrix, effectively addressing the longstanding challenges of insufficient activity and poor durability in conventional RuO_2-based catalysts. The optimized heterophane interfaces facilitate enhanced electron transfer kinetics and stabilize active Ru sites against dissolution, while the disordered domains provide abundant defect-rich regions for improved catalytic accessibility. Experimental evidence shows that this structural engineering not only boosts the density of oxygen vacancies but also regulates the adsorption strength of reaction intermediates, synergistically enhancing both OER activity and operational stability. Importantly, the successful implementation of this strategy on 2D nanosheets opens new avenues for developing cost-effective, corrosion-resistant electrocatalysts, particularly promising for PEMWE and other energy conversion devices requiring prolonged operation in harsh acidic environments. These findings establish phase boundary construction as a universal design principle for next-generation RuO_2 materials, bridging fundamental surface science with practical applications in sustainable hydrogen production and beyond.

4.4.3 Effect of 3D RuO_2-based catalysts

The inherent electronic configuration of RuO_2 enables its high OER activity via moderate intermediate binding. However, this same property can lead to instability, as the material tends to form soluble RuO_4 at anode potentials above 1.4 V in acidic media. Modulating the electronic structure to suppress this degradation pathway thus presents an attractive approach to enhance durability without sacrificing activity. Wang *et al.* introduced interstitial carbon into 3D RuO_2 through a combination of selenium evaporation and carbon combustion to simultaneously enhance the OER stability and activity of 3D RuO_2-based catalysts in acidic environments[91]. Compared to commercial RuO_2, the C-RuO_2-RuSe-5 catalyst exhibits markedly enhanced activity for the OER. The

structural characteristics of the C-RuO_2-RuSe-10 composite were systematically investigated through advanced microscopy techniques. As revealed by TEM imaging (Figure 13a), the material preserves its hollow spherical architecture, demonstrating structural integrity during the modification process. HAADF-STEM (Figure 13b) unveiled distinct lattice fringes with measured interplanar spacings of 0.248 nm and 0.308 nm, exhibiting noticeable lattice contraction compared to the standard (101) and (110) planes of pristine RuO_2. This distortion phenomenon is rationalized through crystallographic modeling (Figure 13c), which illustrates the tetragonal P42/mnm structure of RuO_2 viewed along the [111] zone axis. The structural modifications are attributed to interstitial carbon incorporation within the crystal lattice, inducing measurable deformations that align with the observed HAADF-STEM features. Elemental mapping analysis (Figure 13d) confirmed the homogeneous distribution of Ru, Se, C, and O constituents throughout the hollow nanostructures, providing direct evidence for successful heteroatom integration. Notably, the absence of a discrete carbon shell in HR-TEM images suggests that carbon atoms primarily occupy interstitial positions within the RuO_2 matrix rather than forming surface coatings. This atomic-level integration of Se and C dopants into the RuO_2 framework is critical for understanding the material's modified electronic structure and enhanced catalytic properties. XAS was employed to systematically probe how the incorporation of Se and C modulates the atomic coordination environment and electronic structure. A significant increase in Ru-O bond distance is observed for the C-RuO_2-RuSe-10 hybrid compared to pristine RuO_2, as indicated by Ru K-edge EXAFS data (Figure 13e). This structural modification arises from the lattice distortion induced by interstitial carbon atoms forming robust C-O covalent bonds. Complementary insights from the C K-edge XANES spectra (Figure 13f) demonstrate distinctive electronic features: A prominent peak at 286.8 eV corresponds to the π^* antibonding orbital of sp^2-hybridized C=C bonds, while the characteristic σ^* resonance signatures between 293-310 eV confirm C's hybridization state. Notably, a significantly intensified peak (marked by grass-green dotted frame) emerges compared to reference carbon materials (graphene and carbon powder), unambiguously attributed to the formation of C-O bonds by interstitial carbon dopants. The observed binding energy enhancement and positive shift of the C-O signature indicate substantially strengthened covalent interactions between carbon and oxygen within the RuO_2 matrix. Furthermore, the detectable binding energy shift in Ru 3d orbitals provides direct evidence of intensified electronic coupling between interstitial carbon and the RuO_2 framework. These collective findings substantiate that C incorporation not only modifies the local coordination geometry through lattice strain but also establishes strong electronic interactions within the C-RuO_2-RuSe-10 heterostructure, thereby optimizing its electronic configuration for enhanced catalytic functionality. In comparison with commercial RuO_2, which requires overpotentials of 317, 404, and 498 mV to achieve current densities of 10, 50, and 100 mA cm^{-2}, respectively, the C-RuO_2-RuSe-5 catalyst demonstrates superior performance, attaining equivalent current densities at significantly reduced overpotentials of 212, 259, and 294 mV (Figure 13g). To further elucidate the catalytic kinetics for the OER, Tafel analyses derived from polarization curves reveal that the C-RuO_2-RuSe series exhibits markedly lower Tafel slopes than pristine $RuSe_2$, indicative of enhanced OER kinetics following thermal treatment (Figure 13h). Notably, the stability of the C-RuO_2-$RuSe_2$ catalysts under acidic conditions is substantially improved compared to $RuSe_2$, underscoring the efficacy of post-annealing in air for structural stabilization (Figure 13i). Among the variants, C-RuO_2-RuSe-10 exhibits exceptional durability, maintaining catalytic activity without significant decay for approximately 50 h under aggressive acidic media - a performance surpassing that of commercial RuO_2. Remarkably, this stability persists even at elevated current densities of 20 and 50 mA cm^{-2}, highlighting the robustness of C-RuO_2-RuSe-10 for sustained OER operation in harsh electrochemical environments. These findings collectively establish thermal post-treatment as a critical strategy for optimizing both activity and stability in acidic OER electrocatalysts. As shown in Figure 13j, the activation Δ_G values for the PDSs in the AEM reaction pathway are 2.02 eV and 1.78 eV for RuO_2 and C-RuO_2-RuSe-10 catalysts, respectively. This notable reduction in energy barrier (Δ_G = 0.24 eV) upon C interstitial incorporation strongly suggests that the introduced carbon species effectively modulates the electronic structure and reaction pathways, thereby substantially enhancing the OER kinetics. These computational findings align quantitatively with the experimentally observed catalytic performance improvements, providing mechanistic validation for the critical role of interstitial carbon dopants in optimizing surface adsorption energetics during water oxidation processes.

This work proves that the stability and activity of 3D-RuO_2 can be significantly improved through gap C engineering. This opens broad prospects for the design and construction of a new generation of high-performance electrocatalysts, thereby widely expanding the research on future materials in various potential application fields. This study demonstrates that the stability and catalytic activity of 3D-RuO_2 can be remarkably enhanced through innovative gap C engineering, a strategic approach that modulates the material's atomic structure and electronic properties. By precisely incorporating carbon atoms into interstitial sites, the engineered 3D-RuO_2 exhibits superior resistance to structural degradation and optimized charge transfer kinetics, addressing long-standing challenges in electrocatalyst durability and efficiency. This breakthrough not only provides a robust platform for developing next-generation electrocatalysts with exceptional performance metrics but also establishes a novel paradigm for material design in energy conversion and storage technologies.

While the preceding sections have individually described various strategies for enhancing the stability of Ru-based OER catalysts, including heteroatom doping, protective coating, structural confinement, and reaction pathway regulation, a systematic comparison of their effectiveness, limitations, and scalability is essential for identifying the most promising approaches. Based on the above analysis, we identify three tiers of promise for overcoming the fundamental stability limitations of Ru-based OER catalysts:

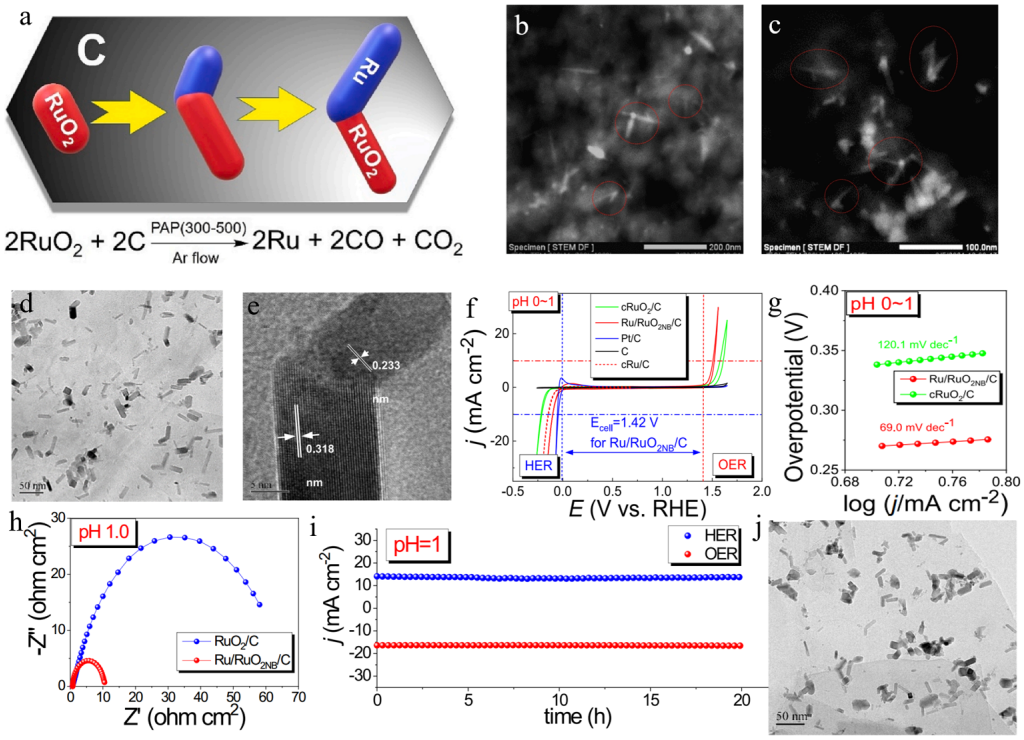


Figure 11. (a) The proposed mechanism for carbon promoting the reduction of RuO_2 to Ru; (b) Low-magnification; (c) high-magnification HAADF-STEM images of Ru/RuO_2 NB/C (Ru/RuO_2 NBs are highlighted by red dashed circles); (d, e) the Ru/RuO_2 NB/GE from corresponding RuO_2 NR/GE treated with PAP (300); (f) CVs of the overall water splitting process for Ru/RuO_2 NB/C, $cRuO_2$/C, cRu/C, and C (XC-72) in Ar-purged and acidic aqueous solutions at a scan rate of 50 mV s^{-1}; (g) Tafel plots for Ru/RuO_2 NB/C *vs.* $cRuO_2$/C in OER and Ru/RuO_2 NB/C *vs.* $cRuO_2$/C and 20% Pt/C in OER; (h) EIS measurements carried out in Ar-purged and acidic aqueous solutions at η_{10} OER = 300 mV for OER; (i) Long-term stability of Ru/RuO_2 NB/C examined by chronoamperometry at overpotentials of 80 and 300 mV for (red solid circle) OER in acidic aqueous solutions; (j) Bright-field HR-TEM images of Ru/RuO_2 NB/GE after electrolysis static overpotentials of 80 and 300 mV for OER, for 20 h in acidic aqueous solutions 0.5 M H_2SO_{4aq}. Reproduced with permission from reference[138]. Copyright © 2023 Elsevier. Ru: ruthenium; TEM: transmission electron microscopy; HAADF-STEM: high-angle annular dark-field scanning TEM; OER: oxygen evolution reaction; EIS: electrochemical impedance spectroscopy; HR: high-resolution.

(1) Co-doping strategies offer the best balance of effectiveness, scalability, and mechanistic rationality. They can break the activity-stability trade-off by decoupling the electronic structure requirements for activity and stability through complementary dopant roles. The synthesis methods are compatible with existing catalyst manufacturing, and the stability improvements have been validated in PEMWE devices at ampere-level current densities[142]. Grain boundary engineering combined with strategic doping is equally promising for near-term deployment, having demonstrated the longest PEMWE durability among Ru-based catalysts[143]. The combination of GB stabilization and dopant segregation at GBs creates a self-reinforcing stability mechanism; (2) Structural confinement provides excellent stability enhancement with maintained activity, but requires further development of scalable support synthesis and catalyst-coated membrane integration processes[144]. Dynamic oxygen vacancy management offers a conceptually elegant solution that allows controlled LOM activity with self-healing, but requires long-term validation under industrial conditions[68]; and (3) OPM-enabling dual-site design represents the ultimate solution, simultaneously achieving scaling-relation-free activity and lattice-preserving stability, but currently requires atomic-level structural control that is not scalable[24]. Future advances in atomically precise synthesis or self-assembly methods could elevate this strategy to higher tiers. High-entropy RuO_2 leverages entropy stabilization for enhanced durability, but the compositional complexity and reproducibility challenges currently limit its scalability and mechanistic understanding[66].

Having discussed the individual research progress of defect engineering, doping modification, and heterointerface construction, it is essential to provide a horizontal comparison of these three core strategies to guide rational catalyst design. Table 3 summarizes the applicable scenarios, performance improvement ranges, and inherent drawbacks of each modification route.

4.5 The other RuO_2-based catalysts

4.5.1 High-entropy oxide engineering

High-entropy oxides (HEOs), originally developed in structural materials science, have recently emerged as a transformative paradigm for designing Ru-based acidic OER electrocatalysts. The high-entropy concept, incorporating five or more cationic elements in equimolar or near-equimolar ratios into a single-phase oxide lattice, introduces four synergistic effects that directly

address the activity-stability trade-off of RuO_2: (1) entropy stabilization, where the configurational entropy thermodynamically stabilizes the single-phase rutile structure against phase segregation and amorphization under anodic potentials; (2) cocktail effects, where the collective interaction of multiple dopants produces emergent catalytic properties unattainable by any single dopant; (3) lattice distortion, where atomic-size mismatch among different cations induces local strain that modulates the Ru-O bond length and electronic structure; and (4) sluggish diffusion, where the complex multi-element environment retards cation migration and dissolution kinetics, enhancing durability.

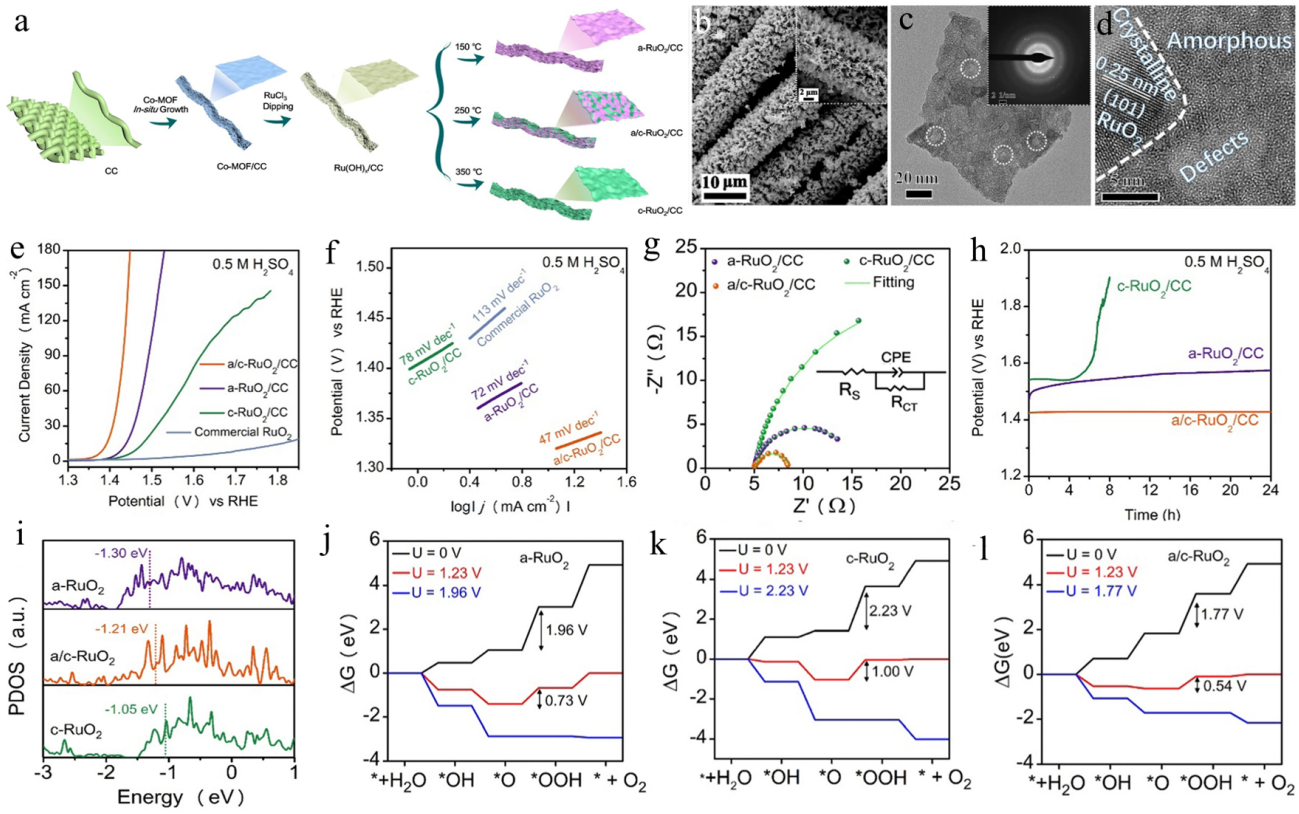


Figure 12. (a) Schematic illustration of the a/c-RuO_2/CC, a-RuO_2/CC, and c-RuO_2/CC preparation; (b) SEM images of a/c-RuO_2/CC; (c, d) HR-TEM images (the inset is the SAED pattern) of a/c-RuO_2/CC; (e) Polarization curves; (f) Tafel slopes of different samples for the acidic OER in 0.5 M H_2SO_4 electrolyte; (g) EIS spectra for the acidic OER of a/c-RuO_2 /CC, a-RuO_2/CC, and c-RuO_2/CC measured at 1.60 V *vs*. RHE in 0.5 M H_2SO_4; (h) Chronopotentiometry measurement of a/c-RuO_2/CC, a-RuO_2/CC, and c-RuO_2/CC recorded at a constant current density of 10 mA cm^{-2}; (i) Projected electronic densities of states for a/c-RuO_2, a-RuO_2, and c-RuO_2; (j, k, l) Calculated free energy diagrams of the OER pathway for the (j) a-RuO_2, (k) c-RuO_2, and (l) a/c-RuO_2. Reproduced with permission from reference[141]. Copyright © 2023 Royal Society of Chemistry. Ru: ruthenium; SEM: scanning electron microscope; CC: carbon cloth; HR: high-resolution; TEM: transmission electron microscopy; SAED: selective area electron diffraction; OER: oxygen evolution reaction; EIS: electrochemical impedance spectroscopy.

The pioneering work by Miao *et al.* demonstrated that co-doping non-precious Cr, W, and Cu elements into the RuIr-mixed oxide lattice constructs a high-entropy rutile $(Ru_{0.2}Ir_{0.2}Cr_{0.2}W_{0.2}Cu_{0.2})O_2$ catalyst with exceptional acidic OER performance[146]. Despite the insulating nature of individual Cr_2O_3, WO_3, and CuO components, the high-entropy rutile phase exhibits metallic conductivity owing to the preservation of the Ru/Ir-derived d-band electronic structure across the multi-element lattice. The catalyst achieves a low overpotential of 228 mV at 10 mA cm^{-2} and remarkable stability exceeding 200 h at 10 mA cm^{-2} in 0.5 M H_2SO_4, significantly outperforming the low-entropy binary and ternary counterparts. DFT calculations reveal that the multi-element synergy optimizes the adsorption free energies of *OH and *OOH intermediates by simultaneously modulating the d-band centers of multiple cation sites, effectively circumventing the scaling relationship that constrains conventional single-dopant systems.

Extending this concept to Ir-free systems, Yu *et al.* reported an Ir-free high-entropy $(RuCrMnFeNi)O_2$ electrocatalyst synthesized via a facile two-step hydrothermal and annealing method, which exhibits an overpotential of 212 mV at 10 mA cm^{-2} and 100 h stability in 0.5 M H_2SO_4[147]. The complete elimination of Ir from the composition represents a significant cost advantage while maintaining competitive performance. The activated lattice oxygen in this Ir-free HEO system participates in the OER through a controlled LOM pathway that is self-limiting due to the entropy-stabilized lattice, preventing the catastrophic structural collapse typically associated with LOM in conventional RuO_2.

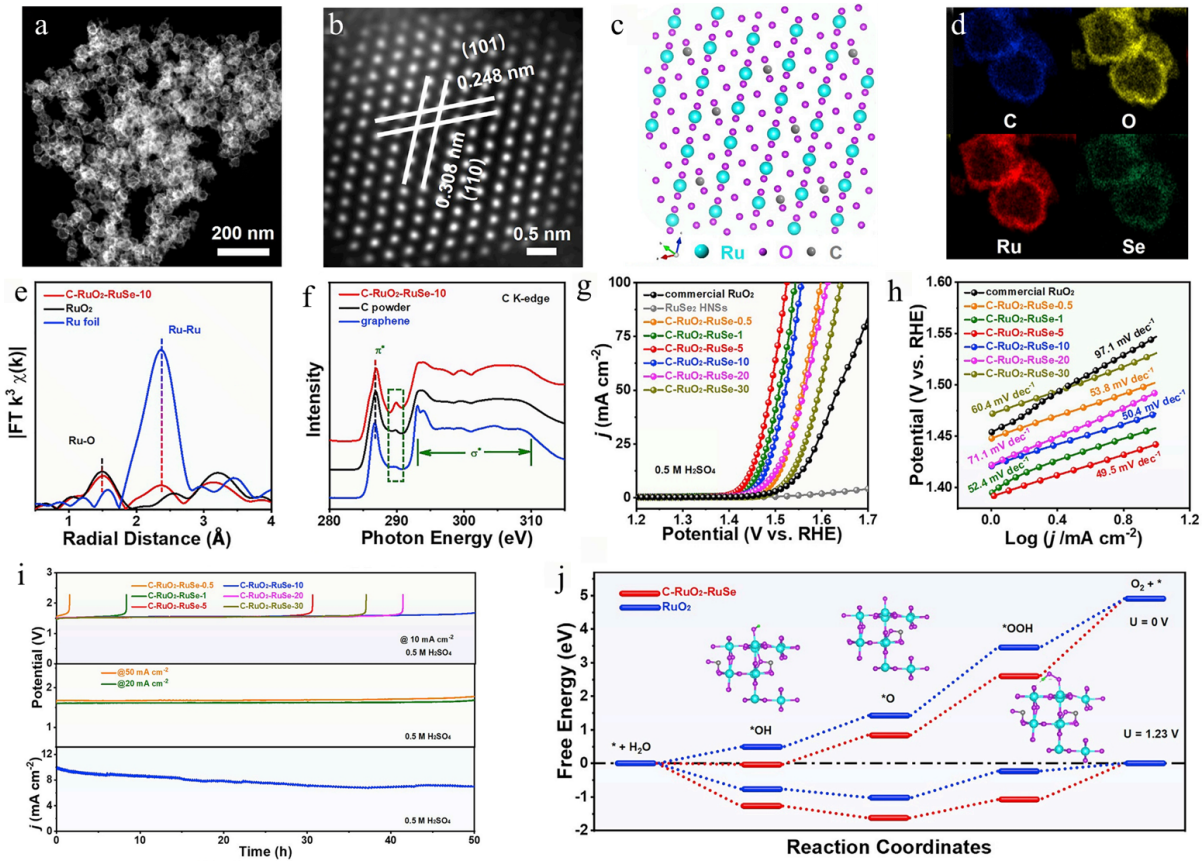


Figure 13. (a) HAADF-STEM image; (b) High-resolution HAADF-STEM image; (c) Crystal structure model; (d) STEM image and STEM-EDS elemental mappings of C-RuO_2-RuSe-10; (e) Ru K-edge EXAFS; (f) C K-edge XANES spectra of C-RuO_2-RuSe-10; (g) OER polarization curves of various catalysts and (h) corresponding Tafel plots; (i) Chronopotentiometry tests of various C-RuO_2-RuSe catalysts at a constant current density of 10 mA cm^{-2} and C-RuO_2-RuSe-10 at constant current densities of 20 and 50 mA cm^{-2}, as well as chronoamperometry test of C-RuO_2-RuSe-10; (j) The free energy profiles of the OER process on RuO_2 and C-RuO_2-RuSe-10 under the applied overpotential of 0 and 1.23 V (versus RHE), respectively; insets are the optimized intermediates during OER on C-RuO_2-RuSe-10. Reproduced from reference[91]. CC BY 4.0.TEM: transmission electron microscopy; HAADF-STEM: high-angle annular dark-field scanning TEM; EDS: energy-dispersive X-ray spectroscopy; Ru: ruthenium; XANES: X-ray absorption near edge structure; OER: oxygen evolution reaction; RHE: reversible hydrogen electrode.

Combining the high-entropy concept with nanostructural engineering, Che *et al.* synthesized a high-entropy ruthenium-based oxide (RuMnFeCoNiO-HEO) with rich grain boundaries using a fast nonequilibrium molten salt method[148]. The rapid crystallization kinetics inherent to the molten salt process generate a high density of grain boundaries within the HEO nanoparticles, creating additional active sites while the entropy stabilization prevents grain boundary-induced phase separation. This dual strategy of entropy stabilization and grain boundary enrichment achieves synergistic enhancement: the grain boundaries provide abundant undercoordinated Ru sites for high activity, while the high-entropy matrix stabilizes these thermodynamically unfavorable sites against dissolution. The RuMnFeCoNiO-HEO catalyst demonstrates an overpotential of 190 mV at 10 mA cm^{-2} and exceptional stability over 100 h at 100 mA cm^{-2} in 0.5 M H_2SO_4, representing one of the best durability metrics among Ir-free Ru-based OER catalysts.

A landmark study by Qian *et al.* demonstrated that incorporating high-entropy atoms (Co, Ni, Mn, Fe, Cu) into the RuO_2 lattice activates a dual-site OPM for O_2 evolution[66]. In conventional RuO_2, the OPM requires adjacent *O intermediates to couple directly, which demands a high *O coverage that is kinetically unfavorable on uniform Ru sites. The high-entropy design creates heterogeneous dual-site pairs, comprising a Ru site and an adjacent transition metal (TM) site, with asymmetric *O adsorption energies[149]. On these Ru-TM dual sites, *O intermediates adsorbed on Ru and TM sites respectively can couple at a lower energy barrier than on two identical Ru sites, making the OPM kinetically competitive with AEM. Crucially, the OPM avoids the formation of oxygen vacancies inherent to LOM, thereby preserving lattice integrity. The high-entropy RuO_2 catalyst achieves stable operation for over 1500 h at 100 mA cm^{-2} in 0.5 M H_2SO_4 with an overpotential of 201 mV, and in a PEMWE device, it operates stably at 1 A cm^{-2} for 1,500 h.

Most recently, a data-driven high-throughput strategy has been proposed to accelerate the discovery of stable acidic OER Ru-HEO catalysts[150]. By combining literature mining with large language models (LLMs) to identify non-noble metal combinations with potential synergy with Ru, followed by DFT-based high-throughput screening of thermodynamic stability and OER activity

descriptors, this approach dramatically reduces the vast compositional search space to a tractable set of promising candidates. The LLM-guided screening identified several previously unexplored Ru-HEO compositions that exhibit predicted dissolution energies 2-3× higher than conventional RuO_2 while maintaining favorable *OH/*OOH adsorption energetics, establishing a powerful computational-experimental workflow for the rational design of next-generation Ru-HEO catalysts.

Table 3. Horizontal comparison of three core modification strategies for RuO_2-based OER electrocatalysts in acidic media[78,118,135,136,145].

Comparison Dimension	Defect Engineering	DopingStrategy	Heterointerface Construction
Core Mechanism	• Introduces oxygen vacancies, cation vacancies grain boundaries, or lattice distortions to modulate local electronic structure and create additional active sites	• Substitutes Ru lattice sites with foreign atoms to tune d-band center, Ru-O covalency, and charge redistribution	• Constructs interfaces between RuO_2 and secondary phases to enable interfacial charge transfer, oxygen spillover, and synergistic catalysis
Preferred OER Pathway	√ Suppresses LOM, promotes AEM	√ Can switch between LOM and AEM depending on dopant type	√ Enables dual-pathway catalysis
Applicable Scenarios	• When intrinsic activity of RuO_2 is limited by strong *O binding • When suppression of LOM is desired to enhance stability • Suitable for all dimensionalities	• When both activity and stability need simultaneous improvement • When precise electronic structure tuning (d-band center, Ru-O covalency) is required • Co-doping preferred when single dopant cannot break activity-stability trade-off	• When single-component catalysts cannot meet both activity and durability requirements • When oxygen spillover or interfacial electron transfer is needed to suppress Ru over-oxidation • Particularly effective for 3D architectures with conductive supports
Key Advantages	√ Directly creates additional active sites √ Relatively simple synthesis √ Can effectively suppress LOM and stabilize AEM pathway √ Grain boundaries provide both activity and stability enhancement	√ Precise electronic structure modulation via dopant selection √ Can strengthen Ru-O covalency to inhibit lattice oxygen oxidation √ Co-doping enables synergistic effects exceeding single-dopant benefits √ Well-established theoretical framework (d-band center theory)	√ Synergistic effects from multi-component interactions √ Oxygen spillover mechanism can protect RuO_2 lattice from over-oxidation √ Interfacial charge redistribution stabilizes Ru active sites √ Enables dual-pathway OER (AEM + OPM) for enhanced kinetics
Inherent Drawbacks	• Excessive vacancy concentration is counterproductive (increases energy barrier) • Uncontrolled defect density leads to structural degradation under long-term operation • Defect characterization remains challenging; precise control of defect type/concentration is difficult • Stability highly dependent on defect type: grain boundaries > oxygen vacancies > cation vacancies	• Dopant solubility limit constrains maximum loading • Some dopants may inadvertently activate LOM, accelerating degradation • High-temperature annealing required for lattice integration may cause particle aggregation • Co-doping optimization is complex; synergistic mechanism not always predictable	• Synthesis complexity increases significantly (multi-step processes) • Interfacial structure and composition difficult to precisely control • Scalability for industrial applications remains challenging • Weak interfacial coupling may lead to phase separation during prolonged operation • Limited 2D heterostructure examples compared to 1D and 3D

Ru: ruthenium; OER: oxygen evolution reaction; LOM: lattice oxygen mechanism; AEM: adsorbate evolution mechanism; 1D: one-dimensional; 2D: two-dimensional; 3D: three-dimensional; OPM: oxide pathway mechanism.

The high-entropy oxide strategy represents a paradigm shift from the conventional single-dopant approach to multi-element cooperative design for Ru-based acidic OER catalysts. Key design principles emerging from the current literature include: (1) maintaining the rutile crystal structure as the host framework to preserve the favorable Ru-O electronic configuration; (2) selecting

transition metal dopants that simultaneously modulate the Ru-O covalency (through d-band center tuning) and provide corrosion-resistant M-O bonds as sacrificial stabilization sites; (3) optimizing the entropy contribution to ensure single-phase stability while avoiding excessive lattice distortion that may compromise conductivity; and (4) leveraging the heterogeneous dual-site pairs inherent to HEOs to activate the OPM pathway, thereby achieving both high activity and lattice-preserving stability. However, challenges remain in scaling up HEO synthesis with precise compositional control, understanding the dynamic restructuring of multi-element surfaces under operando conditions, and establishing reliable structure-activity descriptors for the high-dimensional compositional space.

4.5.2 Single-atom and dual-atom Ru catalyst design

Beyond the nanostructure and compositional engineering strategies, a fundamentally different approach to breaking the activity-stability trade-off has emerged: reducing the Ru dimensionality to the atomic scale. Single-atom and dual-atom Ru catalysts maximize the atom utilization efficiency while offering unprecedented control over the local coordination environment and electronic structure of each Ru center, enabling fine-tuning of the OER mechanism at the atomic level.

The seminal work by Yao *et al.* demonstrated that a series of $PtCu_x$ /Pt_{skin} core-shell structures with atomically dispersed Ru_1 through acid etching and electrochemical leaching exhibit dramatically enhanced acidic OER activity[151]. The compressive strain imposed by the oxide support shortens the Ru-O bond length, which downshifts the Ru d-band center and optimizes the adsorption energies of *OH, *O, and *OOH intermediates. The Ru_1-Pt_3Cu catalyst achieves an overpotential of only 220 mV at 10 mA cm^{-2} in 0.5 M H_2SO_4, surpassing state-of-the-art RuO_2 by over 100 mV. More importantly, the strong Ru-O-support bonding at the single-atom site raises the dissolution energy barrier, as detaching a single Ru atom requires breaking multiple Ru-O bonds simultaneously, a process that is energetically more costly than dissolving a surface Ru atom from crystalline RuO_2 where only 2-3 bonds need to be broken. This "anchoring effect" provides inherent stability advantages for single-atom configurations.

A complementary strategy involves doping single atoms of other elements into the RuO_2 lattice to modulate the electronic structure of adjacent Ru active sites. Cheng *et al.* developed an Ir single-atom and grain boundary co-decorated RuO_2 catalyst (Ir_{SAC}-G-RuO_2) via a KCl-etching strategy[152]. The asymmetric Ru-O-Ir sites created by Ir single-atom substitution lower the activation energy for OH* generation and suppress lattice oxygen participation, as verified by *in situ* electrochemical spectroscopy. The Ir_{SAC}-G-RuO_2 catalyst exhibits a low overpotential of 189 mV at 10 mA cm^{-2} and negligible degradation over 1000 h at 50 mA cm^{-2} in 0.5 M H_2SO_4. In a PEMWE, it achieves 1.0 A cm^{-2} at 1.61 V and maintains stable operation for 200 h at 1 A cm^{-2}. This work demonstrates that even trace amounts of Ir (as single atoms rather than nanoparticles) can provide dramatic stability enhancement, offering a viable pathway to reduce Ir usage by 1-2 orders of magnitude compared to conventional IrO_2-RuO_2 composite anodes.

Similarly, Chen *et al.* reported a single-atom Co-doped core-shell Ru@RuO_2 (Co-Ru@RuO_2) catalyst synthesized via ultrafast pulse-heating and calcination[153]. The single-atom Co dopants in the RuO_2 shell modulate the electronic structure to reduce the OER energy barrier, while the metallic Ru core provides high electrical conductivity. The Co-Ru@RuO_2 catalyst achieves an overpotential of 203 mV at 10 mA cm^{-2} and 400 h stability at 10 mA cm^{-2}. Remarkably, in a PEMWE device, it achieves 1 A cm^{-2} at only 1.58 V under an ultra-low Ru loading of 0.34 mg_{Ru} cm^{-2}, and operates stably for over 200 h at 500 mA cm^{-2}.

Anchoring Ru single atoms on nitrogen-doped carbon supports represents another avenue for maximizing Ru utilization. Recent work demonstrated single-atom Ru confined in vertically aligned mesoporous carbon films (Ru-VMC) for efficient and stable acidic OER[154]. The vertically aligned mesoporous architecture provides efficient mass transport channels for water delivery and oxygen evacuation, while the Ru-N_4 coordination sites offer well-defined active centers with optimized *OH adsorption energy. The Ru-VMC catalyst achieves an overpotential of 187 mV at 10 mA cm^{-2} with exceptional stability, and the self-supported film architecture eliminates the need for binder addition in membrane electrode assemblies (MEAs) fabrication, reducing interfacial resistance. However, the long-term stability of Ru-N_4 sites under high anodic potentials (> 1.6 V *vs.* RHE) remains a concern, as the carbon support is susceptible to oxidative corrosion, potentially leading to Ru atom detachment, a challenge that must be addressed for PEMWE applications.

While single-atom catalysts maximize atom utilization, they are inherently constrained by the scaling relationship between *OH and *OOH adsorption energies on a single active site. Dual-atom catalysts (DACs), featuring two adjacent metal atoms as a cooperative active center, offer a pathway to break this fundamental limitation. In the context of Ru-based OER, two distinct dual-atom strategies have emerged:

(1) Homonuclear Ru-Ru pairs. Adjacent Ru atoms can cooperatively adsorb and couple two *O intermediates, enabling the OPM pathway that bypasses the *OOH formation step entirely. This eliminates the *OH/*OOH scaling constraint and reduces the theoretical overpotential[155]. However, achieving stable Ru-Ru pairs on conventional supports is challenging due to the tendency of Ru atoms to aggregate into nanoparticles during synthesis or operation.

(2) Heteronuclear Ru-TM pairs. The high-entropy RuO_2 system naturally creates heterogeneous Ru-TM dual-site pairs that activate the OPM. More broadly, deliberately engineering Ru-TM dual-atom sites (e.g., Ru-Co, Ru-Ni, Ru-Mn pairs) on oxide or carbon supports

enables asymmetric *O adsorption: the Ru site binds *O strongly while the TM site binds *O moderately, facilitating direct *O-*O coupling at a lower energy barrier than on two identical Ru sites. A recent computational study systematically examined dual-atom catalysts for OER and identified optimal Ru-TM combinations where the differential *O binding energy between the two sites falls within a "Goldilocks window" (0.3-0.8 eV) that maximizes the OPM rate while maintaining lattice stability[156].

Single-atom and dual-atom Ru catalysts represent the ultimate frontier of structural miniaturization for Ru-based acidic OER electrocatalysts. By reducing the catalyst dimensionality from nanoparticles to isolated atoms or atom pairs, these systems achieve near-100% Ru utilization efficiency and offer atomic-level precision in tuning the OER mechanism. Key advantages include: (1) maximized mass activity per Ru atom, enabling ultra-low Ru loadings in PEMWE anodes; (2) strong metal-support anchoring that raises the dissolution energy barrier; and (3) the ability to activate the OPM pathway through dual-site engineering, avoiding the lattice degradation associated with LOM. However, critical challenges remain: (1) the stability of single-atom sites under high-current-density PEMWE conditions has been demonstrated in only a few studies, and the long-term resistance of Ru-N_4/C sites to carbon corrosion and Ru detachment requires further validation; (2) the synthesis of well-defined dual-atom sites with controlled inter-atomic distances and coordination environments remains a significant synthetic challenge; and (3) operando characterization techniques capable of tracking the dynamic evolution of single-atom and dual-atom sites under working conditions are still under development. Future research should focus on developing robust supports (e.g., TiO_2, SnO_2) that resist anodic corrosion while providing strong anchoring for Ru single atoms, and on establishing reliable descriptors for predicting the OER mechanism (AEM *vs.* OPM *vs.* LOM) on dual-atom sites as a function of the Ru-TM pair identity and coordination geometry.

4.6 Bridging half-cell and MEA performance

While the half-cell configuration (three-electrode system in liquid electrolyte) serves as a widely adopted and standardized platform for initial screening of OER electrocatalysts, its predictive value for practical PEMWE performance must be critically evaluated. Several fundamental disparities exist between half-cell and MEA testing environments that can lead to significant discrepancies in both activity and stability assessments.

Current density gap. The majority of half-cell evaluations reported in the literature are conducted at a geometric current density of 10 mA cm^{-2}, whereas industrial PEMWE targets operate at current densities of 1-2 A cm^{-2} or higher. At such elevated current densities, the oxygen evolution rate increases dramatically, imposing severe demands on gas bubble removal, mass transport, and the mechanical integrity of the catalyst layer. Catalysts that exhibit stable performance at 10 mA cm^{-2} may experience accelerated degradation at industrial current densities due to intensified local pH gradients, enhanced Ru over-oxidation, and mechanical stress from vigorous O_2 evolution[11,157].

Mass transport and three-phase boundary. In half-cell tests, the catalyst is typically deposited as a thin film on a glassy carbon electrode or carbon paper with minimal Nafion content, ensuring facile electrolyte access and gas release. In contrast, the MEA configuration involves a complex catalyst layer incorporating ionomer, where the three-phase boundary (electronic conductor/proton conductor/reactant) governs the reaction kinetics. The ionomer distribution, catalyst layer porosity, and porous transport layer/catalyst layer interface collectively determine the mass transport efficiency, which becomes the performance-limiting factor at high current densities[19,158].

Stability assessment discrepancy. A critical concern is that half-cell stability tests, typically performed at 10 mA cm^{-2} for tens to hundreds of hours, may not capture the degradation pathways operative under realistic PEMWE conditions. As demonstrated by recent studies, catalysts showing negligible degradation in half-cell configurations can fail rapidly in MEA tests due to Ru dissolution into the membrane, catalyst layer delamination, or membrane contamination by dissolved Ru species[127,159]. Furthermore, the S-number metric proposed by Geiger *et al.* for quantifying catalyst stability through dissolved metal amounts provides a more rigorous comparison framework, yet it remains underutilized in the RuO_2 literature[28].

Therefore, while half-cell data provide valuable insights into intrinsic catalytic activity and mechanistic understanding, extrapolation to PEMWE performance requires careful consideration of these disparities. Future studies should prioritize MEA-level validation under industrially relevant conditions to bridge the gap between laboratory screening and practical deployment.

The modification strategies and performance metrics discussed in the preceding sections have been predominantly evaluated in three-electrode half-cell configurations. However, the ultimate validation of RuO_2-based electrocatalysts lies in their integration and performance within operational PEMWE devices. The following section examines the structural components of PEMWE systems, the current status of RuO_2 deployment in membrane electrode assemblies, and the industrial development trajectory of PEMWE technology.

5. The Applications of RuO_2-Base Nanomaterials in PEMWE

5.1 The components of PEMWE

A standard PEMWE stack comprises end plates, insulating layers, bipolar plates, sealing gaskets, porous transport layers, and MEAs

(Figure 14). The end plates provide mechanical compression to ensure intimate interfacial contact across all layers. Bipolar plates, typically Ti-based on the anodic side due to carbon's susceptibility to oxidative corrosion at high anodic potentials, serve as current collectors, flow-field distributors for reactant water and product gases, and physical compartmentalizers between adjacent cells[160]. Sealing gaskets (silicone rubber, fluor elastomer, or PTFE) prevent gas crossover and external leakage while providing electrical insulation between bipolar plates and PTL. The PTL and MEAs are the components that most directly govern the performance and durability of RuO_2-based anodes, and their interplay with the catalyst layer is discussed in detail below.

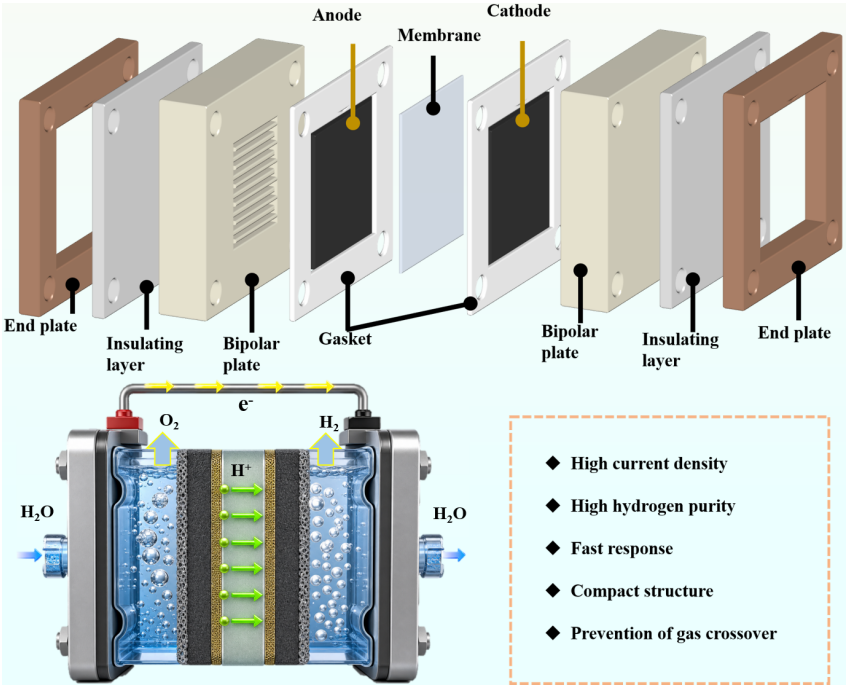


Figure 14. Schematic diagram and advantages of the PEMWE device.

5.1.1 Porous transport layers of PEMWE

The anodic PTL, typically sintered Ti fiber felt or multi-layered Ti mesh with gradient porosity, plays a far more critical role in determining RuO_2 anode performance than is commonly appreciated. Three PTL-catalyst layer interaction mechanisms directly influence RuO_2 activity and durability in operational PEMWE:

(1) Interfacial contact resistance and catalyst utilization. The rough surface morphology of sintered Ti felts creates localized high-contact-pressure points against the RuO_2 catalyst layer, while leaving adjacent regions with poor electrical contact. This non-uniform contact distribution leads to heterogeneous current density across the catalyst layer: regions in direct contact with Ti fiber tips experience disproportionately high local current densities, accelerating Ru dissolution at these hotspots. Conversely, catalyst material in poorly contacted regions remains electrochemically underutilized.

(2) Water transport and oxygen bubble management. At current densities exceeding 1 A cm^{-2}, the volumetric oxygen evolution rate at the anode becomes substantial, generating oxygen bubbles that can temporarily block water access to RuO_2 active sites within the catalyst layer. The PTL pore structure governs the efficiency of two-phase water supply/oxygen removal: excessively dense PTLs impede oxygen evacuation, causing local catalyst "flooding" with trapped O_2 that blocks reactant water access and creates local hotspots of elevated overpotential; excessively open PTLs compromise mechanical support and may allow catalyst layer intrusion into flow-field channels. For RuO_2 catalysts, which are already kinetically disadvantaged relative to IrO_2 at high overpotentials due to their dissolution susceptibility, inefficient oxygen removal exacerbates the problem by pushing the local anode potential even higher, thereby accelerating RuO_4 formation and catalyst loss.

(3) PTL corrosion and RuO_2 contamination. Under anodic operating conditions, the Ti PTL surface undergoes progressive oxidation, forming a TiO_2 passivation layer that increases interfacial contact resistance over time. This passivation forces the RuO_2 catalyst layer to operate at increasingly higher local overpotentials to maintain the imposed current density, accelerating Ru dissolution. Furthermore, dissolved Ti species can migrate into the catalyst layer and deposit on RuO_2 surfaces, partially blocking active sites. Iridium-coated or platinum-coated Ti PTL mitigate this passivation but add cost; alternative approaches using corrosion-resistant ceramic coatings on Ti felts are under investigation specifically for RuO_2-based anodes where the cost margin is tighter than for IrO_2 systems[161].

As the heart of the PEMWE device, the membrane electrode assembly provides the essential interface at which the electrochemical reactions proceed[162]. Its layered configuration integrates an anode catalyst layer, a proton exchange membrane, and a cathode catalyst layer into a unified assembly. For the anodic catalyst layer, IrO_2 is the most prevalent choice despite its high cost, whereas RuO_2 offers enhanced catalytic activity at the expense of diminished operational durability. The catalyst layer is typically fabricated by incorporating the active catalyst into a Nafion polymer matrix, thereby forming a composite catalytic film. The anode catalyst layer provides reactive sites where water, protons, and electrons come into contact simultaneously, thereby catalyzing the oxygen evolution reaction and accelerating the decomposition of water. The OER acts as the bottleneck process in PEMWE systems; thus, the electrocatalytic activity and operational robustness exhibited by the anode catalyst exert a direct and profound influence on the electrolysis performance efficiency and durability.

5.1.2 MEA assembly of PEMWE

The translation of RuO_2 catalyst powder into a functional MEA anode involves multiple processing steps, including ink formulation, coating/deposition, drying, and hot-pressing, each of which can profoundly alter the catalyst's microstructure, electronic environment, and ultimately its OER performance and durability. These fabrication-induced effects are frequently overlooked in laboratory studies that report only three-electrode half-cell data, yet they represent a primary source of the lab-to-device performance gap for RuO_2 catalysts.

(1) Catalyst ink formulation and ionomer-catalyst interaction. The anode catalyst ink typically consists of RuO_2 powder, Nafion ionomer solution, and a solvent system (water/alcohol). The ionomer-to-catalyst ratio (I/C ratio) critically governs the catalyst layer's proton conductivity, electronic percolation, and porosity. For RuO_2, the optimal I/C ratio differs significantly from that for IrO_2: RuO_2's more hydrophilic surface chemistry leads to stronger interaction with the sulfonic acid groups of Nafion, causing the ionomer to adsorb preferentially on RuO_2 surfaces and form thicker ionomer films. This thicker ionomer coverage can impede electron transport between adjacent RuO_2 particles and block reactant water access to active sites, particularly at high current densities where mass transport through the ionomer film becomes rate-limiting.

(2) Coating method and catalyst layer morphology. Two primary MEA fabrication approaches are employed: catalyst-coated membrane (CCM) and catalyst-coated substrate (CCS). For RuO_2 anodes, the CCM method, where the catalyst ink is directly coated onto the proton exchange membrane, presents specific challenges: (a) the acidic Nafion membrane surface can partially dissolve RuO_2 nanoparticles during the coating process, especially when alcohol-based solvents are used, leading to Ru loss before the MEA is even assembled; (b) the thin, dense catalyst layers produced by CCM can suffer from severe oxygen bubble accumulation at high current densities, as the limited pore volume provides insufficient pathways for O_2 evacuation. The CCS method, coating the catalyst onto the PTL, avoids membrane exposure to the ink solvent and produces thicker, more porous catalyst layers that facilitate gas release, but at the cost of higher catalyst loading and potentially poorer membrane-catalyst interfacial contact.

(3) Hot-pressing effects on RuO_2 crystallinity and stability. The hot-pressing step used in MEA assembly can alter the crystalline structure and defect state of RuO_2 catalysts. For amorphous or low-crystallinity RuO_2, hot-pressing can induce partial crystallization, reducing the density of catalytically active defect sites and shifting the OER mechanism from the beneficial AEM pathway back toward the detrimental LOM pathway[141]. For nanocrystalline RuO_2 with grain boundaries, the applied pressure can cause grain boundary collapse and particle agglomeration, reducing the active surface area[57]. These hot-pressing-induced structural changes are rarely characterized in the literature but can account for 20–40% of the performance loss observed when transitioning from half-cell to MEA testing. Optimized low-temperature assembly protocols (e.g., decal transfer at < 100 °C) have been proposed to preserve the as-synthesized RuO_2 nanostructure during MEA fabrication.

5.1.3 High-current-density attenuation mechanisms

The degradation behavior of RuO_2 catalysts under industrial PEMWE operating conditions differs fundamentally from that observed in laboratory three-electrode cells at 10 mA cm^{-2}. Understanding these high-current-density attenuation mechanisms is essential for rational design of durable RuO_2-based anodes.

(1) Potential-dependent dissolution acceleration. At current densities of 1–3 A cm^{-2}, the anode potential in a PEMWE typically reaches 1.5–1.8 V *vs.* RHE, well above the thermodynamic threshold for RuO_4 formation. This dramatic acceleration arises from two synergistic factors: (a) the higher anodic potential directly increases the thermodynamic driving force for $Ru^{4+} \rightarrow Ru^{8+}$ (RuO_4) oxidation; (b) the local pH at the catalyst/membrane interface drops significantly due to the high proton generation rate at large current densities, creating an even more corrosive microenvironment.

(2) Oxygen bubble-induced mechanical degradation. At high current densities, the vigorous oxygen evolution creates substantial mechanical stress within the catalyst layer. Oxygen bubbles nucleating at RuO_2 active sites exert localized pressure pulses that can physically dislodge catalyst particles from the ionomer matrix, crack the catalyst layer, and delaminate the catalyst layer from either the membrane or the PTL. This mechanical degradation mode is particularly severe for RuO_2 because: (a) RuO_2's higher OER activity generates oxygen at a faster rate than IrO_2 at equivalent overpotentials, producing more frequent and larger bubble events; (b) the

thinner ionomer films on RuO_2 surfaces provide weaker adhesion between catalyst particles.

(3) Reverse current degradation during shutdown. When a PEMWE system is shut down, the dissolution of residual oxygen at the anode and hydrogen at the cathode can create a galvanic cell that drives a reverse current through the MEA. This reverse current reduces the anode potential below the OER range, causing reduction of surface RuO_2 to metallic Ru, which upon subsequent restart re-oxidizes to a less stable, more amorphous RuO_x phase with higher dissolution susceptibility. Protective countermeasures, including maintaining a small anodic holding current during idle periods or employing recombination catalysts within the MEA, are essential for RuO_2-based PEMWE durability but are rarely discussed in the catalyst design literature.

(4) Ionomer degradation and catalyst layer restructuring. Under prolonged high-current operation, the Nafion ionomer within the RuO_2 catalyst layer undergoes chemical degradation via attack by reactive oxygen species (*OH, *OOH radicals) generated as OER intermediates. This ionomer degradation reduces proton conductivity within the catalyst layer, creates hydrophobic patches that impede water access, and weakens the mechanical integrity that holds RuO_2 particles in place. The loss of ionomer connectivity forces the remaining current to concentrate in still-conductive regions, creating local current density hotspots that further accelerate Ru dissolution, a positive feedback loop that leads to accelerating (rather than linear) degradation. This mechanism explains the commonly observed "knee" in PEMWE durability curves, where the cell voltage increases slowly for an extended period before entering a regime of rapid performance decline.

The main function of the PEM is to conduct the H^+ ions generated at the anode in the form of hydrated ions to the cathode, serving as the core channel for ion conduction in electrolysis. The proton exchange membrane can prevent the mutual penetration and mixing of oxygen at the anode and hydrogen at the cathode, ensuring the purity and safety of the gases, while also preventing electrons from passing through the membrane, forcing the electrons to flow only through the external circuit. It should be noted that the membrane needs to maintain a proper hydration state to maintain high proton conductivity. In practical applications, the thickness of the membrane and its proton conductivity directly affect the ohmic overpotential. The membrane can reduce resistance loss and improve efficiency, but if it is too thin, it will increase the risk of gas cross-penetration and mechanical strength issues.

The performance optimization of PEM materials is crucial for enhancing the efficiency and lifespan of PEMWE systems. Currently, mainstream perfluoro sulfonic acid membrane materials such as Nafion and Aquivion have achieved significant performance improvements through modification techniques such as nanofiber doping. Although these materials possess excellent ionic conductivity and chemical stability, they still have obvious drawbacks in practical applications: the Nafion membrane exhibits water swelling at temperatures above 100 °C, while the Aquivion material, although having better high-temperature resistance, faces the technical challenge of gas cross-penetration[163]. To address this issue, surface engineering and coating techniques are employed to construct an intermediate layer structure between the two electrodes and catalyst support membranes, which has been proven to effectively inhibit hydrogen permeation[53]. For the cathode catalyst layer, Pt/C is mostly used as the catalyst, providing reaction active sites where protons, electrons, and hydrogen gas can simultaneously come into contact. This enables the hydrogen evolution reaction to accelerate the reduction of protons into hydrogen gas.

5.2 The application of RuO_2 in PEMWE

Under high current density conditions, the electrolysis has more stringent requirements for the coordination of each component. An ideal PEMWE should not only have excellent proton conductivity but also effectively prevent gas cross-penetration, eliminating the safety risks caused by hydrogen-oxygen mixture. The catalyst layer needs to maintain structural integrity in the high potential environment and avoid performance decline due to excessive oxidation. The porous transport layer must optimize its pore structure to ensure efficient transportation of reactants and products, while maintaining good electron conductivity. The synergy between these key components directly affects the comprehensive performance of the electrolysis under high current density conditions.

The high anodic potentials and acidic environment in PEMWE promote RuO_2 dissolution via formation of soluble RuO_4^{2-}, resulting in permanent loss of active sites. The core challenge lies in designing anode OER catalysts that maintain both activity and durability under these harsh conditions. This critical issue severely restricts the industrialization process of PEMWE. It is worth noting that at current densities above 1 A cm^{-2}, the dissolution and deactivation of the catalysts will significantly intensify, presenting a dilemma for material design in balancing activity and stability. Notably, at current densities above 1 A cm^{-2}, catalyst dissolution and deactivation are significantly exacerbated, presenting a dilemma for material design in balancing activity and stability. Operando characterization under PEMWE operating conditions has provided critical insights into the degradation mechanisms of RuO_2 catalysts at industrially relevant current densities. Post-operando ICP-MS analysis of MEA components has further quantified the dramatically different Ru dissolution rates: commercial RuO_2 loses > 50% of its Ru loading within 100 h at 1 A cm^{-2}, while $Ta_{0.1}Ru_{0.9}O_{2-x}$ exhibits a dissolution rate of only 14 μV h^{-1} over 2,800 h[164]. These operando and post-operando findings under realistic PEMWE conditions represent the most stringent validation of catalyst stability and should serve as essential benchmarks for the field.

In the performance regulation of RuO_2 catalysts, lattice strain engineering demonstrates unique advantages. Taking the Sr/Ta co-doped RuO_2 system as an example, the effective control of the internal stress distribution enables precise regulation of Ru-O bond length and oxygen vacancy concentration[50]. Experimental observations show that the increase in Ru-O bond length caused by the

strain effect promotes the reduction of Ru oxidation state, thereby inhibiting the formation of oxygen vacancies and the participation of lattice oxygen in the reaction process. The catalyst exhibits excellent oxygen evolution reaction activity under acidic conditions while maintaining great stability, at 500 mA cm^{-2} in PEMWE without apparent degradation (Figure 15a,b,c), presenting the promising potential for large-power applications. Beyond lattice strain engineering through dopant incorporation, defect architecture design offers a complementary approach to stabilizing RuO_2 under high-current-density conditions. The multi-scale defect RuO_2 double continuous nanoreactor (MD-RuO_2-BN) prepared by molten salt-assisted synthesis exhibits rich defect structures, including Ru vacancies, O vacancies, and inter-atomic boundaries[104]. HR-TEM and XRD analysis confirm that the KCl-LiCl molten salt system plays a key role in defect formation at 500 °C. Theoretical simulations reveal that the low-coordination Ru atoms at the defect sites not only enhance catalytic activity but also effectively inhibit the oxidation of lattice oxygen and the dissolution of high-valent Ru through weakening the Ru-O interaction. This unique double-continuous structure also has excellent mass transport properties, creating a favorable environment for catalytic reactions under high current density conditions. Therefore, a PEMWE single cell consisting of CCM, porous transport layers, and bipolar plates was finally installed (Figure 15d,e). Time-dependent current density curves (Figure 15f) reveal that MD-RuO_2-BN-based electrolysis well maintains water electrolysis activity for 50 h, while both K-RuO_2 and C-RuO_2 experience clear decline within only 25 h of operation, especially C-RuO_2. An alternative strategy for modulating lattice strain involves electrochemical lithium intercalation, which induces lattice expansion and electronic structure modification through a fundamentally different mechanism. The study of electrochemical lithium intercalation modified RuO_2 systems reveals the synergistic mechanism of strain and defect. The solid solution phase of $LixRuO_2$ formed during the constant current charge-discharge process causes lattice expansion and changes in electronic structure[13]. XAS analysis indicates that lithium electron injection reduces the Ru valence, weakens the covalent nature of Ru-O bonds, and the formation of the Li-O-Ru local coordination structure effectively inhibits Ru dissolution. This coordinated regulation strategy of electronic structure and lattice strain provides a new direction for the design of highly stable catalysts. Chrono-potential test results confirm that the modified samples have significantly improved durability.

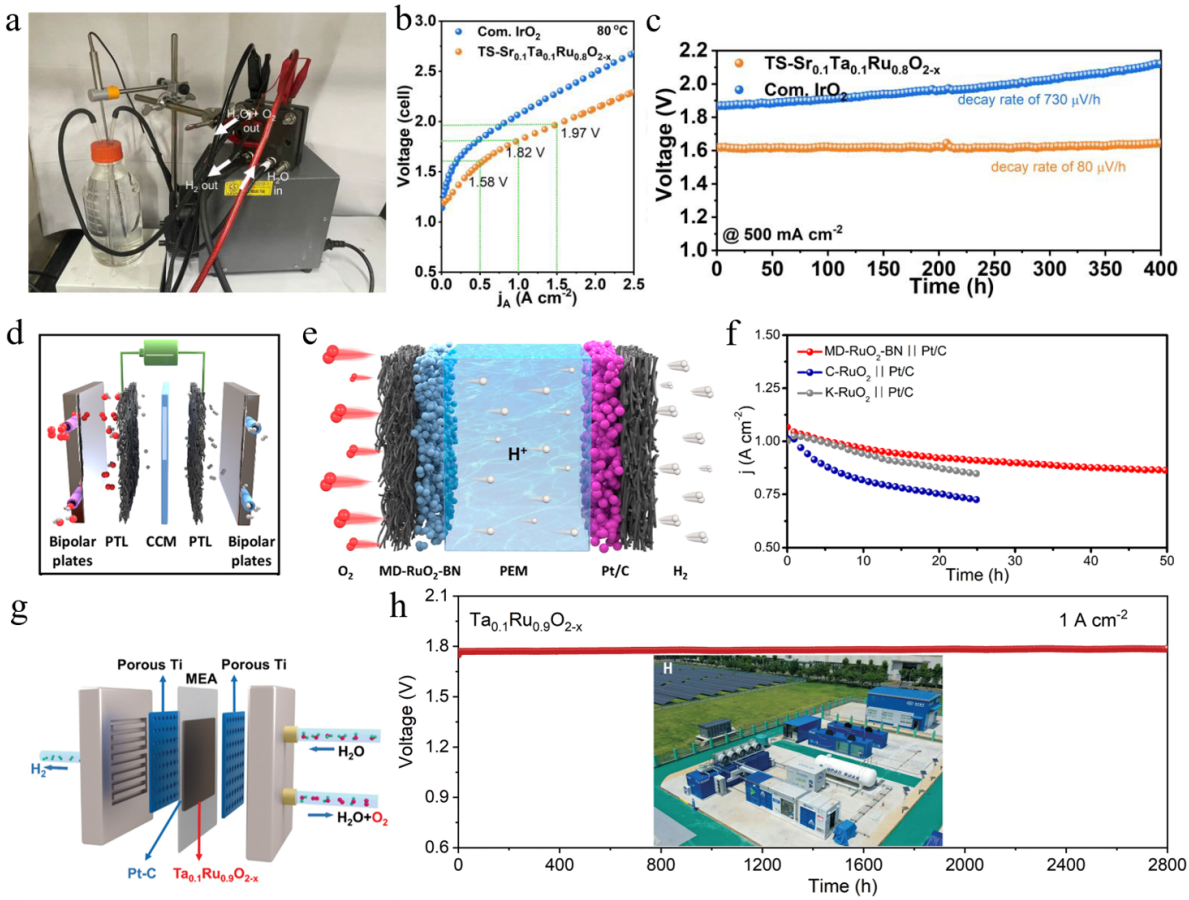


Figure 15. (a) The photograph shows the PEMWE system to produce the H_2 (80 °C); (b) Polarization curves of the PEMWE using commercial IrO_2 and our TS-$Sr_{0.1}Ta_{0.1}Ru_{0.8}O_{2-x}$ as anode catalyst; (c) Chronopotentiometry curve of the PEMWE using IrO_2 and our TS-$Sr_{0.1}Ta_{0.1}Ru_{0.8}O_{2-x}$ catalyst operated at 500 mA cm^{-2}. Reproduced from reference[50]. CC BY 4.0; Schematic diagram of a typical PEMWE device (d) and the MEA components (e); (f) Time-dependent current density curves of the PEMWE measured at 80 °C, no *iR*-correction. Reproduced from reference[104]. CC BY 4.0; (g) Illustration of a single-cell PEMWE; (h) Voltage-time curves of PEMWE with $Ta_{0.1}Ru_{0.9}O_{2-x}$. Reproduced from reference[164]. CC BY 4.0. PEMWE: proton exchange membrane water electrolysis; MEA: membrane electrode assembly.

Current research still faces several technical challenges. Although hetero-metal doping can introduce local compressive stress layers (such as the repulsive effect of Pt doping on adjacent Ru atoms), maintaining uniform strain distribution in large-scale production remains difficult. DFT calculations show that the lowering of the d-band center of the doped Ru region can weaken the adsorption of oxygen intermediates, but this effect highly depends on the precise control of the doping element. Similarly, the defect structure prepared by the molten salt method has excellent catalytic performance, but its preparation process is extremely sensitive to temperature control and raw material ratios. The breakthroughs in these technical challenges will directly affect the practical application effect of strain and defect engineering in PEMWE.

The performance optimization of RuO_2-based catalysts mainly relies on doping and alloying strategies, especially in the application of acidic OER. Taking Ta-doped RuO_2 (Ta-RuO_2) as an example, this catalyst exhibited stability close to IrO_2 in industrial tests[164]. After 2,800 h of continuous operation, the performance decay rate was only 14 μV h^{-1}, which is much better than traditional RuO_2 catalysts, as shown in Figure 15g,h. It was found that the strong corrosion resistance of Ta-O bonds and the electron transfer process from Ta to Ru through the oxygen bridge can effectively stabilize Ru sites and prevent the dissolution and excessive oxidation of surface Ru active sites[165]. The optimized Ta_1/RuO_2 catalyst operated continuously for 1,000 h at a current density of 100 mA cm^{-2} and achieved a working voltage of 1.58 V in a PEMWE cell system[166].

The research on multi-element doping systems indicates that the synergistic effect between different elements can further enhance catalytic performance. For example, the formation of $Nb_{0.1}Mn_{0.1}Ru_{0.8}O_2$ nanoparticles by co-doping Nb and Mn requires only 209 mV overpotential to reach a current density of 10 mA cm^{-2} in a three-electrode system, and can operate stably for more than 1,000 h in a PEMWE device at a current density of 0.5 A cm^{-2}, with a decay rate of only 59 μV h^{-1} (Figure 16a,b)[145]. Similarly, the Ta/B co-doping system also shows significant synergistic effects. The Ta/B-RuO_2 electrolysis can achieve a high current density of 1.0 A cm^{-2} at a voltage of 1.6 V and operate stably for more than 120 hours at a current density of 200 mA cm^{-2}[142]. DFT calculations further confirm that the doping of Ta and B will cause electronic structure rearrangement, optimize the rate-determining step, reduce the energy barrier, and improve overall durability. The doping of rare earth elements provides a new research direction for the performance regulation of RuO_2. Taking Gd ($4f^7$ half-filled) doping as an example, this doping causes the Ru-O bond length to increase from 1.90 Å to 1.98 Å, and the absolute value of Integrated Crystal Orbital Hamilton Populations (ICOHP) to decrease from -2.01 to -1.66, indicating a weakening of Ru-O covalency[168].

When carbon-based materials are used as the carrier for RuO_2 catalysts, their electron supply effect and interface anchoring function are particularly prominent. The latest research has found that the ultra-small RuO_2 nanoparticles embedded on the surface of carbon nanosheets (RuO_2/C) can form significant interfacial interactions. XPS and EPR spectral data clearly reveal the phenomenon of electron transfer from the carbon carrier to the RuO_2 nanoparticles[167]. This electron transfer not only effectively inhibits the peroxidation process of Ru, but also significantly increases the oxygen vacancy concentration on the catalyst surface. HAADF-STEM characterization confirmed the uniform dispersion state of the ultra-small RuO_2 nanoparticles on the carbon nanosheets, and this unique structural feature effectively prevented the excessive growth of RuO_2 particles, demonstrating excellent stability in 450-h continuous tests, with a degradation rate of only 0.035 mV h^{-1} (Figure 16c). The core-shell structure design provides an effective interface protection strategy for RuO_2 catalysts. The HR-TEM study of the Co-Ru@RuO_2 catalyst showed that after the OER reaction, the core-shell structure of the nanoparticles remained intact, and the crystal structure did not undergo significant changes[153]. In the actual PEMWE device tests, the Co-Ru@RuO_2 catalyst was used in combination with the commercial Pt/C (20%) cathode in the Nafion 115 membrane system, demonstrating excellent overall performance, as shown in Figure 16d,e,f.

The design of the porous framework structure requires a balance between mass transfer efficiency and mechanical stability. The RuO_2/C catalyst achieved uniform dispersion of ultra-small RuO_2 nanoparticles on the carbon nanosheets through an optimized two-step heat treatment process. This porous structure not only provides abundant mass transfer channels but also exposes many active sites. However, under high current density conditions, the mechanical strength of the porous structure may be insufficient, leading to the destruction of the catalyst layer structure. By precisely controlling the heat treatment parameters and optimizing the morphology of the carbon nanosheets, the mechanical stability of the porous structure can be significantly improved while maintaining excellent mass transfer performance, enabling it to adapt to the long-term operation requirements under high current density.

The concept of strong metal-support interaction (SMSI) was first introduced by Tauster *et al.* in 1978 for gas-phase heterogeneous catalysis, describing the dramatic changes in chemisorption properties of group 8-10 metals supported on TiO_2 after high-temperature reduction[169]. In the context of electrocatalysis at electrified solid-liquid interfaces, SMSI manifests through fundamentally different but equally critical mechanisms that govern both the activity and stability of OER catalysts. Oh *et al.* provided the first experimental evidence for electronic catalyst-support interactions in electrochemical environments, demonstrating that antimony-doped tin oxide (ATO) supports stabilize IrO_x nanoparticles in sustained lower oxidation states, thereby suppressing the growth of higher-valent Ir oxide layers that compromise catalyst stability[170]. This landmark study established the concept of metal/metal-oxide support interaction (MMOSI) in electrochemistry and revealed that SMSI effects, largely neglected in the past, may be more important for understanding the durability of oxide-supported nanoparticle OER catalysts than previously thought.

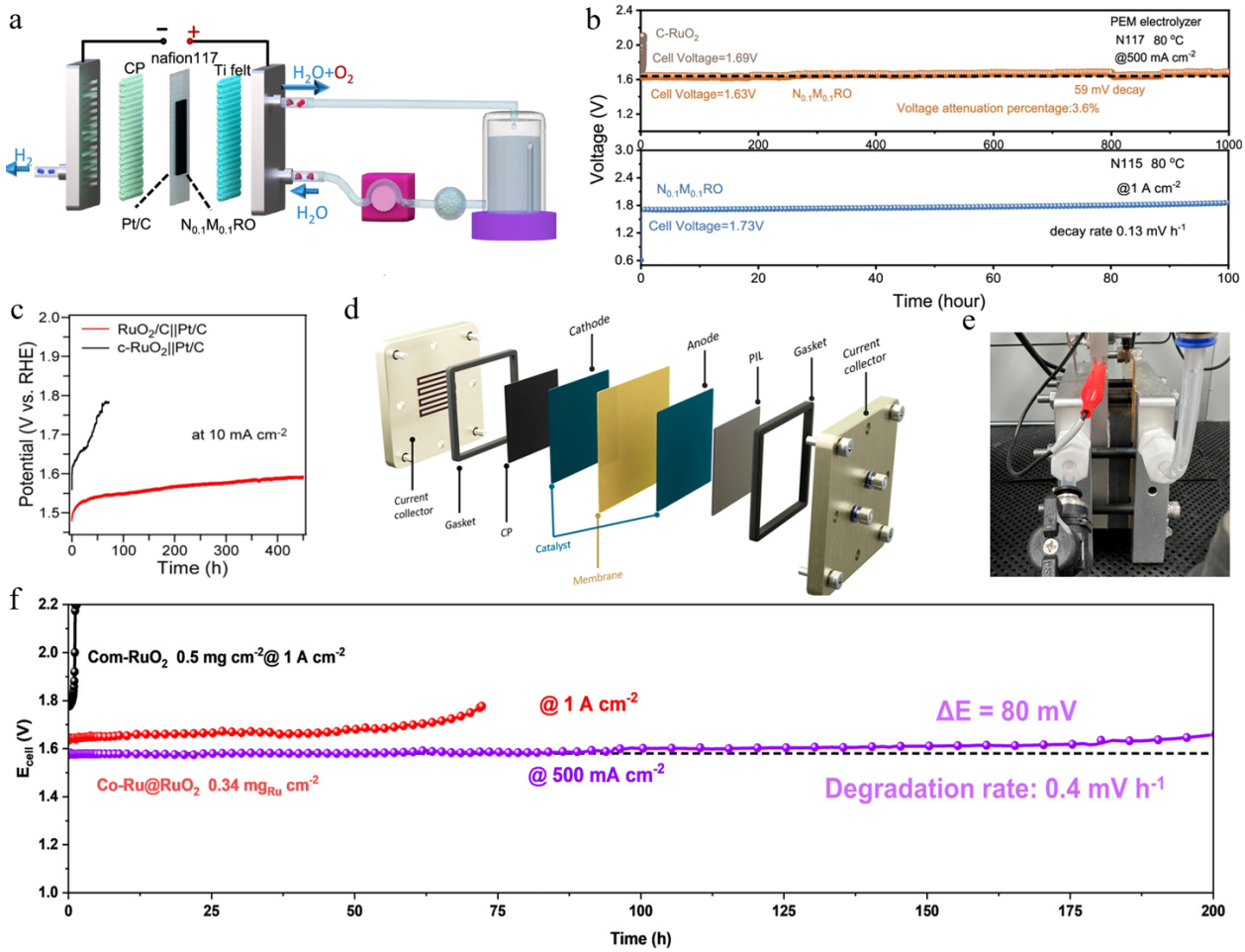


Figure 16. (a) Schematic diagram of the PEMWE device; (b) Chronopotentiometry curve of the PEMWE under 500 mA cm^{-2} (top) and 1 A cm^{-2} (bottom). Reproduced from reference[145]. CC BY 4.0; (c) Electrochemical OWS stability of RuO_2/C||Pt/C and c-RuO_2||Pt/C. Reproduced with permission from reference[167]. Copyright © 2025 Elsevier; (d) Schematic illustration and (e) digital photograph of a single-cell PEMWE; (f) Chronopotentiometry testing of the Co-Ru@RuO_2 catalyst at 500 and 1,000 mA cm^{-2} and commercial RuO_2 at 1,000 mA cm^{-2} in the PEMWE at 60 °C and ambient pressure. Reproduced with permission from reference[153]. Copyright © 2025 American Chemical Society. PEMWE: proton exchange membrane water electrolysis; Ru: ruthenium; RHE: reversible hydrogen electrode; OWS: overall water splitting.

The work function (Φ) difference between the catalyst and support drives interfacial electron transfer, fundamentally altering the electronic structure of the active metal sites. The direction and magnitude of charge transfer depend not only on the bulk work functions but also on the interfacial bonding geometry, the oxidation state of the support surface, and the presence of defects (oxygen vacancies, dopants). For example, reduced TiO_{2-x} (with oxygen vacancies) has a lower effective work function than stoichiometric TiO_2, leading to stronger electron donation to RuO_2[171]. SMSI provides geometric stabilization through multiple mechanisms that physically anchor catalyst nanoparticles to the support, preventing Ostwald ripening, coalescence, and detachment[172]. For example, strong Ru-O-W bridge bonds at the catalyst-support interface create robust chemical anchors[173]. When the lattice parameters of the catalyst and support are closely matched, epitaxial growth minimizes interfacial strain and maximizes the interfacial contact area, creating strong adhesion[47]. Porous or layered supports physically confine RuO_2 nanoparticles within their pore structure, preventing migration and agglomeration. The confinement effect scales inversely with pore size: smaller pores provide stronger spatial restriction but may limit mass transport[174].

The stability of RuO_2-based catalysts under realistic PEMWE operating conditions represents a fundamentally different challenge from that observed in half-cell configurations. Industrial PEMWE operation imposes multiple concurrent stressors that synergistically accelerate catalyst degradation.

High current density degradation. At current densities exceeding 1 A cm^{-2}, the anode potential typically reaches 1.6–2.0 V *vs.* RHE, which is well above the thermodynamic threshold for RuO_4 formation (~ 1.39 V *vs.* RHE). Under such highly oxidizing conditions, the dissolution rate of Ru increases exponentially with potential, as described by the thermodynamic-kinetic framework established by Cherevko *et al.*[11] Recent work by Zhang *et al.* demonstrated that Ta-stabilized RuO_2 can operate continuously for 2,800 h at 1 A cm^{-2} with a degradation rate of only 14 μV h^{-1}, attributed to the strong Ta-O bonds and electron transfer from Ta to Ru through oxygen

bridges that stabilize surface Ru sites[164]. Similarly, Yuan *et al.* reported that Nb/Mn co-doped RuO_2 maintained stable operation for over 1000 h at 0.5 A cm^{-2} in PEMWE with a decay rate of 59 μV h^{-1}[145]. These results underscore that strategic doping can effectively suppress the over-oxidation pathway that dominates at high anodic potentials.

Ru dissolution mechanisms under operating conditions. The dissolution of Ru under OER conditions proceeds through two primary pathways: (1) electrochemical oxidation of surface Ru^{4+} to soluble RuO_4, which is particularly favored at potentials above 1.4 V *vs.* RHE in acidic media; and (2) lattice oxygen-mediated degradation, where the participation of lattice oxygen in the OER (LOM pathway) creates oxygen vacancies that destabilize the local Ru coordination environment and promote cation dissolution[70]. Under PEMWE operating conditions, the continuous flow of water through the anode compartment facilitates the removal of dissolved Ru species, preventing their redeposition and leading to irreversible catalyst loss. ICP-MS analysis of the effluent water from PEMWE cells has revealed Ru dissolution rates on the order of ng h^{-1} cm^{-2} even for stabilized catalysts, which, while seemingly low, can accumulate to significant active site loss over thousands of hours of operation[167].

Temperature effects. Industrial PEMWE typically operates at 60–80 °C, which accelerates both the OER kinetics and the degradation processes. Elevated temperatures increase the rate of RuO_4 formation and volatilization, while also promoting ionomer degradation and membrane thinning. The interplay between thermal and electrochemical degradation pathways necessitates stability evaluation at operating temperatures rather than ambient conditions commonly used in half-cell tests.

Membrane contamination. Dissolved Ru species can migrate into the proton exchange membrane and redeposit, leading to increased membrane resistance, hydrogen crossover, and eventual cell failure. This degradation mode is unique to MEA configurations and cannot be captured by half-cell testing. Post-mortem analysis of degraded MEAs has revealed Ru accumulation at the membrane/cathode interface, confirming the crossover of dissolved Ru species[153]. Therefore, the stability criterion for PEMWE anode catalysts must encompass not only the preservation of catalytic activity but also the minimization of Ru dissolution to prevent membrane contamination.

5.3 Industrial development of PEMWE

5.3.1 Market and policy background of PEMWE

PEMWE has become an important solution in the field of green hydrogen production. This technology utilizes PEMs to achieve efficient water decomposition, featuring high current density and rapid dynamic response among other notable characteristics. Notably, the U.S. Department of Energy's Hydrogen and Fuel Cell Technologies Office (HFTO) established technical targets for PEM electrolysis in its Multi-Year Program Plan, including the ambitious goals of reducing the cost of clean hydrogen production to $2 per kilogram by 2026 and to $1 per kilogram by 2031, alongside electrolyzer system cost targets of $250/kW and an operational lifetime target of 80,000 hours[175], through a comprehensive improvement in performance, efficiency, lifespan, and cost. Therefore, it is imperative to design and develop high-performance, long-lasting and low-cost PEMWE to achieve the hydrogen production cost target.

From 2020 to 2026, the PEMWE technology achieved a significant breakthrough from laboratory research to industrial application. At the international level, different countries have adopted different promotion strategies: The EU is committed to technological standardization through the H2Giga program; the Chinese government has incorporated hydrogen energy development into the "Medium and Long-Term Development Plan for Hydrogen Energy Industry", establishing its important position in the national energy system. The United States mainly relies on tax incentives to promote commercial applications. This diverse policy support not only created a favorable development environment for the PEMWE technology, but also demonstrated its crucial role in the global carbon neutrality process.

The global PEMWE hydrogen production equipment market is projected to grow significantly from 2025 to 2030, driven by increasing clean energy demand and government policy support. The global market was valued at approximately $5 billion in 2024 and is expected to exceed $20 billion by 2030. According to the IEA Global Hydrogen Review 2024, global installed water electrolyser capacity reached 1.4 GW by the end of 2023 and could reach 5 GW by the end of 2024, with China accounting for 60% of global electrolyser manufacturing capacity[176]. This growth is mainly driven by the strong demand in the Asia-Pacific region, especially in the Chinese market. As the world's largest energy consumer and an important country for hydrogen energy development, China's policy support and market demand have provided broad development space for the PEMWE hydrogen production equipment market.

China has made particularly significant progress in the market for PEMWE hydrogen production equipment. According to the IEA Global Hydrogen Review 2024 and the China Hydrogen Alliance's 2024 Annual Report on the Development of China's Hydrogen Energy Industry, China's operational electrolyser capacity has grown rapidly, with total installed capacity reaching approximately 1.15 GW by the end of 2024, of which 493.4 MW were newly added in 2024[176]. This growth is attributed to the strong support from the Chinese government and the continuous investment in technological research and development and market expansion by Chinese enterprises.

According to the IEA Global Hydrogen Review 2025, global installed capacity of water electrolysis reached 2 GW in 2024, with

continued rapid growth driven primarily by China[177]. PEM electrolysis technology holds particular advantages in specific application scenarios requiring high-purity hydrogen, fast dynamic response for coupling with fluctuating renewable power sources, and compact system design for distributed applications, as documented by the IEA[176]. At present, more than 18 enterprises have launched new PEMWE products in China. CSS PeiRi Hydrogen Energy (formerly 718 Institute) is one of the earliest units to enter the engineering stage in China. In addition, companies such as Sunlight Hydrogen Energy, Coakley & Riddle, and LONGi Hydrogen Energy are all accelerating their commercialization plans.

The megawatt-level PEM electrolysis water hydrogen production unit was jointly developed by Sinopec Research Institute of Petroleum and Yanshan Petrochemical Company[178]. It is a proton exchange membrane electrolysis water hydrogen production equipment. It was officially put into operation in 2022. This device adopts the most domestically manufactured single-cell megawatt-level PEM electrolysis water hydrogen production complete set of equipment. The hydrogen production capacity reaches 250 standard cubic meters per hour, with a hydrogen purity of 99.999%[178]. The annual hydrogen production capacity of the device is approximately 200 tons, producing green hydrogen through renewable electricity with zero carbon emissions during the production process[178]. The megawatt-level PEM water electrolysis hydrogen production system developed by the Dalian Institute of Chemical Physics of the Chinese Academy of Sciences has achieved full-power operation at the hydrogen utilization station of Anhui Branch of State Grid. According to the on-site tests conducted by experts organized by Anhui Branch of State Grid, the system has a rated hydrogen production capacity of 220 standard cubic meters per hour and a peak hydrogen production capacity of 275 standard cubic meters per hour[179]. The technological breakthrough has been practically deployed in Xinjiang's inaugural integrated energy station, and has subsequently secured an additional procurement contract valued at 80 million CNY[180]. These outcomes demonstrate that China has accomplished comprehensive domestic R & D across the PEMWE technology pathway, attaining a leading position within the sector while concurrently earning substantive market validation.

5.3.2 Critical bottlenecks of RuO_2 catalysts in commercial PEMWE

Despite the remarkable progress in RuO_2-based OER electrocatalysts at the laboratory level, their deployment in commercial PEMWE systems faces a series of interconnected technical bottlenecks that must be critically addressed before industrial adoption can be realized. The following analysis identifies six key barriers, quantifying the gap between current research achievements and industrial requirements.

5.3.2.1 Intrinsic dissolution instability under operating conditions

The fundamental barrier to RuO_2 commercialization is its thermodynamic tendency to undergo overoxidation at anodic potentials above ~ 1.4 V *vs.* RHE, where surface Ru^{4+} is irreversibly oxidized to soluble RuO_4 species, leading to permanent loss of active sites[4]. This dissolution process is exponentially accelerated at the high current densities required for industrial PEMWE operation, where local pH drops and elevated potentials at the catalyst/membrane interface create extreme corrosive conditions. ICP-MS measurements have revealed that commercial RuO_2 can lose > 50% of its Ru content within 20 h of operation at 10 mA cm^{-2} in 0.5 M H_2SO_4, whereas IrO_2 loses < 5% under identical conditions[11]. Even the most advanced modified RuO_2 catalysts have only been demonstrated at current densities of 0.5-1 A cm^{-2} in PEMWE single cells (e.g., Ta-RuO_2 with 2,800 h stability at 14 μV h^{-1}[164]. The dissolution rate at ampere-level current densities remains largely uncharacterized for most reported RuO_2 catalysts, representing a critical knowledge gap.

5.3.2.2 Durability gap relative to industrial lifetime requirements

Commercial PEMWE systems are designed for operational lifetimes exceeding 60,000 h (~ 7 years of continuous operation), with the U.S. DOE ultimately targeting 80,000 h[181]. The best-reported RuO_2-based PEMWE durability is approximately 2,800 h for Ta-RuO_2 at a degradation rate of 14 μV h^{-1}[164]. Even assuming this degradation rate remains constant, an optimistic assumption given the accelerating nature of dissolution-driven degradation, the projected lifetime would be approximately 10,000-20,000 h, still a factor of 3-6x below the commercial requirement. Furthermore, most reported long-term stability tests are conducted under constant current conditions, whereas real-world PEMWE operation under renewable energy coupling involves frequent load cycling and start-up/shutdown transients that can accelerate degradation by 2-5x. This durability gap represents the single most critical barrier to RuO_2 commercialization.

5.3.2.3 Laboratory-to-industry performance translation gap

A pervasive but frequently overlooked issue is the fundamental mismatch between laboratory evaluation protocols and industrial operating conditions. The vast majority of RuO_2 catalyst performance data reported in the literature are measured in three-electrode configurations at current densities of 10 mA cm^{-2} using rotating disk electrodes. In contrast, commercial PEMWE anodes operate at 1-3 A cm^{-2} in MEAs with catalyst loadings of 1-4 mg cm^{-2}, at elevated temperatures and under pressure. The translation from half-cell to MEA performance is nontrivial: mass transport limitations, catalyst/ionomer interfacial effects, and non-uniform current distribution in large-area electrodes can cause the overpotential to increase and the degradation rate to accelerate.

5.3.2.4 Catalyst loading and cost paradox

While Ru is approximately 10x cheaper than Ir on a per-gram basis, the actual cost advantage in PEMWE anodes is significantly diminished by the higher loadings and more frequent replacement required to compensate for RuO_2's faster degradation. Current commercial PEMWE anodes use IrO_2 loadings of 2–4 mg cm^{-2}[182]. If RuO_2 requires 2–3x higher loadings to achieve comparable initial performance and must be replaced 3–6x more frequently over the system lifetime, the effective cost per kWh of hydrogen produced may actually exceed that of IrO_2-based systems. A rigorous techno-economic analysis by Minke *et al.*[22] showed that for PEMWE deployment at the terawatt scale, even with RuO_2 at 1 mg cm^{-2}, the cumulative Ru demand could exceed 50% of annual global production, creating supply chain vulnerabilities analogous to those currently faced by Ir. The cost advantage of RuO_2 is therefore conditional on achieving comparable or superior durability at equivalent or lower loadings, a goal that has not yet been realized.

5.3.2.5 MEA integration and carbon support corrosion challenges

The translation of high-performance RuO_2 catalysts from powder form to functional MEA catalyst layers introduces multiple engineering challenges: (a) Ionomer distribution: Uniform dispersion of Nafion ionomer within the RuO_2 catalyst layer is critical for proton conductivity and reactant/product transport, but the hydrophilic nature of RuO_2 surfaces leads to poor ionomer-catalyst interaction compared to IrO_2, often resulting in non-uniform ionomer distribution and localized flooding or drying; (b) Catalyst layer cracking: RuO_2 nanoparticles tend to agglomerate during ink drying, forming cracks and voids that increase ohmic resistance and create non-uniform current distribution; (c) Carbon support corrosion: Many of the highest-performing RuO_2 catalysts reported employ carbon-based supports (CNTs, carbon cloth, carbon nanosheets) or protective carbon coatings (e.g., NC@Vo-RuO_2/CNTs-350 with 1,000 h stability)[115]. However, carbon is thermodynamically unstable at anodic potentials above ~ 0.9 V *vs.* RHE in acidic media, undergoing electrochemical oxidation to CO_2. While carbon supports may survive short-term laboratory tests at moderate current densities, they will inevitably corrode under industrial PEMWE operating conditions, leading to catalyst detachment, RuO_2 agglomeration, and rapid performance decay. This fundamental incompatibility means that carbon-supported RuO_2 catalysts cannot be directly deployed in commercial PEMWE anodes without replacing the carbon support with a corrosion-resistant alternative, which typically sacrifices electronic conductivity and catalytic activity.

5.3.2.6 Lack of standardized accelerated stress testing protocols

The absence of industry-accepted accelerated stress testing (AST) protocols for RuO_2-based PEMWE anodes makes it impossible to meaningfully compare durability across different studies or to project long-term performance from short-term tests. Current stability assessments vary widely in testing conditions: electrolyte concentration (0.1–0.5 M H_2SO_4 or $HClO_4$), current density (1–100 mA cm^{-2} in half-cells; 0.1–2 A cm^{-2} in MEAs), temperature (25–80 °C), and duration (6–2,800 h). Without standardized AST protocols, such as the potential cycling protocols established for PEM fuel cell catalysts, it is extremely difficult to: (a) rank catalyst stability on a common scale, (b) identify degradation mechanisms under realistic operating conditions, or (c) provide reliable lifetime projections for commercial systems. The development and adoption of such protocols is a prerequisite for translating laboratory RuO_2 innovations into qualified commercial products.

Collectively, these six bottlenecks form an interconnected barrier system: dissolution instability causes the durability gap, which is exacerbated by the lab-to-industry translation gap and MEA integration challenges; the cost paradox means that simply increasing RuO_2 loading to compensate for faster degradation is economically unviable; and the lack of standardized testing prevents reliable benchmarking and qualification. Addressing these bottlenecks requires not only continued materials innovation, but also systematic engineering efforts in MEA design, manufacturing scale-up, and industrial testing protocols, areas that have received far less attention than catalyst synthesis in the current literature.

5.3.3 Cost structure and the path toward RuO_2 commercialization

In the cost structure of PEMWE, the proportion of precious metal catalysts and key materials is particularly significant. This has prompted researchers to actively explore effective cost reduction methods to accelerate the commercialization process of the technology. Currently, the research efforts mainly focus on two areas: the improvement of iridium recovery technology and the development of alternative materials. In terms of iridium recovery, hydrometallurgical processes have become the mainstream choice due to their mature technical and economic advantages. In the field of alternative material research, RuO_2 catalysts have emerged as the most promising candidates due to their high activity. However, it is still in the transitional period from the laboratory stage to the pilot-scale production stage. Within the domain of substitute material investigation, RuO_2-based catalysts have been identified as the most viable alternatives owing to their superior catalytic performance. Nevertheless, the current stage of development is still in a transitional period between laboratory experiments and pilot production, and it is expected to achieve full commercial application.

The application of Ru-based catalysts goes far beyond the OER in PEMWE. Leveraging their core advantages such as high intrinsic activity for OER, mixed electron-proton conductivity, dual-function catalytic potential, and excellent chlorine evolution selectivity, Ru-based catalysts have permeated various energy conversion and storage systems[48,49,183-185].

5.3.4 Gap analysis and remaining challenges for RuO_2-based PEMWE

While the preceding sections have established that RuO_2-based catalysts can achieve exceptional OER activity and significantly improved stability in half-cell configurations, a critical question remains: how close are these catalysts to actual industrial deployment in PEMWE? This section provides a systematic gap analysis between current laboratory achievements and industrial requirements, identifies the remaining challenges, and proposes a roadmap for bridging this gap.

The most significant barrier to industrial deployment of RuO_2-based PEMWE is the durability gap. The best-performing RuO_2-based PEMWE demonstrations to date include the following: AC-MoRuO can operate for ⩾ 2,000 hours at 1.0 A cm^{-2} and 1,000 hours at 1.5 A cm^{-2}. The voltage loss is negligible[77]. The $Cr0.1Sn_{0.1}Ru_{0.8}O_2$ exhibits excellent performance under industrial current density for 1,000 hours, with a low degradation rate, and can be extended to kilowatt-level (hundred ampere) water electrolysis[186]. At a reverse osmosis water flow rate of 1.0 A cm^{-2}, the degradation rate of Co-RuO_2 over a period of 2,000 hours can reach 10.2 μV h^{-1}[187] and GB-rich Ir-doped RuO_2 can last for over 1,500 hours at ampere-level current densities[143]. While these results represent remarkable progress, demonstrating that RuO_2-based catalysts can survive for thousands of hours under industrial current densities, they still fall 27-40x short of the 80,000-hour lifetime target[181]. Furthermore, most of these durability tests are conducted under steady-state conditions at moderate current densities (0.2-1.5 A cm^{-2}), whereas industrial PEMWE operates at 2-3 A cm^{-2} with dynamic load profiles. The degradation rate of the best RuO_2-based PEMWE is approximately 4x higher than the DOE 2026 target, indicating that even the most advanced RuO_2 catalysts have not yet achieved the long-term stability required for commercial deployment.

Current laboratory demonstrations of RuO_2-based PEMWE typically employ anode catalyst loadings of ~ 1-2 mg cm^{-2}, while the DOE 2026 target for total platinum group metal content (both electrodes combined) is 0.5 mg cm^{-2}[181]. Reducing the Ru loading while maintaining performance and durability is essential for cost competitiveness. The cost advantage of Ru over Ir (approximately 8x lower price) provides some buffer; Ru-based catalysts can afford higher loadings than Ir-based ones for the same cost, but this advantage is negated if Ru's much faster dissolution rate necessitates impractically high initial loadings. The synthesis methods used for state-of-the-art RuO_2-based catalysts in academic laboratories are often not directly scalable to industrial production. Key challenges include: (1) synthesis reproducibility and batch-to-batch consistency; (2) dopant uniformity at scale; (3) nanoparticle size and morphology control; (4) catalyst ink formulation, and (5) support material scalability.

Given the current rate of progress, where the best PEMWE durability has improved from ~ 100 h (pre-2022) to ~ 3,000 h (2024-2025), we estimate that achieving 80,000-hour PEMWE durability with RuO_2-based anodes will require 5-10 years of focused development, assuming that the non-linear degradation challenge can be addressed.

6. Conclusions and Perspectives

Designing efficient RuO_2-based electrocatalysts for the hydrogen production field has become a key step for the large-scale application of PEMWE. This paper reviews the research progress of advanced acidic OER electrocatalysts in recent years based on RuO_2-based catalysts with nanostructures in different dimensions, including defect engineering design in each dimension, incorporation of foreign elements, and construction of heterogeneous structures (Figure 17 and Table 4). As the most advanced catalysts for acidic OER, Ru-based materials are explored across multiple dimensions. Current research centers on tailoring their structural morphology and electronic structure to break the activity-stability trade-off.

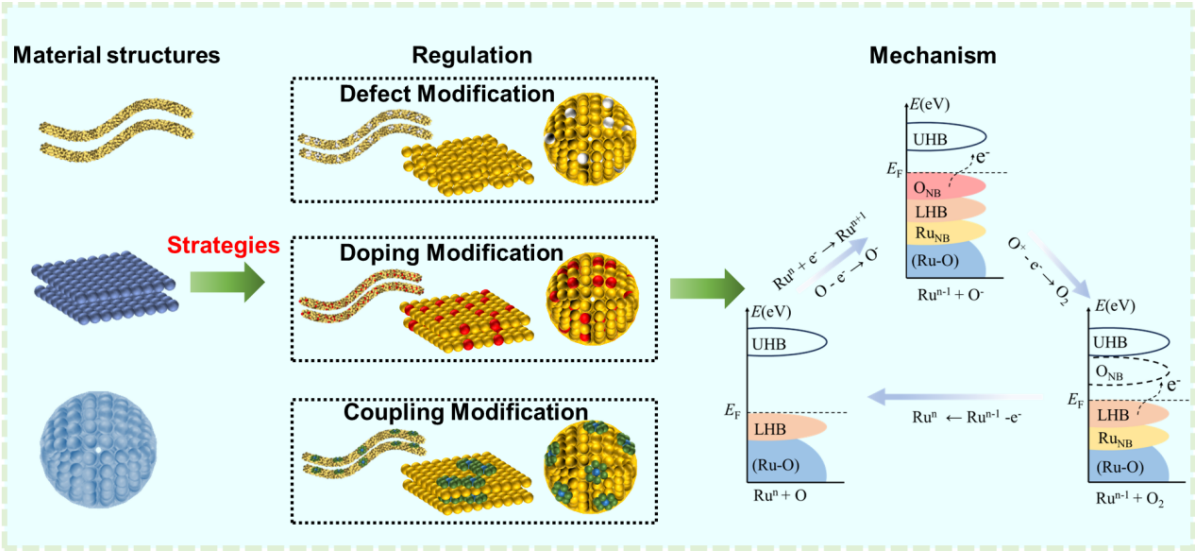


Figure 17. Nanotopography control and optimization strategies of RuO_2-based electrocatalysts. Ru: ruthenium.

Table 4. Summary of the optimization strategies for 1D, 2D, and 3D RuO_2-based electrocatalysts and their OER performances.

	Electrocatalyst	Overpotential (mV) at 10 mA cm^{-2}	Tafel slope (mV dec^{-1})	Stability	Electrolyte	Ref.
1D	**Defect**					
	RuO_2 wavy NWs	234	/	20 h at 10 mA cm^{-2}	0.5 M H_2SO_4	[112]
	V-$Ru_xMn_{1-x}O_2$ NWs	200	48.97	600 h at 10 mA cm^{-2}	0.5 M H_2SO_4	[113]
	Doping					
	M-doped RuO_2 NWs, M = Fe/Co/Ni	200	/	/	0.5 M H_2SO_4	[117]
	Zn-doped RuO_2 nanowires	173	41.2	1,000 h at 10 mA cm^{-2}	0.5 M H_2SO_4	[158]
	Co-Doped Nanorod-like RuO_2	169	49	50 h at 10 mA cm^{-2}	0.5 M H_2SO_4	[62]
	Mn-RuO_2 oxide nanowires	168	42.97	40 mV after 150 h @ 10 mA cm^{-2}	0.5 M H_2SO_4	[118]
	Te-doped RuO_2 nanotubes	171	38.1	50 h at 10 mA cm^{-2}	0.1 M $HClO_4$	[119]
	SH-RuCuO NRs	231	39.7	250 h at 10 mA cm^{-2}	0.5 M H_2SO_4	[188]
	$Ir_xRu_{1-x}O_2$($Ir_{0.91}Ru_{0.09}O_2$)	180	50.3	0.34% after 72 h @ 10 mA cm^{-2}	0.5 M H_2SO_4	[189]
	Co-doped RuO_2 nanorod	328	74	24 h at 10 mA cm^{-2}	0.5 M H_2SO_4	[120]
	nanorod-shaped PtCo-RuO_2/C	212.6	48.5	100 h at 10 mA cm^{-2}	0.1 M $HClO_4$	[60]
	Coupling					
	IrO_2-RuO_2/C	188	42	6 h at 10 mA cm^{-2}	0.5 M H_2SO_4	[129]
	RuO_2/MoO_3 nanowires	167	65	30 h at 10 mA cm^{-2}	0.5 M H_2SO_4	[96]
	WO_3@RuO_2 heterostructure nanowires	246	68.3	50 h at 10 mA cm^{-2}	0.5 M H_2SO_4	[190]
	Other					
	Ru/RuO_2 NB/C	276	69	/	0.5 M H_2SO_4	[138]
2D	**Defect**					
	defect-rich ultra-thin RuO_2 nanosheets	199	38.2	32 mV after 6 h @ 10 mA cm^{-2}	0.5 M H_2SO_4	[102]
	GB-RuO_2	187	34.5	550 h at 10 mA cm^{-2}	0.1 M $HClO_4$	[57]
	defective RuO_2-NS/CF	212	73	30 h at 10 mA cm^{-2}	0.5 M H_2SO_4	[191]
	Doping					
	Rh-RuO_2/G nanosheets	161	45.8	700 h at 50 mA cm^{-2}	0.5 M H_2SO_4	[95]
	Cox-doped RuO_2 nanosheets(x = 0.108)	214	78	45 h at 10 mA cm^{-2}	0.5 M H_2SO_4	[192]
	Pd-doped RuO_2 nanosheet	204	51.7	7,000 s at 10 mA cm^{-2}	0.5 M H_2SO_4	[42]
	2D Mn/RuO_2 nanosheets	185	45.05	3% after 25 h @ 10 mA cm^{-2}	0.5 M H_2SO_4	[193]
	Ru/S NSs-400	219	46.1	600 h at 10 mA cm^{-2}	0.5 M H_2SO_4	[122]
	5% Pt-Ru ONAs	227	38.2	6 h at 10 mA cm^{-2}	0.5 M H_2SO_4	[194]
	Coupling					
	$RuCoO_x$ nanosheet catalyst	200	50.1	45 mV after 100 h at 10 mA cm^{-2}	0.1 M $HClO_4$	[59]
	RuO_2/$CoMnO_3$ nanosheet	210	71.6	500 h at 10 mA cm^{-2}	0.5 M H_2SO_4	[92]
	Other					

	2D D-RuO_2/G	169	40	/	0.5 M H_2SO_4 [195]
	MnO_x/RuO_2	178	43.8	40 h at 10 mA cm^{-2}	0.5 M H_2SO_4 [196]
	a/c-RuO_2/CC	150	47	24 h at 10 mA cm^{-2}	0.5 M H_2SO_4 [141]
	Mn-RuO_2 nanoarrays	217	54.46	100 h at 10 mA cm^{-2}	0.5 M H_2SO_4 [197]
3D	**Defect**				
	oxygen vacancies of RuO_2-PTFE	219	62	800 h at 10 mA cm^{-2}	[198]
	ultrafine defective RuO_2 nanoparticles	179	36.9	19 mV after 20 h @ 10 mA cm^{-2}	0.5 M H_2SO_4 [116]
	NC@Vo•-RuO_2/CNTs-350	170	/	/	0.5 M H_2SO_4 [115]
	Doping				
	$La_{0.1}Ru_{0.9}O_2$	188	76.6	180 mV after 63 h at 10 mA cm^{-2}	0.5 M H_2SO_4 [128]
	$Ru_3Cr_1Sr_x$(x = 0.125,0.175,0.225)	214	39.8	300 h at 10 mA cm^{-2}	0.1 M $HClO_4$ [125]
	Pt-doped RuO_2 hollow nanospheres	228	51	100 h at 100 mA cm^{-2}	0.5 M H_2SO_4 [127]
	$Sn_{0.1}$-RuO_2@NCP	178	60.6	150 h at 10 mA cm^{-2}	0.5 M H_2SO_4 [124]
	Cu-doped RuO_2 hollow porous polyhedra	188	43.96	8 h at 10 mA cm^{-2}	0.5 M H_2SO_4 [126]
	Coupling				
	Ru/RuO_2	183	45	0.11 mV h^{-1} in 600h @ 10 mA cm^{-2}	0.5 M H_2SO_4 [199]
	Ru-RuO_2 heterostructures	176	61	62 mV after 80 h at 10 mA cm^{-2}	0.5 M H_2SO_4 [134]
	RuO_2-CeO_2-CC heterostructures	180	58.9	1,000 h at 10 mA cm^{-2}	0.5 M H_2SO_4 [135]
	Ru/RuO_2-Co_3O_4(Vo)	226	49	19 h at 10 mA cm^{-2}	0.1 M $HClO_4$ [200]
	Acid-Treated RuO_2/Co_3O_4	152	83	150 h at 10 mA cm^{-2}	0.5 M H_2SO_4 [136]
	RuO_2/CeO_2@C	170	56.6	100 h at 50 mA cm^{-2}	0.5 M H_2SO_4 [201]
	Pt-RuO_2@KB	272	61.9	12 h at 1.465 V *vs*. RHE	0.1 M $HClO_4$ [202]
	RuO_2/$MnO_{2-\gamma}$	220	72.2	80 h at 50 mA cm^{-2}	0.1 M $HClO_4$ [133]
	Other				
	C-RuO_2-RuSe-10	212	50.4	50 h at 10 mA cm^{-2}	0.5 M H_2SO_4 [91]
	$Ru_{0.6}W_{17.4}O_{49-\delta}$	252	50	45 h at 10 mA cm^{-2}	0.1 M $HClO_4$ [203]
	$RuS_{0.45}O_x$	160	39.18	1,000 h at 10 mA cm^{-2}	0.5 M H_2SO_4 [78]

1D: one-dimensional; 2D: two-dimensional; 3D: three-dimensional; Ru: ruthenium; NWs: nanowires; NSs: nanosheets; $Sn_{0.1}$-RuO_2@NCP: Sn-RuO_2 nanoparticles supported on N-doped carbon polyhedra; RHE: reversible hydrogen electrode.

Despite significant progress in the study of RuO_2-based electrocatalysts, several critical challenges remain unresolved, and the path toward industrial PEMWE deployment requires targeted, operable research strategies. Below, we outline five specific research proposals with defined methodologies, expected outcomes, and quantitative targets.

6.1 Machine learning-assisted dopant screening for breaking the activity-stability trade-off

The current trial-and-error approach to dopant selection is inefficient, given the vast compositional space of single-element ($\geqslant$ 30 candidates across transition metals, rare earths, and main-group elements) and co-doping (combinatorial explosion of binary/ternary pairs) configurations. We propose a three-stage machine learning (ML) workflow specifically tailored for RuO_2-based OER electrocatalysts:

Stage 1: Descriptor Construction and Database Assembly: Establish a high-fidelity dataset by extracting structural descriptors (d-band center, Ru-O covalency index, O 2p band center position, formation energy of oxygen vacancies, *OH/*O/*OOH adsorption energies) from DFT calculations on doped RuO_2 surfaces. Augment this with experimental performance metrics (overpotential, Tafel slope, stability hours) from published literature to create a dual-source training database. Key descriptors should include the Pourbaix

stability criterion as recently demonstrated by Abed *et al*. who used a Pourbaix ML framework to identify Ti-doped RuO_2 with suppressed Ru dissolution[204].

Stage 2: Multi-Objective ML Model Training: Deploy ensemble learning algorithms (e.g., gradient boosting, random forest) and deep learning models (graph neural networks for crystal structure representation) trained simultaneously on activity (η_{10} minimization) and stability (Ru dissolution rate minimization) objectives. The model should incorporate a Pareto optimization module to identify dopant combinations that lie on the activity-stability Pareto frontier, rather than optimizing either metric in isolation. Recent work by Shang *et al*. demonstrated a general machine-learning framework for high-throughput screening of stable and efficient RuO_2-based OER catalysts, achieving high consistency between ML predictions and experimental validation for Co-, Cu-, Zn-doped RuO_2[205].

Stage 3: High-Throughput Computational Validation and Experimental Verification: Screen the top 20-50 ML-predicted dopant candidates using automated DFT workflows (e.g., AFLOW, Materials Project APIs), then synthesize and test the top 5-10 candidates experimentally. The target is to determine the appropriate doping combinations within 3 to 5 years, so that they can achieve a lower overpotential at high current density, and can operate stably in the PEMWE for a long time.

6.2 Multi-scale simulation prediction of Ru dissolution behavior under operating conditions

Ru dissolution is the fundamental failure mechanism of RuO_2-based catalysts in acidic OER, yet current understanding relies primarily on post-mortem analysis rather than predictive modeling. We propose a hierarchical multi-scale simulation framework:

(a) Quantum Scale (0-1 nm): Employ ab initio molecular dynamics (AIMD) and constrained DFT to calculate the thermodynamic and kinetic barriers for Ru oxidation pathways ($Ru^{4+} \rightarrow Ru^{n+}$, $n > 4$) and RuO_4 formation/desorption on different doped/defected RuO_2 surfaces. Key outputs include the dissolution onset potential and the activation energy for Ru-O bond breaking under applied potential, as informed by the computational hydrogen electrode (CHE) model.

(b) Mesoscale (1-100 nm): Develop kinetic Monte Carlo (kMC) models parameterized by AIMD-derived rate constants to simulate the temporal evolution of surface Ru site populations, oxygen vacancy accumulation, and lattice oxygen depletion under OER operating conditions. This enables prediction of catalyst lifetime as a function of operating current density, temperature, and local pH.

(c) Macroscale (100 nm-mm): Integrate kMC-derived degradation rates into continuum-level PEMWE cell models (e.g., using COMSOL Multiphysics) that couple electrochemical reaction kinetics, species transport, and catalyst layer degradation. This enables prediction of cell-level voltage degradation rates as a function of catalyst composition and operating conditions, directly comparable to industrial durability metrics.

(d) Validation Protocol: Cross-validate simulation predictions against operando synchrotron XAS data monitoring Ru oxidation state evolution, and ICP-MS quantifying dissolved Ru concentrations in the electrolyte. The target is to achieve predictive accuracy within 20% of experimentally measured dissolution rates and to establish a "dissolution phase diagram" mapping Ru stability as a function of dopant type, concentration, and operating potential.

6.3 Roll-to-roll large-area catalyst coating technology for PEMWE scale-up

The transition from laboratory-scale catalyst fabrication (typically < 5 cm^2 electrode area) to industrial PEMWE deployment (active areas > 1,000 cm^2) represents a critical manufacturing bottleneck. Current laboratory methods (drop-casting, spin-coating, hand-brushing) produce catalyst layers with non-uniform thickness, poor reproducibility, and low throughput. We propose the development of roll-to-roll (R2R) coating technology specifically adapted for RuO_2-based anode catalyst layers:

(a) Ink formulation optimization: Develop stable, high-solid-content RuO_2 catalyst inks with controlled rheological properties suitable for slot-die coating. The ink must incorporate optimized ionomer-to-catalyst ratios (typically 15-30 wt% Nafion) and dispersant systems that prevent RuO_2 nanoparticle aggregation while maintaining electrochemical accessibility.

(b) CCM *vs*. CCS strategy: Evaluate both CCM (direct coating on Nafion membrane) and CCS (coating on porous transport layer) architectures for RuO_2-based anodes. CCM offers lower interfacial resistance but requires careful control of membrane swelling during coating; CCS enables decoupled optimization of catalyst layer and membrane but may introduce additional contact resistance. The goal is to achieve in single-cell testing of PEMWE, the MEA prepared by the R2R process using RuO_2 anode can achieve a higher current density response under low voltage conditions, and maintain a low attenuation rate within a long-term stability period[206].

(c) Scalability and cost analysis: Conduct techno-economic analysis comparing R2R-coated RuO_2 anodes with conventional IrO_2 anodes on a per-kW basis. Given Ru's ~ 50× lower cost than Ir, even with comparable loadings, the raw material cost reduction potential exceeds $150/kW at current metal prices.

6.4 *In Situ* /operando characterization of LOM-to-AEM pathway switching dynamics

The transition between LOM and AEM pathways during OER operation fundamentally determines both activity and stability, yet the

real-time dynamics of this switching remain poorly understood. We propose a combined operando characterization protocol:

(a) Employ operando DEMS with ^{18}O isotope labeling to track lattice oxygen participation in real time, combined with operando Raman spectroscopy monitoring the Ru-O stretching mode evolution.

(b) Correlate these observations with operando XAS at the Ru K-edge (monitoring Ru oxidation state) and O K-edge (monitoring O 2p band occupancy) to establish a mechanistic map linking electronic structure evolution to reaction pathway selection.

(c) The target is to identify the critical potential threshold and structural conditions (oxygen vacancy concentration, Ru oxidation state, d-band center position) at which LOM-to-AEM switching occurs, enabling rational design of catalysts that maintain AEM dominance under industrial operating conditions.

6.5 Accelerated stress testing protocols for industrial qualification

Current stability assessments (chronopotentiometry at 10 mA cm^{-2} for tens to hundreds of hours) do not reflect industrial PEMWE operating conditions. We propose standardized AST protocols:

(a) Potential cycling AST: apply 10,000 cycles between 1.0-1.6 V *vs.* RHE at 50 mV s^{-1} in 0.5 M H_2SO_4 to simulate start-up/shutdown transients, followed by ICP-MS quantification of dissolved Ru.

(b) High-current-density hold AST: maintain 1-2 A cm^{-2} in a PEMWE single cell at 80 °C for 1,000 h, with periodic polarization curve recording every 100 h to track voltage degradation rate.

(c) Combined AST: alternate between high-current holds and open-circuit periods for 500 cycles to simulate renewable energy-coupled operation with power fluctuations.

(d) Establish quantitative degradation benchmark: after the catalyst completes the entire AST protocol, it should exhibit a lower degradation rate and Ru loss (measured by ICP-MS) before it can be considered for industrial application.

In summary, the industrial deployment of RuO_2-based OER electrocatalysts in PEMWE systems requires a paradigm shift from empirical optimization to predictive, data-driven catalyst design, physics-informed durability modeling, and manufacturing-scalable fabrication, supported by mechanistic understanding under realistic operating conditions and rigorous industrial qualification standards. These five proposals are interconnected: ML-identified optimal dopants serve as inputs for dissolution modeling and operando characterization; validated catalyst formulations are then scaled via R2R coating and qualified through standardized AST protocol. This integrated research framework provides a concrete roadmap for transitioning RuO_2-based electrocatalysts from laboratory discoveries to commercially viable PEMWE anodes, ultimately contributing to the U.S. DOE's target of $1/kg green hydrogen by 2030.

Declarations

Acknowledgements

No artificial intelligence (AI) tools or language models were used in the writing, editing, or revision of this manuscript.

Authors contribution

Feng WJ: Writing-original draft, conceptualization.
Wang X: Investigation, resources.
Wang LX, Yang H: Investigation.
Yuan CZ: Writing-review & editing, investigation, supervision.
Zhang X: Writing-review & editing, investigation, funding acquisition, supervision.
Wang R: Investigation, funding acquisition, supervision.

Conflicts of interest

The authors declare no conflicts of interest.

Ethical approval

Not applicable.

Consent to participate

Not applicable.

Consent for publication

Not applicable.

Availability of data and materials

Not applicable.

Funding

This work was supported by the Double Thousand Plan of Jiangxi Province (Grant No. jxsq2023201002); the Joint Fund Project of University of Science and Technology of China-Ganjiang Innovation Academy-Chinese Academy of Sciences-China Rare Earth Group Co., Ltd. -Ganzhou Municipal Government-"Challenge-Based" Project (Grant No. FU2025J006).

Copyright

© The Author(s) 2026.

References

1. Zhao JW, Li Y, Luan D, Lou XWD. Structural evolution and catalytic mechanisms of perovskite oxides in electrocatalysis. Sci Adv. 2024;10(39):eadq4696. [DOI][PubMed][PMC]
2. Li L, Wang P, Shao Q, Huang X. Metallic nanostructures with low dimensionality for electrochemical water splitting. Chem Soc Rev. 2020;49(10):3072-3106. [DOI][PubMed]
3. Chu S, Majumdar A. Opportunities and challenges for a sustainable energy future. Nature. 2012;488(7411):294-303. [DOI][PubMed]
4. Bai J, Zhou W, Xu J, Zhou P, Deng Y, Xiang M, et al. RuO_2 catalysts for electrocatalytic oxygen evolution in acidic media: Mechanism, activity promotion strategy and research progress. Molecules. 2024;29(2):537. [DOI][PubMed][PMC]
5. Chen D, Liu T, Wang P, Zhao J, Zhang C, Cheng R, et al. Ionothermal route to phase-pure RuB_2 catalysts for efficient oxygen evolution and water splitting in acidic media. ACS Energy Lett. 2020;5(9):2909-2915. [DOI]
6. Sun M, Huang H, Niu X, Gong S, Li Z, Fang J, et al. Grain boundary-derived local amorphization enhances acidic OER. ACS Catal. 2024;14(20):15764-15776. [DOI]
7. Marquez RA, Kalokowski E, Espinosa M, Bender JT, Son YJ, Kawashima K, et al. Transition metal incorporation: Electrochemical, structure, and chemical composition effects on nickel oxyhydroxide oxygen-evolution electrocatalysts. Energy Environ Sci. 2024;17(5):2028-2045. [DOI]
8. Gielen D, Boshell F, Saygin D, Bazilian MD, Wagner N, Gorini R. The role of renewable energy in the global energy transformation. Energy Strategy Rev. 2019;24:38-50. [DOI]
9. Suntivich J, May KJ, Gasteiger HA, Goodenough JB, Shao-Horn Y. A perovskite oxide optimized for oxygen evolution catalysis from molecular orbital principles. Science. 2011;334(6061):1383-1385. [DOI][PubMed]
10. Song F, Bai L, Moysiadou A, Lee S, Hu C, Liardet L, et al. Transition metal oxides as electrocatalysts for the oxygen evolution reaction in alkaline solutions: An application-inspired renaissance. J Am Chem Soc. 2018;140(25):7748-7759. [DOI][PubMed]
11. Cherevko S, Geiger S, Kasian O, Kulyk N, Grote JP, Savan A, et al. Oxygen and hydrogen evolution reactions on Ru, RuO_2, Ir, and IrO_2 thin film electrodes in acidic and alkaline electrolytes: A comparative study on activity and stability. Catal Today. 2016;262:170-180. [DOI]
12. Vereshchuk N, Gil-Sepulcre M, Ghaderian A, Holub J, Gimbert-Suriñach C, Llobet A. Metamorphic oxygen-evolving molecular Ru and Ir catalysts. Chem Soc Rev. 2023;52(1):196-211. [DOI]
13. Qin Y, Yu T, Deng S, Zhou XY, Lin D, Zhang Q, et al. RuO_2 electronic structure and lattice strain dual engineering for enhanced acidic oxygen evolution reaction performance. Nat Commun. 2022;13(1):3784. [DOI]
14. Lin X, Liu P, Zheng J, Xu J, Wang Z, Chen Z, et al. Electronic tuning of RuO_2 polarizes metal-oxygen redox for proton exchange membrane water electrolysis. Nat Commun. 2025;16(1):8709. [DOI][PubMed][PMC]
15. Huang Y, Zhou T, Hu Y, Yang Y, Yang F, Huang W, et al. Ordered derivatives on Ti surface enhance the OER activity and stability of Ru-based film electrode. Int J Hydrogen Energy. 2023;48(86):33411-33421. [DOI]
16. Suen NT, Hung SF, Quan Q, Zhang N, Xu YJ, Chen HM. Electrocatalysis for the oxygen evolution reaction: Recent development and future perspectives. Chem Soc Rev. 2017;46(2):337-365. [DOI]
17. Hou L, Gu X, Cui X, Tang J, Li Z, Liu X, et al. Strategies for the design of ruthenium-based electrocatalysts toward acidic oxygen evolution reaction. EES Catal. 2023;1(5):619-644. [DOI]
18. An L, Wei C, Lu M, Liu H, Chen Y, Scherer GG, et al. Recent development of oxygen evolution electrocatalysts in acidic environment. Adv Mater. 2021;33(20):e2006328. [DOI][PubMed]
19. Chen Y, Liu C, Xu J, Xia C, Wang P, Xia BY, et al. Key components and design strategy for a proton exchange membrane water electrolyzer. Small Struct. 2023;4(6):2200130. [DOI]
20. Wu ZY, Chen FY, Li B, Yu SW, Finfrock YZ, Meira DM, et al. Non-iridium-based electrocatalyst for durable acidic oxygen evolution reaction in proton exchange membrane water electrolysis. Nat Mater. 2023;22(1):100-108. [DOI]
21. Song HJ, Yoon H, Ju B, Kim DW. Highly efficient perovskite-based electrocatalysts for water oxidation in acidic environments: A mini

review. Adv Energy Mater. 2021;11(27):2002428. [DOI]
22. Minke C, Suermann M, Bensmann B, Hanke-Rauschenbach R. Is iridium demand a potential bottleneck in the realization of large-scale PEM water electrolysis? Int J Hydrogen Energy. 2021;46(46):23581-23590. [DOI]
23. Qiu C, Sellers C, Wu ZY, Cullen DA, Stavitski E, Tayal A, et al. Low-iridium stabilized ruthenium oxide anode catalyst for durable proton-exchange membrane water electrolysis. Nat Nanotechnol. 2025;20(12):1787-1795. [DOI]
24. Qin R, Chen G, Feng X, Weng J, Han Y. Ru/Ir-based electrocatalysts for oxygen evolution reaction in acidic conditions: From mechanisms, optimizations to challenges. Adv Sci. 2024;11(21):2309364. [DOI]
25. Chen Z, Guo L, Pan L, Yan T, He Z, Li Y, et al. Advances in oxygen evolution electrocatalysts for proton exchange membrane water electrolyzers. Adv Energy Mater. 2022;12(14):2103670. [DOI]
26. Tang L, Chen X, Xie Z, Xiang Q, Liu J, Li L, et al. Metal-oxygen bonding characteristics dictate activity and stability differences of RuO_2 and IrO_2 in the acidic oxygen evolution reaction. Phys Chem Chem Phys. 2025;27(18):9369-9378. [DOI][PubMed]
27. Zhou C, Li L, Dong Z, Lv F, Guo H, Wang K, et al. Pinning effect of lattice Pb suppressing lattice oxygen reactivity of Pb-RuO_2 enables stable industrial-level electrolysis. Nat Commun. 2024;15(1):9774. [DOI][PubMed][PMC]
28. Geiger S, Kasian O, Ledendecker M, Pizzutilo E, Mingers AM, Fu WT, et al. The stability number as a metric for electrocatalyst stability benchmarking. Nat Catal. 2018;1(7):508-515. [DOI]
29. Wu Q, Zhou R, Yao Z, Wang T, Li Q. Effective approaches for enhancing the stability of ruthenium-based electrocatalysts towards acidic oxygen evolution reaction. Chin Chem Lett. 2024;35(10):109416. [DOI]
30. Ping X, Liu Y, Zheng L, Song Y, Guo L, Chen S, et al. Locking the lattice oxygen in RuO_2 to stabilize highly active Ru sites in acidic water oxidation. Nat Commun. 2024;15(1):2501. [DOI][PubMed][PMC]
31. Wen Y, Chen P, Wang L, Li S, Wang Z, Abed J, et al. Stabilizing highly active Ru sites by suppressing lattice oxygen participation in acidic water oxidation. J Am Chem Soc. 2021;143(17):6482-6490. [DOI][PubMed]
32. Chen X, Huang C, Liu J, Xiang Q, Zhang L, Huang X, et al. Dynamic stability of OER electrocatalysts in water electrolyzers: Multiscale deactivation mechanisms and regulation strategies. Chem Sci. 2026;17(29):14120-14151. [DOI][PubMed][PMC]
33. Lao K, Lin H, Wen L, Huang F, Tao H, Zheng N. Revealing ionomer loss from the anode catalyst layer as a critical degradation origin in water electrolysis. Adv Funct Mater. 2026:e77598. [DOI]
34. Xu S, Liu H, Zheng N, Tao HB. Physical degradation of anode catalyst layer in proton exchange membrane water electrolysis. Adv Mater Interfaces. 2025;12(4):2400549. [DOI]
35. Hao S, Zhu P, Wang H. Failure mechanisms in PEM water electrolyzers. Carbon Future. 2025;2(4):9200060. [DOI]
36. Mo J, Kang Z, Yang G, Li Y, Retterer ST, Cullen DA, et al. *In situ* investigation on ultrafast oxygen evolution reactions of water splitting in proton exchange membrane electrolyzer cells. J Mater Chem A. 2017;5(35):18469-18475. [DOI]
37. Wang C, Jin L, Shang H, Xu H, Shiraishi Y, Du Y. Advances in engineering RuO_2 electrocatalysts towards oxygen evolution reaction. Chin Chem Lett. 2021;32(7):2108-2116. [DOI]
38. Zhang Q, Qian Z, Wei Y, Liu X, Zhang P, Gao Y, et al. Molten salt-derived RuO_2 nanocrystals and nanowires: Unveiling correlations of morphology, microstructure, and electrocatalytic performance. Inorg Chem. 2023;62(44):18257-18266. [DOI]
39. Liu Y, Duan T, Xu L, Gao X, Xue L, Xin Y, et al. Electrocatalyst of RuO_2 decorating TiO_2 nanowire arrays for acidic oxygen evolution. Int J Hydrogen Energy. 2023;48(29):10737-10754. [DOI]
40. Wang Y, Hao Y, Wang L, Li C, Ren J, Sun Y, et al. Charge-enriched RuO_2 nanoparticles decorating TiO_2 with Ti defects to promote oxygen evolution reaction in acidic media. Inorg Chem Front. 2023;10(20):6015-6022. [DOI]
41. Yan Y, Xia BY, Zhao B, Wang X. A review on noble-metal-free bifunctional heterogeneous catalysts for overall electrochemical water splitting. J Mater Chem A. 2016;4(45):17587-17603. [DOI]
42. Liu Y, Hu X, Liu C, Zhu S, Jiang K, Liu F, et al. Construction of Pd-doped RuO_2 nanosheets for efficient and stable acidic water oxidation. Green Energy Environ. 2024;9(6):937-948. [DOI]
43. Ju Z, Kong X. Metastable fcc-Ru/fcc-RuO_2 heterointerphase for hydrogen evolution. Inorg Chem. 2025;64(3):1241-1245. [DOI]
44. Zhang L, Gao W, Liu Z, Luo M, Chen Y, Zhang W, et al. Template-assisted construction of molybdenum-doped ruthenium dioxide hollow nanospheres for highly efficient acidic oxygen evolution reaction. Chem Eng Sci. 2025;308:121389. [DOI]
45. Zhao Y, Adiyeri Saseendran DP, Huang C, Triana CA, Marks WR, Chen H, et al. Oxygen evolution/reduction reaction catalysts: From *In situ* monitoring and reaction mechanisms to rational design. Chem Rev. 2023;123(9):6257-6358. [DOI]
46. Li CH, Yuan CZ, Wang LX, Wu F, Xin L, Zhang X, et al. Single atom-decorated transition metal oxide nanomaterials for efficient oxygen evolution reaction. Mater Chem Front. 2024;8(15):2627-2648. [DOI]
47. Jung S, Sung MC, Ju B, Yoon H, Park Y, Kim DW. Phase-guided assembly of RuO_2 epitaxial films on TiO_2 nanofibers: Interfacial coherence outperforming defect-driven mismatch for active site generation in Li-O_2 batteries. Adv Funct Mater. 2026;36(27):e24403. [DOI]
48. Song RY, Park JH, Sivakkumar SR, Kim SH, Ko JM, Park DY, et al. Supercapacitive properties of polyaniline/Nafion/hydrous RuO_2 composite electrodes. J Power Sources. 2007;166(1):297-301. [DOI]
49. Profeti LPR, Profeti D, Olivi P. Pt-RuO_2 electrodes prepared by thermal decomposition of polymeric precursors as catalysts for direct methanol fuel cell applications. Int J Hydrogen Energy. 2009;34(6):2747-2757. [DOI]
50. Liu Y, Wang Y, Li H, Kim MG, Duan Z, Talat K, et al. Effectiveness of strain and dopants on breaking the activity-stability trade-off of RuO_2 acidic oxygen evolution electrocatalysts. Nat Commun. 2025;16(1):1717. [DOI][PubMed][PMC]
51. Danilovic N, Subbaraman R, Chang KC, Chang SH, Kang YJ, Snyder J, et al. Activity-stability trends for the oxygen evolution reaction on

monometallic oxides in acidic environments. J Phys Chem Lett. 2014;5(14):2474-2478. [DOI][PubMed]
52. Yu Y, Liu F, Liu X, Li L, Zhou B, Liao H, et al. Suppressive Ru oxidation and activated lattice oxygen in Mn doped RuO_2 for efficient acidic oxygen evolution reaction. Chem Eng J. 2025;514:163295. [DOI]
53. Hua D, Xu Y, Huang J, Han J, Fu Q, Wei H, et al. Triggering the direct oxygen coupling at the Au/RuO_2 heterointerface to enhance the oxygen evolution reaction in acid. Small. 2025;21(40):e07400. [DOI]
54. KC BR, Kumar D, Bastakoti BP. Enhancing electrocatalytic performance of RuO_2-based catalysts: Mechanistic insights, strategic approaches, and recent advances. JPhys Energy. 2025;7(2):022001. [DOI]
55. Ju C, Wang Y, Liu X, Xie Z, He S, Hu L, et al. Pyrochlore-type $Bi_2Ru_2O_7$ with regulated local electronic structure for efficient oxygen evolution reaction. Small. 2026;22(18):e11136. [DOI][PubMed]
56. Jia R, Tan Y, Li A, Wang Y, Cheng C. 3D ordered RuO_2/WO_3 heterostructure inverse opal arrays for highly-active and stable acidic oxygen evolution reaction. Nano Res Energy. 2025;4(1):e9120141. [DOI]
57. He W, Tan X, Guo Y, Xiao Y, Cui H, Wang C. Grain-boundary-rich RuO_2 porous nanosheet for efficient and stable acidic water oxidation. Angew Chem Int Ed. 2024;63(28):e202405798. [DOI]
58. Huang YC, Wu Y, Lu YR, Chen JL, Lin HJ, Chen CT, et al. Direct identification of O-O bond formation through three-step oxidation during water splitting by operando soft X-ray absorption spectroscopy. Adv Sci. 2024;11(40):e2401236. [DOI][PubMed][PMC]
59. Zhu W, Yao F, Cheng K, Zhao M, Yang CJ, Dong CL, et al. Direct dioxygen radical coupling driven by octahedral ruthenium-oxygen-cobalt collaborative coordination for acidic oxygen evolution reaction. J Am Chem Soc. 2023;145(32):17995-18006. [DOI][PubMed]
60. Jin H, Choi S, Bang GJ, Kwon T, Kim HS, Lee SJ, et al. Safeguarding the RuO_2 phase against lattice oxygen oxidation during acidic water electrooxidation. Energy Environ Sci. 2022;15(3):1119-1130. [DOI]
61. Chen S, Huang H, Jiang P, Yang K, Diao J, Gong S, et al. Mn-doped RuO_2 nanocrystals as highly active electrocatalysts for enhanced oxygen evolution in acidic media. ACS Catal. 2020;10(2):1152-1160. [DOI]
62. Tian Y, Wang S, Velasco E, Yang Y, Cao L, Zhang L, et al. A Co-doped nanorod-like RuO_2 electrocatalyst with abundant oxygen vacancies for acidic water oxidation. iScience. 2020;23(1):100756. [DOI][PubMed][PMC]
63. Ma G, Huo H, Hu Y, Liu J, Liu Z, Ding Y, et al. Engineering acid-stable OER electrocatalysts: Recent advances in main-group element doping of ir- and Ru-based oxides. ACS Catal. 2026;16(3):1871-1893. [DOI]
64. Tan X, Zhang M, Chen D, Li W, Gou W, Qu Y, et al. Electrochemical etching switches electrocatalytic oxygen evolution pathway of IrO_X/Y_2O_3 from adsorbate evolution mechanism to lattice-oxygen-mediated mechanism. Small. 2023;19(44):e2303249. [DOI][PubMed]
65. Wu J, Zou W, Zhang J, Zhang L, Song H, Cui Z, et al. Regulating Ir-O covalency to boost acidic oxygen evolution reaction. Small. 2024;20(22):e2308419. [DOI][PubMed]
66. Qian F, Cao D, Chen S, Yuan Y, Chen K, Chimtali PJ, et al. High-entropy RuO_2 catalyst with dual-site oxide path for durable acidic oxygen evolution reaction. Nat Commun. 2025;16(1):6894. [DOI]
67. Lin C, Li JL, Li X, Yang S, Luo W, Zhang Y, et al. *In-situ* reconstructed Ru atom array on α-MnO_2 with enhanced performance for acidic water oxidation. Nat Catal. 2021;4(12):1012-1023. [DOI]
68. Yang M, Guo P, Wu H, Han X, Cheng Y, Xiao M, et al. Engineering a dynamic oxygen vacancy activation-replenishment-regeneration cycle in Mo-doped RuO_2 for efficient and durable acidic water oxidation. Energy Environ Sci. 2026;19(15):5027-5037. [DOI]
69. Nong HN, Falling LJ, Bergmann A, Klingenhof M, Tran HP, Spöri C, et al. Key role of chemistry versus bias in electrocatalytic oxygen evolution. Nature. 2020;587(7834):408-413. [DOI][PubMed]
70. Rao RR, Kolb MJ, Halck NB, Pedersen AF, Mehta A, You H, et al. Towards identifying the active sites on RuO_2 (110) in catalyzing oxygen evolution. Energy Environ Sci. 2017;10(12):2626-2637. [DOI]
71. Yin ZH, Liu H, Hu JS, Wang JJ. The breakthrough of oxide pathway mechanism in stability and scaling relationship for water oxidation. Natl Sci Rev. 2024;11(11):nwae362. [DOI]
72. Rong C, Meyer Q, Lu H, Zhao C. Bridging laboratory catalysts with industrial proton exchange membrane water electrolyzers. Adv Mater. 2026;38(4):e12414. [DOI]
73. Hong WT, Stoerzinger KA, Lee YL, Giordano L, Grimaud A, Johnson AM, et al. Charge-transfer-energy-dependent oxygen evolution reaction mechanisms for perovskite oxides. Energy Environ Sci. 2017;10(10):2190-2200. [DOI]
74. Wang Q, Cheng Y, Tao HB, Liu Y, Ma X, Li DS, et al. Long-term stability challenges and opportunities in acidic oxygen evolution electrocatalysis. Angew Chem Int Ed. 2023;62(11):e202216645. [DOI]
75. Macounova K, Makarova M, Krtil P. Oxygen evolution on nanocrystalline RuO_2 and $Ru_{0.9}Ni_{0.1}O_{2-\delta}$ electrodes-DEMS approach to reaction mechanism determination. Electrochem Commun. 2009;11(10):1865-1868. [DOI]
76. Huang ZF, Song J, Du Y, Xi S, Dou S, Nsanzimana JMV, et al. Chemical and structural origin of lattice oxygen oxidation in Co-Zn oxyhydroxide oxygen evolution electrocatalysts. Nat Energy. 2019;4(4):329-338. [DOI]
77. Chen G, Lu R, Zhuang Z, Fei H, Li X, Zhang X, et al. Heterophase RuO_2 oxygen evolution catalyst for durable proton exchange membrane water electrolysis. Sci Adv. 2025;11(51):eaea4543. [DOI][PubMed][PMC]
78. Wu L, Huang W, Li D, Zhao B, Zhou H, Luo W. Role of interfacial water in improving the activity and stability of lattice-oxygen-mediated acidic oxygen evolution on RuO_2. Angew Chem Int Ed. 2025;64(22):e202420848. [DOI]
79. Rossmeisl J, Qu ZW, Zhu H, Kroes GJ, Nørskov JK. Electrolysis of water on oxide surfaces. J Electroanal Chem. 2007;607(1-2):83-89. [DOI]
80. Grimaud A, Diaz-Morales O, Han B, Hong WT, Lee YL, Giordano L, et al. Activating lattice oxygen redox reactions in metal oxides to catalyse oxygen evolution. Nat Chem. 2017;9(5):457-465. [DOI]

81. Han C, Liu Y, Wang T. Structure-activity relation of the oxide path mechanism for O-O coupling on rutile-based oxygen evolution reaction catalysts. ACS Energy Lett. 2025;10(9):4511-4517. [DOI]
82. Xu Y, Mao Z, Zhang J, Ji J, Zou Y, Dong M, et al. Strain-modulated Ru-O covalency in Ru-Sn oxide enabling efficient and stable water oxidation in acidic solution. Angew Chem Int Ed. 2024;63(8):e202316029. [DOI]
83. Liu H, Zhang Z, Fang J, Li M, Sendeku MG, Wang X, et al. Eliminating over-oxidation of ruthenium oxides by niobium for highly stable electrocatalytic oxygen evolution in acidic media. Joule. 2023;7(3):558-573. [DOI]
84. Shi Z, Li J, Wang Y, Liu S, Zhu J, Yang J, et al. Customized reaction route for ruthenium oxide towards stabilized water oxidation in high-performance PEM electrolyzers. Nat Commun. 2023;14(1):843. [DOI][PubMed][PMC]
85. Cao X, Miao L, Jia W, Qin H, Lin G, Ma R, et al. Strain heterogeneity in RuO_2 for efficient acidic oxygen evolution reaction in proton exchange membrane water electrolysis. Nat Commun. 2025;16(1):6217. [DOI][PubMed][PMC]
86. Chaudhary P, Zagalskaya A, Over H, Alexandrov V. Strain-dependent activity-stability relations in RuO_2 and IrO_2 oxygen evolution catalysts. ChemElectroChem. 2024;11:e202300659. [DOI]
87. Xue T, Liu Z, Song Y, Liu M, Zhang J, Zhou K, et al. Cation-vacancy induced compressive strain localization in RuO_2 catalyst for high-performance acidic oxygen evolution. Angew Chem Int Ed. 2026;65(12):e24664. [DOI][PubMed]
88. He S, Cheng M, Li F, Xie J, Sun T, Xu L. Mitigating the activity-stability trade-off in in-doped RuO_2 for acidic oxygen evolution via electronic regulation of lattice oxygen chemistry. ACS Catal. 2026;16(12):11147-11160. [DOI]
89. Deka N, Jones TE, Falling LJ, Sandoval-Diaz LE, Lunkenbein T, Velasco-Velez JJ, et al. On the operando structure of ruthenium oxides during the oxygen evolution reaction in acidic media. ACS Catal. 2023;13(11):7488-7498. [DOI]
90. Ji Q, Tang B, Zhang X, Wang C, Tan H, Zhao J, et al. Operando identification of the oxide path mechanism with different dual-active sites for acidic water oxidation. Nat Commun. 2024;15(1):8089. [DOI]
91. Wang J, Cheng C, Yuan Q, Yang H, Meng F, Zhang Q, et al. Exceptionally active and stable RuO_2 with interstitial carbon for water oxidation in acid. Chem. 2022;8(6):1673-1687. [DOI]
92. Zhang J, Qin H, Cao X, Jia W, Ma R, Chen X, et al. Constructing adjustable heterointerface for enhancing acidic oxygen evolution performances of RuO_2@$CoMnO_3$ nanosheets electrocatalysts. ACS Mater Lett. 2024;6(7):3016-3024. [DOI]
93. Wu H, Fu Z, Chang J, Hu Z, Li J, Wang S, et al. Engineering high-density microcrystalline boundary with V-doped RuO_2 for high-performance oxygen evolution in acid. Nat Commun. 2025;16(1):4482. [DOI][PubMed][PMC]
94. Li D, Wang W, Lian C, Lai Z. Enhancing OER activity and stability in acidic media: Ru heterojunction and oxygen vacancies synergy in RuO_2. Appl Surf Sci. 2025;712:164273. [DOI]
95. Wang Y, Yang R, Ding Y, Zhang B, Li H, Bai B, et al. Unraveling oxygen vacancy site mechanism of Rh-doped RuO_2 catalyst for long-lasting acidic water oxidation. Nat Commun. 2023;14(1):1412. [DOI][PubMed][PMC]
96. Gou W, Zhang S, Wang Y, Tan X, Liao L, Qi Z, et al. Oxygen spillover from RuO_2 to MoO_3 enhances the activity and durability of RuO_2 for acidic oxygen evolution. Energy Environ Sci. 2024;17(18):6755-6765. [DOI]
97. Wang JX, Inada H, Wu L, Zhu Y, Choi Y, Liu P, et al. Oxygen reduction on well-defined core-shell nanocatalysts: Particle size, facet, and Pt shell thickness effects. J Am Chem Soc. 2009;131(47):17298-17302. [DOI][PubMed]
98. Huang J, Li Y, Huang RK, He CT, Gong L, Hu Q, et al. Electrochemical exfoliation of pillared-layer metal-organic framework to boost the oxygen evolution reaction. Angew Chem Int Ed. 2018;57(17):4632-4636. [DOI]
99. Bhowmik T, Kundu MK, Barman S. Growth of one-dimensional RuO_2 nanowires on g-carbon nitride: An active and stable bifunctional electrocatalyst for hydrogen and oxygen evolution reactions at all pH values. ACS Appl Mater Interfaces. 2016;8(42):28678-28688. [DOI][PubMed]
100. Takimoto D, Fukuda K, Miyasaka S, Ishida T, Ayato Y, Mochizuki D, et al. Synthesis and oxygen electrocatalysis of iridium oxide nanosheets. Electrocatalysis. 2017;8(2):144-150. [DOI]
101. Kong X, Xu K, Zhang C, Dai J, Norooz Oliaee S, Li L, et al. Free-standing two-dimensional Ru nanosheets with high activity toward water splitting. ACS Catal. 2016;6(3):1487-1492. [DOI]
102. Zhao ZL, Wang Q, Huang X, Feng Q, Gu S, Zhang Z, et al. Boosting the oxygen evolution reaction using defect-rich ultra-thin ruthenium oxide nanosheets in acidic media. Energy Environ Sci. 2020;13(12):5143-5151. [DOI]
103. Chen C, Kang Y, Huo Z, Zhu Z, Huang W, Xin HL, et al. Highly crystalline multimetallic nanoframes with three-dimensional electrocatalytic surfaces. Science. 2014;343(6177):1339-1343. [DOI][PubMed]
104. Chen D, Yu R, Yu K, Lu R, Zhao H, Jiao J, et al. Bicontinuous RuO_2 nanoreactors for acidic water oxidation. Nat Commun. 2024;15(1):3928. [DOI]
105. Zhang J, Lin R, Zhao Y, Wang H, Liu S, Cai X. Modulation for RuO_2/TiO_2 via simple synthesis to enhance the acidic oxygen evolution reaction. ACS Sustainable Chem Eng. 2023;11(25):9489-9497. [DOI]
106. Gao F, Cao J, Gong Q, Yin Y, Chen Y, Bu X, et al. Hierarchical RuO_2/RuTi/Ti composite electrodes for highly efficient and durable oxygen evolution reaction in acidic proton exchange membrane water electrolysis. J Alloys Compd. 2025;1048:184988. [DOI]
107. Wang F, Wang W, Wang T, Wang X, Siniard KM, Fan J, et al. Flux synthesis of lattice-engineered rutile solid solutions for acidic oxygen evolution. Angew Chem Int Ed. 2025;64(49):e202514922. [DOI]
108. Zheng N, Yang B, Xie J, Hu J, Lu Z, Cao Y. Ru-RuO_2@Co/CNF bifunctional catalysts with enhanced HER and OER activity for efficient acidic and alkaline overall water splitting. Chem Eng J. 2026;529:173158. [DOI]
109. Zhang H, Li J, Yan H, Chen X, Fu H. Engineering of stabilized Ru-based proton exchange membrane water electrolysis. Adv Mater.

2026;38(7):e16207. [DOI]
110. Zhang H, Liu L, Pei L, Wang D, Wang X. Highly active and stable nitrogen-doped ruthenium oxide/titanium nitride composite anode electrocatalyst for practical proton exchange membrane water electrolyzers. Adv Energy Mater. 2025;15(29):2406074. [DOI]
111. Li H, Pan Y, Wu L, He R, Qin Z, Luo S, et al. IrO_2 deposited on RuO_2 as core-shell structured RuO_2@IrO_2 for oxygen evolution reaction in electrochemical water electrolyzer. Mol Catal. 2023;551:113619. [DOI]
112. Yang J, Ji Y, Shao Q, Zhang N, Li Y, Huang X. A universal strategy to metal wavy nanowires for efficient electrochemical water splitting at pH-universal conditions. Adv Funct Mater. 2018;28(41):1803722. [DOI]
113. Zhu H, Wang Y, Jiang Z, Deng B, Jiang ZJ. High activity and excellent durability of oxygen-vacancy-rich ruthenium manganese oxide solid-solution nanowires for the oxygen evolution reaction in acidic media. J Mater Chem A. 2023;11(46):25252-25261. [DOI]
114. Cao D, Xu H, Cheng D. Construction of defect-rich RhCu nanotubes with highly active Rh_3Cu_1 alloy phase for overall water splitting in all pH values. Adv Energy Mater. 2020;10(9):1903038. [DOI]
115. Yan H, Jiang Z, Deng B, Wang Y, Jiang ZJ. Ultrathin carbon coating and defect engineering promote RuO_2 as an efficient catalyst for acidic oxygen evolution reaction with super-high durability. Adv Energy Mater. 2023;13(23):2300152. [DOI]
116. Ge R, Li L, Su J, Lin Y, Tian Z, Chen L. Ultrafine defective RuO_2 electrocatayst integrated on carbon cloth for robust water oxidation in acidic media. Adv Energy Mater. 2019;9(35):1901313. [DOI]
117. Wang J, Ji Y, Yin R, Li Y, Shao Q, Huang X. Transition metal-doped ultrathin RuO_2 networked nanowires for efficient overall water splitting across a broad pH range. J Mater Chem A. 2019;7(11):6411-6416. [DOI]
118. Xiao M, Liu J, Li R, Sun Y, Liu F, Gan J, et al. Rapid conversion from alloy nanoparticles to oxide nanowires: Strain wave-driven Ru-O-Mn collaborative catalysis for durable oxygen evolution reaction. Small. 2024;20(30):2400754. [DOI]
119. Liu GQ, Yang Y, Zhang XL, Li HH, Yu PC, Gao MR, et al. Porous tellurium-doped ruthenium dioxide nanotubes for enhanced acidic water oxidation. Small. 2024;20(16):e2306914. [DOI][PubMed]
120. Madhu R, Karmakar A, Kumaravel S, Sankar SS, Bera K, Nagappan S, et al. Revealing the pH-universal electrocatalytic activity of Co-doped RuO_2 toward the water oxidation reaction. ACS Appl Mater Interfaces. 2022;14(1):1077-1091. [DOI][PubMed]
121. Mefford JT, Rong X, Abakumov AM, Hardin WG, Dai S, Kolpak AM, et al. Water electrolysis on $La_{1-x}Sr_xCoO_{3-\delta}$ perovskite electrocatalysts. Nat Commun. 2016;7(1):11053. [DOI]
122. Liu L, Ji Y, You W, Liu S, Shao Q, Kong Q, et al. Trace lattice S inserted RuO_2 flexible nanosheets for efficient and long-term acidic oxygen evolution catalysis. Small. 2023;19(38):e2208202. [DOI][PubMed]
123. Xue Y, Fang J, Wang X, Xu Z, Zhang Y, Lv Q, et al. Sulfate-functionalized $RuFeO_x$ as highly efficient oxygen evolution reaction electrocatalyst in acid. Adv Funct Mater. 2021;31(32):2101405. [DOI]
124. Qiu L, Zheng G, He Y, Lei L, Zhang X. Ultra-small Sn-RuO_2 nanoparticles supported on N-doped carbon polyhedra for highly active and durable oxygen evolution reaction in acidic media. Chem Eng J. 2021;409:128155. [DOI]
125. Liu Z, Liu H, Xue T, Zhou K, Li C, Shen Y, et al. Synergistic Sr activation and Cr buffering effect on RuO_2 electronic structures for enhancing the acidic oxygen evolution reaction. Nano Lett. 2024;24(35):10899-10907. [DOI]
126. Su J, Ge R, Jiang K, Dong Y, Hao F, Tian Z, et al. Assembling ultrasmall copper-doped ruthenium oxide nanocrystals into hollow porous polyhedra: Highly robust electrocatalysts for oxygen evolution in acidic media. Adv Mater. 2018;30(29):1801351. [DOI]
127. Wang J, Yang H, Li F, Li L, Wu J, Liu S, et al. Single-site Pt-doped RuO_2 hollow nanospheres with interstitial C for high-performance acidic overall water splitting. Sci Adv. 2022;8(9):eabl9271. [DOI][PubMed][PMC]
128. Li CH, Yuan CZ, Huang X, Zhao H, Wu F, Xin L, et al. Tailoring the electron redistribution of RuO_2 by constructing a Ru-O-La asymmetric configuration for efficient acidic oxygen evolution. eScience. 2025;5(1):100307. [DOI]
129. Samanta R, Panda P, Mishra R, Barman S. IrO_2-modified RuO_2 nanowires/nitrogen-doped carbon composite for effective overall water splitting in all pH. Energy Fuels. 2022;36(2):1015-1026. [DOI]
130. Hao Y, Hung SF, Tian C, Wang L, Chen YY, Zhao S, et al. Polarized ultrathin BN induced dynamic electron interactions for enhancing acidic oxygen evolution. Angew Chem Int Ed. 2024;63(18):e202402018. [DOI][PubMed]
131. Ede SR, Luo Z. Tuning the intrinsic catalytic activities of oxygen-evolution catalysts by doping: A comprehensive review. J Mater Chem A. 2021;9(36):20131-20163. [DOI]
132. Wu M, Fan Y, Huang Y, Wang D, Xie Y, Wu A, et al. Synergistic Ru/RuO_2 heterojunctions stabilized by carbon coating as efficient and stable bifunctional electrocatalysts for acidic overall water splitting. Nano Res. 2024;17(8):6931-6939. [DOI]
133. Li J, Yao M, Yuan Z, Ma J, Geng S, Liu F. Phase engineering boosting heterogeneous interface effect in RuO_2/MnO_2 catalysts for acidic oxygen evolution reaction. Chem Eng J. 2024;496:153921. [DOI]
134. Ai L, Wang Y, Luo Y, Tian Y, Yang S, Chen M, et al. Robust interfacial Ru-RuO_2 heterostructures for highly efficient and ultrastable oxygen evolution reaction and overall water splitting in acidic media. J Alloys Compd. 2022;902:163787. [DOI]
135. Song H, Yong X, Waterhouse GIN, Yu J, Wang H, Cai J, et al. RuO_2-CeO_2 lattice matching strategy enables robust water oxidation electrocatalysis in acidic media via two distinct oxygen evolution mechanisms. ACS Catal. 2024;14(5):3298-3307. [DOI]
136. Huang X, Lee C, Li Y, Xu J, Liu D. Acid-treated RuO_2/Co_3O_4 nanostructures for acidic oxygen evolution reaction electrocatalysis. ACS Appl Nano Mater. 2024;7(8):9244-9251. [DOI]
137. Stern LA, Feng L, Song F, Hu X. Ni_2P as a Janus catalyst for water splitting: The oxygen evolution activity of Ni_2P nanoparticles. Energy Environ Sci. 2015;8(8):2347-2351. [DOI]
138. Chen JL, Feng SY, Lu CJ, Huang JF. Janus Ru/RuO_2 nano-boomerangs on carbon as pH-universal electrocatalysts with bifunctional activity

toward the hydrogen/oxygen evolution reaction. Chem Eng J. 2023;468:143761. [DOI]
139. Li H, Zhou X, Zhai W, Lu S, Liang J, He Z, et al. Phase engineering of nanomaterials for clean energy and catalytic applications. Adv Energy Mater. 2020;10(40):2002019. [DOI]
140. Do VH, Prabhu P, Jose V, Yoshida T, Zhou Y, Miwa H, et al. Pd-PdO nanodomains on amorphous Ru metallene oxide for high-performance multifunctional electrocatalysis. Adv Mater. 2023;35(12):2208860. [DOI]
141. Zhang Y, Zhang Y, Zeng Z, Ho D. Order-disorder engineering of RuO_2 nanosheets towards pH-universal oxygen evolution. Mater Horiz. 2023;10(8):2904-2912. [DOI][PubMed]
142. Zheng W, Zhao Y, Jiang K, Xie F, Meng L, Gao S, et al. Heteroatom dopants overcome the activity-stability trade-off in RuO_2 for acidic oxygen evolution. Nat Commun. 2025;16(1):6716. [DOI][PubMed][PMC]
143. Cai J, Li P, Huang H, Wang S, Peng Y, Peng Y, et al. Stabilizing grain-boundary-rich RuO_2 by atomic iridium-doping to achieve high-performance oxygen evolution for ampere-level PEM water electrolysis. Chem Mater. 2026;38(3):1516-1526. [DOI]
144. Zheng WX, Cheng XX, Chen PP, Wang LL, Duan Y, Feng GJ, et al. Boosting the durability of RuO_2 via confinement effect for proton exchange membrane water electrolyzer. Nat Commun. 2025;16(1):337. [DOI]
145. Yuan B, Dang Q, Liu H, Sendeku MG, Peng J, Fan Y, et al. Synergistic niobium and manganese co-doping into RuO_2 nanocrystal enables PEM water splitting under high current. Nat Commun. 2025;16(1):4583. [DOI]
146. Miao X, Peng Z, Shi L, Zhou S. Insulating high-entropy ruthenium oxide as a highly efficient oxygen-evolving electrocatalyst in acid. ACS Catal. 2023;13(6):3983-3989. [DOI]
147. Yu S, Li L, Ma C, Zhang X, Li M, Wang A, et al. Iridium-free high-entropy ruthenium-based oxides with activated lattice oxygen towards high efficient and durable acidic water oxidation. Chem Commun. 2025;61(60):11223-11226. [DOI][PubMed]
148. Che Y, Zhang X, Bo S, An Q, Zhang J, Li B, et al. High-entropy ruthenium-based oxides with rich grain boundaries for efficient oxygen evolution. ACS Mater Lett. 2024;6(9):4142-4148. [DOI]
149. Nie W, Zhang Q, Xiao X, Jiang Z, Jiang ZJ. Plasma defect engineering to stabilize Mn-doped ruthenium dioxide nanoparticles for oxygen evolution via oxide path mechanism. J Mater Sci Technol. 2026;251:262-274. [DOI]
150. Tu Y, Shan X, Chen L, Zhang J, Yang L, Cai F, et al. Accelerated discovery of highly stable ruthenium-based high-entropy oxides for acidic oxygen evolution. Sci Adv. 2026;12(18):eaed8479. [DOI][PubMed][PMC]
151. Yao Y, Hu S, Chen W, Huang ZQ, Wei W, Yao T, et al. Engineering the electronic structure of single atom Ru sites via compressive strain boosts acidic water oxidation electrocatalysis. Nat Catal. 2019;2(4):304-313. [DOI]
152. Cheng R, Fu J, Shi L, Ren H, Peng B, Liu Y, et al. Surface iridium single-atom engineering enables a highly stable RuO_2 catalyst for efficient acidic water oxidation. Adv Energy Mater. 2026;16(31):e71254. [DOI]
153. Chen J, Ma Y, Cheng C, Huang T, Luo R, Xu J, et al. Cobalt-doped Ru@RuO_2 core-shell heterostructure for efficient acidic water oxidation in low-Ru-loading proton exchange membrane water electrolyzers. J Am Chem Soc. 2025;147(10):8720-8731. [DOI][PubMed]
154. Liu T, Guo J, Wu A, Shen D, Fan Y, Fu Y, et al. Single-atom Ru confined in self-supported mesoporous carbon films for efficient and stable acidic oxygen evolution. Chem Eng J. 2025;512:162387. [DOI]
155. Li J, Zhang Z, Tian Y, Zeng X, Chu K. A homonuclear ruthenium dual-atom catalyst enables efficient urea electrosynthesis via dual site-single site synergy. ACS Sustainable Chem Eng. 2025;13(45):19679-19687. [DOI]
156. Fang C, Zhou J, Zhang L, Wan W, Ding Y, Sun X. Synergy of dual-atom catalysts deviated from the scaling relationship for oxygen evolution reaction. Nat Commun. 2023;14(1):4449. [DOI]
157. Meharban F, Lin C, Wu X, Tan L, Wang H, Hu W, et al. Scaling up stability: Navigating from lab insights to robust oxygen evolution electrocatalysts for industrial water electrolysis. Adv Energy Mater. 2024;14(41):2402886. [DOI]
158. Zhang D, Li M, Yong X, Song H, Waterhouse GIN, Yi Y, et al. Construction of Zn-doped RuO_2 nanowires for efficient and stable water oxidation in acidic media. Nat Commun. 2023;14(1):2517. [DOI][PubMed][PMC]
159. Cherevko S. Stability and dissolution of electrocatalysts: Building the bridge between model and "real world" systems. Curr Opin Electrochem. 2018;8:118-125. [DOI]
160. Meng Q, Yue X, Shang L, Liu X, Wang F, Zhang G. Corrosion behavior of metallic coatings on titanium bipolar plates of proton exchange membrane water electrolysis. Int J Hydrogen Energy. 2024;63:1105-1115. [DOI]
161. Liu C, Carmo M, Bender G, Everwand A, Lickert T, Young JL, et al. Performance enhancement of PEM electrolyzers through iridium-coated titanium porous transport layers. Electrochem Commun. 2018;97:96-99. [DOI]
162. Tang Y, Huo M, Xing Z, Chang J. Innovations in membrane electrode assembly design and manufacture for PEMWE and PEMFC: A review on catalyst layers, diffusion layers, and fabrication methods. eScience Energy. 2026:100116. [DOI]
163. Matos BR, Dresch MA, Santiago EI, Moraes LPR, Carastan DJ, Schoenmaker J, et al. Nafion membranes annealed at high temperature and controlled humidity: Structure, conductivity, and fuel cell performance. Electrochim Acta. 2016;196:110-117. [DOI]
164. Zhang J, Fu X, Kwon S, Chen K, Liu X, Yang J, et al. Tantalum-stabilized ruthenium oxide electrocatalysts for industrial water electrolysis. Science. 2025;387(6729):48-55. [DOI][PubMed]
165. Wang X, Li Z, Jang H, Chen C, Liu S, Wang L, et al. RuO_2 with short-range ordered tantalum single atoms for enhanced acidic oxygen evolution reaction. Adv Energy Mater. 2025;15(6):2403388. [DOI]
166. Shim J, Lee K, Yu Y, Lee HS, Shin H, Lee KS, et al. Atomically dispersed high-valent d^0-metal breaks the activity-stability trade-off in proton exchange membrane water electrolysis. J Am Chem Soc. 2025;147(19):16179-16188. [DOI]
167. Huang L, Ma L, Yang J, Kang J, Chen Y, Yan J, et al. Electron donation from carbon support enhances the activity and stability of

ultrasmall ruthenium dioxide nanoparticles in acidic oxygen evolution reaction. J Colloid Interface Sci. 2025;686:438-447. [DOI]
168. Wan J, Qian F, Jiang W, Huang J, Xin Y, Hu C, et al. Gradient tuning the covalency of Ru-O bonds by 4f-electron to unlock dual-site oxide path mechanism for acid-stable water oxidation. Appl Catal B Environ Energy. 2026;392:126716. [DOI]
169. Tauster SJ, Fung SC, Garten RL. Strong metal-support interactions. Group 8 noble metals supported on titanium dioxide. J Am Chem Soc. 1978;100(1):170-175. [DOI]
170. Oh HS, Nong HN, Reier T, Bergmann A, Gliech M, Ferreira de Araújo J, et al. Electrochemical catalyst-support effects and their stabilizing role for IrOx nanoparticle catalysts during the oxygen evolution reaction. J Am Chem Soc. 2016;138(38):12552-12563. [DOI][PubMed]
171. Zhu F, Wu Q, Zhang D, Wu L, Song N, Han Y, et al. Advances in defect-engineered metal-support interactions for acidic oxygen evolution reaction. Mater Horiz. 2026;13(12):5851-5875. [DOI][PubMed]
172. Yu J, Cao L, Zhong S, Wang Y, Shang D, Yu M, et al. Mechanism-driven atomic-level engineering over RuO_2-based catalysts for proton exchange membrane water electrolysis. Adv Energy Mater. 2026;16(33):e71381. [DOI]
173. Wang T, Duan S, Pan J, Li J, Shao L, Shi L, et al. Interfacial Ru-O-W orbital coupling enables lattice oxygen stabilization for enhanced acidic OER. Carbon Energy. 2026;8(5):e70167. [DOI]
174. Liang J, Zhao Y, Yang C, Zhu S, Wang L, Xu K, et al. Dual-site cobalt-doped RuO_2/TiO_2 electrocatalyst enables stable and cost-efficient acidic oxygen evolution for PEM water electrolysis. J Am Chem Soc. 2025;147(43):39781-39795. [DOI]
175. U.S. Department of Energy, Hydrogen and Fuel Cell Technologies Office. Hydrogen and Fuel Cell Technologies Office Multi-Year Program Plan [Internet]. Available from: https://www.energy.gov/cmei/fuels/hydrogen-and-fuel-cell-technologies-multi-year-program-plan
176. International Energy Agency (IEA). Global Hydrogen Review 2024 [Internet]. Paris: IEA. Available from: https://www.iea.org/reports/global-hydrogen-review-2024
177. International Energy Agency (IEA). Global Hydrogen Review 2025 [Internet]. Paris: IEA. Available from: https://www.iea.org/reports/global-hydrogen-review-2025
178. State-owned Assets Supervision and Administration Commission of the State Council (SASAC). Sinopec Launches High-Efficiency Hydrogen Production Station [Internet]. SASAC Official Website. Available from: http://en.sasac.gov.cn/2021/11/09/c_8135.htm
179. Chinese Academy of Sciences (CAS). The Megawatt-Level Proton Exchange Membrane Water Electrolysis Hydrogen Production System Has Been Successfully Operated [Internet]. CAS Official Website. Chinese. Available from: https://www.cas.cn/cm/202110/t20211018_4809857.shtml
180. European Commission. Hydrogen [Internet]. Brussels: European Commission. Available from: https://energy.ec.europa.eu/topics/eus-energy-system/hydrogen_en
181. U.S. Department of Energy. Technical Targets for Proton Exchange Membrane Electrolysis [Internet]. Available from: https://www.energy.gov/cmei/fuels/technical-targets-proton-exchange-membrane-electrolysis
182. Chen H, Na M, Zou X. Iridium-based anode catalysts for water electrolysis: From fundamentals to industrial applications. CCS Chem. 2025;7(11):3259-3274. [DOI]
183. Yang Y, Yu Y, Li J, Chen Q, Du Y, Rao P, et al. Engineering ruthenium-based electrocatalysts for effective hydrogen evolution reaction. Nanomicro Lett. 2021;13(1):160. [DOI][PubMed][PMC]
184. Wang HF, Song LN, Wang S, Ding SJ, Xu JJ. Local electric field-driven reaction pathway regulation via Ru single atoms on highly curved carbon sphere for stable Li-O_2 batteries. Angew Chem Int Ed. 2026;65(3):e21423. [DOI]
185. Sopčić S, Roković MK, Mandić Z, Inzelt G. Preparation and characterization of RuO_2/polyaniline composite electrodes. J Solid State Electrochem. 2010;14(11):2021-2026. [DOI]
186. Bao J, Gu Y, Su B, Sun X, Zhang H, Wang K, et al. Electronic structure-engineered proton depletion interfaces on ternary RuO_2 for ultra-stable kilowatt electrocatalysis. Angew Chem Int Ed. 2025;64(45):e202515362. [DOI]
187. Liu H, Sun X, Gao FY, Zheng Y, Qiao SZ. Cost-efficient and stable electrolysis of reverse osmosis water using a Co-RuO_2-enabled PEM electrolyser. Nat Catal. 2026;9(1):9-17. [DOI]
188. Yao Q, Yu Z, Chu YH, Lai YH, Chan TS, Xu Y, et al. S incorporated RuO_2-based nanorings for active and stable water oxidation in acid. Nano Res. 2022;15(5):3964-3970. [DOI]
189. Qin K, Yu H, Zhu W, Zhou Y, Guo Z, Shao Q, et al. 1D Monoclinic $Ir_xRu_{1-x}O_2$ solid solution with Ru-enhanced electrocatalytic activity for acidic oxygen evolution reaction. Adv Funct Mater. 2025;35(21):2402226. [DOI]
190. Zhang X, Wu F, Zhang Q, Lu Z, Zheng Y, Zhu YA, et al. Self-supported WO_3@RuO_2 nanowires for electrocatalytic acidic water oxidation. Inorg Chem. 2024;63(18):8418-8425. [DOI]
191. Huang H, Kim H, Lee A, Kim S, Lim WG, Park CY, et al. Structure engineering defective and mass transfer-enhanced RuO_2 nanosheets for proton exchange membrane water electrolyzer. Nano Energy. 2021;88:106276. [DOI]
192. Hu J, Tong L, Jia Y, Li Z, Yang H, Wang Y, et al. Co-motif-engineered RuO_2 nanosheets for robust and efficient acidic oxygen evolution. ACS Appl Mater Interfaces. 2025;17(13):19734-19744. [DOI][PubMed][PMC]
193. Zhang X, He X, Wang C, Fan Z, Li B, Du P, et al. Facile synthesis of Mn/RuO_2 nanosheets for high-performance acidic oxygen evolution reaction. Mater Lett. 2023;340:134187. [DOI]
194. Yao Q, Le J, Yang S, Cheng J, Shao Q, Huang X. A trace of Pt can significantly boost RuO_2 for acidic water splitting. Chin J Catal. 2022;43(6):1493-1501. [DOI]
195. Li Y, Wang Y, Lu J, Yang B, San X, Wu ZS. 2D intrinsically defective RuO_2/Graphene heterostructures as All-pH efficient oxygen evolving

electrocatalysts with unprecedented activity. Nano Energy. 2020;78:105185. [DOI]
196. Wu Z, Wang Y, Liu D, Zhou B, Yang P, Liu R, et al. Hexagonal defect-rich MnO_x/RuO_2 with abundant heterointerface to modulate electronic structure for acidic oxygen evolution reaction. Adv Funct Mater. 2023;33(49):2307010. [DOI]
197. Deng M, Tang Y, Lu Z, Wang Y, Lin Y. Self-Supporting Mn-RuO_2 Nanoarrays for Stable Oxygen Evolution Reaction in Acid. Molecules. 2023;28(23):7727. [DOI][PubMed][PMC]
198. Zhang J, Wang X, Zhao X, Chen H, Jia P. Significantly enhanced acidic oxygen evolution reaction performance of RuO_2 nanoparticles by introducing oxygen vacancy with polytetrafluoroethylene. Polymers. 2024;17(1):59. [DOI][PubMed][PMC]
199. Lu Q, Liu J, Zou X, Huang B, Wu W, Yin J, et al. Breaking the activity-stability trade-off of RuO_2 via metallic Ru bilateral regulation for acidic oxygen evolution reaction. Angew Chem Int Ed. 2025;64(22):e202503733. [DOI]
200. Wang T, Li Z, Jang H, Kim MG, Qin Q, Liu X. Interface engineering of oxygen vacancy-enriched Ru/RuO_2-Co_3O_4 heterojunction for efficient oxygen evolution reaction in acidic media. ACS Sustainable Chem Eng. 2023;11(13):5155-5163. [DOI]
201. Wu Y, Yao R, Zhang K, Zhao Q, Li J, Liu G. RuO_2/CeO_2 heterostructure anchored on carbon spheres as a bifunctional electrocatalyst for efficient water splitting in acidic media. Chem Eng J. 2024;479:147939. [DOI]
202. Zhang Y, Huang H, Han Y, Qin Y, Nie N, Cai W, et al. Constructing stable charge redistribution through strong metal-support interaction for overall water splitting in acidic solution. J Mater Chem A. 2022;10(25):13241-13246. [DOI]
203. Wang X, Jang H, Liu S, Li Z, Zhao X, Chen Y, et al. Enhancing the catalytic kinetics and stability of Ru sites for acidic water oxidation by forming Brønsted acid sites in tungsten oxide matrix. Adv Energy Mater. 2023;13(36):2301673. [DOI]
204. Abed J, Heras-Domingo J, Sanspeur RY, Luo M, Alnoush W, Meira DM, et al. Pourbaix machine learning framework identifies acidic water oxidation catalysts exhibiting suppressed ruthenium dissolution. J Am Chem Soc. 2024;146(23):15740-15750. [DOI][PubMed]
205. Shang Z, Zhao S, Dang Q, Wang F, Sun X, Li H. A general machine-learning framework for high-throughput screening for stable and efficient RuO_2-based acidic oxygen evolution reaction catalysts. ACS Catal. 2025;15(15):12835-12847. [DOI]
206. Xing Y, Li H, Avgouropoulos G. Research progress of proton exchange membrane failure and mitigation strategies. Materials. 2021;14(10):2591. [DOI][PubMed][PMC]

Publisher's Note

Science Exploration remains a neutral stance on jurisdictional claims in published maps and institutional affiliations. The views expressed in this article are solely those of the author(s) and do not reflect the opinions of the Editors or the publisher.